OPTICAL CHARACTERIZATION OF CALCIUM FLUORIDE AND GREY TIN USING SPECTROSCOPIC ELLIPSOMETRY.

BY
Jaden R. Love, B.S.

A dissertation submitted to the Graduate School
in partial fulfillment of the requirements
for the degree
Master of Science

Major: Physics

NEW MEXICO STATE UNIVERSITY
LAS CRUCES, NEW MEXICO
(July 2025)

Jaden R. Love

Candidate

Physics

Major

This Dissertation is approved on behalf of the faculty of New Mexico State University, and it is acceptable in quality and form for publication:

Approved by the thesis Committee:

Dr. Stefan Zollner

Chairperson

Dr. Michael Engelhardt

Committee Member

Dr. Ludi Miao

Committee Member

Dr. Corey Frank

Committee Member

DEDICATION

I DEDICATE THIS WORK TO MY PARENTS,
JOHN LOVE + DENISE RIVERA-LOVE. ♥

ACKNOWLEDGMENTS

I would like to thank my advisor, Dr. Stefan Zollner, for his support and patience over the years. From the first time I heard the word "ellipsometry" to meeting John Woollam himself at the 10th ICSE, professor Zollner has provided valuable insights and encouragement. He has cultivated a wonderful research group and I would like to thank all of the people who I call teammates and friends from the NMSU Ellipsometry group. Carlos Armenta, Haley Woolf, Yoshitha Hettige, Sonam Yadav, Aaron Lopez Gonzalez, Gabriel Ruiz, Dannisa Ortega, Meghan Worrell, and most recently Jan Hrabovský- thank you for being awesome and for sharing your time and knowledge with me. I must also thank the group members who have graduated and continue to share their knowledge with the group, it is invaluable and I will maintain that relationship with future students. The closed loop helium system was installed with the help of Atlantis Moses and Jose Marquez; thank you for your efforts in regards to all parts of that project.

This project would not be here if it wasn't for the help of our collaborators from the University of Nebraska Lincoln and the University of California at Santa Barbara. Thank you to Dr. Mathias Schubert and his former student Dr. Megan Stokey from UNL for your help with collecting and interpreting data and engaging in a variety of insightful conversations. You have both inspired me and alongside the other members of your research group have helped to make me feel at home in the ellipsometry community. Thank you to Dr. Chris Palmstrøm, his student Aaron Engel, and his postdoc Wilson Parreno from UCSB for sharing their resources, facilities, and time to motivate and guide this project for characterizing grey tin films. I would also like to thank members of the J. A. Woollam Company who have

provided guidance in regards to technical support and the research topics through email and in person at at conferences.

This project has been funded most recently by the Air Force Office of Scientific Research (Grant No. FA9550-24-1-0061), the Air Force Research Lab (Grant No. FA9453-23-2-0001), and the National Science Foundation (Grant No. DMR-2423992). The project was initiated with support from the New Mexico Space Grant Consortium (NMSGC) and the SCalable Asymetric Lifecycle Engagement, SCALE, (Grant No. W52P1J-22-9-3009) program. A special thank you to Dr. Hyun-Jung Kim at the National Institute of Aerospace for motivating our investigation of calcium fluoride. The growth of the grey tin samples was preformed by our collaborators from UCSB and was supported by the Army Research Laboratory (Grants No. W911NF-21-2-0140 and No. W911NF-23-2-0031). Thank you all for providing support towards these types of projects, the outcome value is immeasurably high and I am truly grateful.

VITA

November 30, 2000	Born at Albuquerque, New Mexico, United States of America
2019 - 2024	B.S., New Mexico State University, Las Cruces, New Mexico
2022 - 2023	Supplemental Instruction Facilitator, Department of Chemistry, New Mexico State University
2021 - 2024	Research Assistant, Department of Physics, New Mexico State University
2024 - 2025	M.S., New Mexico State University, Las Cruces, New Mexico
2024 - 2025	Graduate Assistant, Department of Physics, New Mexico State University.

PROFESSIONAL AND HONORARY SOCIETIES

American Vacuum Society (AVS)

PUBLICATIONS

J. R. Love, C. A. Armenta, A. K. Moses, J. Hrabrovsky, S. Zollner, A. N. Engel, and C. J. Palmstrøm, *"Infrared ellipsometry measurements of carrier concentrations in doped gray α-tin on InSb and CdTe"*, (Planned submission: J. Appl. Phys.).

J. R. Love, S. Zollner, M. Stokey, M. Schubert, *"Determining the optical constants for commercially available bulk calcium fluoride using ellipsometry"*, (Planned submission: Surf. Sci. Spectr.).

J. Hrabovský, J. R. Love, L. Strizik, T. Ishibashi, S. Zollner, and M. Veis, *"TeO_2-BaO-Bi_2O_3 tellurite optical glasses II. - Linear and non-linear optical and magneto-optical properties"*, (Submitted to: Opt. Mater., 2025).

M. Milosavljevic, R. Carrasco, A. Newell, J. R. Love, S. Zollner, C. Morath, D. Maestas, P. Webster, and S. R. Johnson, *"Spectroscopic ellipsometry measurement and analysis of the optical constants of InAs/InAsSb and InGaAs/InAsSb superlattices and their bulk constituents"*, (Submitted to: J. Appl. Phys., 2025).

M. R. Arias, C. A. Armenta, C. Emminger, C. M. Zamarripa, N. S. Samarasingha, J. R. Love, S. Yadav, and S. Zollner, *"Temperature dependence of the infrared dielectric function and the direct band gap of InSb from 80 to 725 K"*, J. Vac. Sci. Technol. B **41**, 022203 (2023).

F. Abadizaman, J. R. Love, S. Zollner, *"Optical constants of single-crystalline Ni(100) from 77 K to 770 K from ellipsometry measurements"*, J. Vac. Sci. Technol. A **40**, 033202 (2022).

PRESENTATIONS

J. R. Love, C. A. Armenta, A. K. Moses, S. Zollner, A. N. Engel, C. J. Palmstrøm, *"Temperature Dependent Infrared Dielectric Function of Grey Tin on InSb (100)"*. 10th International Conference on Spectroscopic Ellipsometry, 8 – 13 June 2025, Boulder, CO.

J. R. Love, C. A. Armenta, M. Stokey, M. Schubert, S. Zollner, *"The Optical Constants of*

Calcium Fluoride from 0.03 – 9 eV". AVS 70th International Symposium and Exhibition, 3 - 8 November 2024, Tampa, FL.

S. Zollner, C. A. Armenta, S. Yadav, Y. Hettige, J. R. Love, H. B. Woolf, A. K. Moses, and D. P. Ortega, *"Optical spectroscopy of materials for mid-wave infrared detector applications"*, 7th Tri-Service Workshop on GeSn and GeSiSn. 16 - 17 September 2024, Colorado Springs, CO.

J. R. Love, *"Optical and structural properties of CaF_2"*. NMSU URCAS, 29 April 2022, Las Cruces, NM.

J. R. Love, N. S. Samarasingha, C. A. Armenta, S. Zollner, H. Kim, *"Optical constants of CaF_2 at 300 K from 0.03 to 6.5 eV"*. AVS 68th International Symposium and Exhibition, 6 - 11 November 2021, Pittsburg, PA.

J. R. Love, N. S. Samarasingha, C. A. Armenta, S. Zollner, H. Kim, *"Properties of CaF_2 using X-Ray Diffraction and IR Ellipsometry"*. 2022 APS March Meeting, 14 - 18 March 2022, Chicago, IL.

FIELD OF STUDY

Major Field: Physics

ABSTRACT

OPTICAL CHARACTERIZATION OF CALCIUM FLUORIDE AND GREY TIN USING SPECTROSCOPIC ELLIPSOMETRY

BY

Jaden R. Love, B.S.

Master of Science

New Mexico State University

Las Cruces, New Mexico, 2025

Dr. Stefan Zollner, Chair

In this work we present an optical study on two materials: calcium fluoride and grey tin. We use spectroscopic ellipsometry to determine the optical constants for both materials, but the interpretations of data are different because calcium fluoride is an insulator with a wide transparency range and grey tin is a semimetal with unique electronic properties. We use x-ray diffraction for structural characterization of the samples in order to support the analysis of ellipsometry data by verifying the surface orientation (for calcium fluoride) and layer thickness (for grey tin).

We refine the optical constants of calcium fluoride from 0.14 to 40 μm for two commercially available bulk substrates with surface orientations (100) and (111). We compare with

literature values from [1] and find that there is excellent agreement, especially in the infrared region where the infrared active phonon modes are identified. Towards the absorption band edge of calcium fluoride we find that the onset of absorption is slightly lower than in the literature [1] and attribute this to the presence of defects in the lattice.

For grey tin we measure the temperature dependent dielectric function using Fourier Transform Infrared (FTIR) ellipsometry from 300 K to 10 K and observe the $\bar{E}_0$ transition for two grey tin epitaxial layers grown by Molecular Beam Epitaxy (MBE) on InSb substrates with different interface preparations. The substrate interface preparation influences the number of donor or acceptor ions in the grey tin lattice and we observe a change in the oscillator strength of the $\bar{E}_0$ transition. We apply the Thomas-Reiche-Kuhn f-sum rule [2] to the $\bar{E}_0$ absorption peak and calculate the carrier density as a function of temperature. We compare carrier densities for grey tin samples that are considered intrinsic, p-type, and n-type doped. We find that the oscillator strength of the $\bar{E}_0$ peak is strongly dependent on the sample preparation that can change the type of doping in the grey tin layer.

CONTENTS

LIST OF TABLES

LIST OF FIGURES

1 INTRODUCTION

In this study we use x-ray diffraction (XRD) and spectroscopic ellipsometry (SE) to characterize bulk calcium fluoride (CaF_2) and thin grey tin (α-Sn) films grown on InSb (100) substrates. The materials are quite different in their properties. Studies of calcium fluoride go back a long time because the mineral has wide applications and is naturally abundant with reasonable quality. Optical studies of α-Sn are relatively new since the material has been notoriously difficult to stabilize, but is known to have interesting electronic properties like the other group IV elements. For each material we begin with a structural analysis using XRD in order to confirm the surface orientation, lattice constants, and check the quality of the material by comparing the spectra with powders and pure substrates. High resolution XRD is used to confirm the layer thickness for the 30 nm α-Sn films. SE data for calcium fluoride is collected from the infrared to the vacuum ultra-violet (VUV) at room temperature in ambient conditions. The data provides the optical constants of the material and we compare results with the compiled tables published by [1]. Infrared SE data for the α-Sn samples was collected under ultra-high vacuum (UHV) from room temperature down to 10 K. The temperature dependent data is modeled using a basis spline polynomial and we apply an optical sum rule to determine the carrier density as a function of temperature. The 30 nm α-Sn films were prepared on substrates with different surface preparations and by comparing the carrier density at all temperatures we show how substrate interface preparation influences the inter-valence band transitions in α-Sn. Here I introduce the motivation for studying these materials then I provide the supporting theory that guides the experimen-

tal procedure, analysis, and interpretation. I will explain the experimental methods starting with the structural characterization and sample preparation, the ellipsometric measurements and acquisition parameters, temperature dependent SE and the installation process of this equipment. There will be a chapter for each material that will include the specific methods and modeling techniques along with the compiled results. Then a summary and conclusion discussing the findings overall for both materials.

1.1 Calcium Fluoride

Calcium difluoride "calcium fluoride" is a neutral ionic compound with a formula unit consisting of one Ca^{2+} ion and two F^- ions. CaF_2 crystallizes in the cubic fluorite structure where the calcium ions occupy the face centered cubic (FCC) lattice, and the fluorine ions occupy a cubic lattice [1]. The crystal structure is in space group $Fm\bar{3}m$, No. 225 (O_h^5). The unit cell contains four formula units that are organized with four Ca^{2+} ions located at Wyckoff positions (4a) $m\bar{3}m$ (0,0,0) +FCC and eight F^- ions located at Wyckoff positions (8c) $\bar{4}3m$ ($\frac{1}{4}$, $\frac{1}{4}$, $\frac{3}{4}$) and ($\frac{1}{4}$, $\frac{1}{4}$, $\frac{1}{4}$) +FCC [3]. The lattice constant as reported by Rohrer is 5.4626 Å[3]. The lattice constant as reported by Bezuidenhout is 5.46305 Å [1]. Using XRD we find the lattice constants for bulk CaF_2 (111) and (100) to be 5.4639(8) Å and 5.4778(2) Å, respectively.

The interest in materials that can be used as windows and filters for the optical components required for spectroscopy measurements led to the characterization of materials such as calcium fluoride. CaF_2 is an insulator with a wide band gap of 11 eV and an exciton binding energy of 1 eV giving a fundamental absorption band at 12 eV [4]. The material has an especially wide transparency range that extends from the infrared to the ultra-violet. The

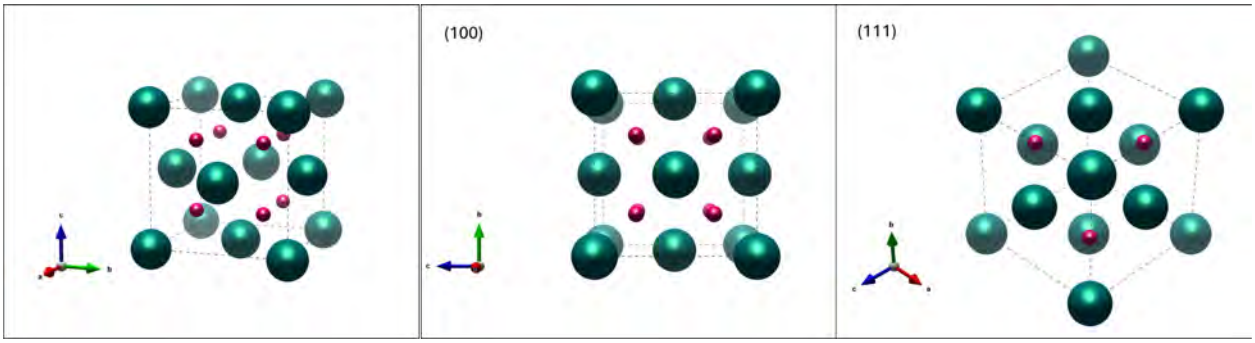

Figure 1: Calcium fluoride unit cell with fluorine, F^{1-}, ions (pink) in the cubic lattice and calcium , Ca^{2+}, ions (green) in the face centered cubic lattice.

bulk material has a Mohs hardness of 158.3 Knoop and a melting point of 1360°C [5] making it well suited for commercial manufacturing. These properties combined with the fact that the mineral is relatively abundant make CaF_2 ideal for use in optical components. The earliest publication showing the dispersion curve of fluorite was [6] showing data taken in 1893 by Handke who collected transmission measurements down to 1311 Å. Prior to modern growth methods only naturally occurring bulk crystals could be used. Natural crystals required mechanical polishing and often had non-parallel surfaces and visible scratching [7]. The issue with using fluorides as optical components has been the quality of available crystals. Over the years methods for crystal growth have been greatly improved by implementing modern electronics to increase accuracy and precision during growth so that the ideal conditions are maintained and the imperfections are reduced. Because of these advancements it has been possible to synthesize most naturally occurring minerals, fluorides being one of these, in a laboratory setting. Consequently, crystal quality has improved in the years since previous studies [8, 1, 9] were conducted and therefore it is reasonable to evaluate the properties of the currently available commercial bulk crystals [10].

Some of the more recent studies were conducted in the 1960's and determined the optical

properties of CaF_2 using reflection and transmission coefficients to calculate the complex refractive index [1, 8]. These measurements were taken at single wavelengths with larger intervals especially towards the far infrared and were time intensive. Kaiser [9] applied similar methods to determine the complex refractive index from 10 to 80 μm and calculated the infrared active phonon mode frequencies to be 257 cm^{-1} and 463 cm^{-1} (38.9 μm and 21.6 μm) for the transverse optical (TO) and longitudinal optical (LO) modes, respectively. The goal of this study is to expand on these results that were compiled previously by [1] using modern ellipsometry equipment and modeling software that are from commercial sources to determine the complex refractive index and infrared active phonon modes for calcium fluoride wafers with different surface orientations by analysis of ellipsometric angles measured over a continuous spectrum from 0.14 to 40 μm. We determined the optical constants of commercially purchased CaF_2 (111) and (100) bulk substrates using spectroscopic ellipsometry (SE). The CaF_2 (111) and (100) substrates are 10 x 10 x 1 mm square wafers that were purchased in 2022 from MTI Corporation. From the experimental data we identify one infrared active phonon mode and observe two phonon absorption in the reststrahlen band. The refractive index and extinction coefficient are plotted as a function of wavelength alongside the values tabulated in [1] and show excellent agreement with the literature values.

1.2 Grey Tin

Grey-tin, α-Sn, is a single crystalline, low-temperature, phase of tin that crystallizes in an FCC diamond-like structure. Like the structures of lighter group IV elements: C, Ge, and Si - at low temperatures the Sn^{4+} ions are more stable bonded covalently in a tetrahedral structure rather than through metallic bonding. The tetrahedral coordination of the basis

atoms gives the crystal O_h symmetry [3]. The Bravais lattice of grey tin is FCC and the conventional cubic unit cell contains eight Sn^{4+} atoms. The α-Sn structure belongs to space group Fd$\bar{3}$m No. 227 (O_h^7) and contains two atoms located at the Wyckoff positions (0,0,0) and ($\frac{1}{4}$, $\frac{1}{4}$, $\frac{1}{4}$) [11]. The lattice constant of α-Sn is 6.48920 Å[6]. The semi-metallic α phase is stable at temperatures below 13.2°C (286.2 K) [12] and above the critical temperature the structure transitions to the metallic β phase (white tin). Grey tin is less dense than white tin and with densities of $\rho_\alpha = 5.56\ \frac{g}{cm^3}$ and $\rho_\beta = 7.13\ \frac{g}{cm^3}$ [6]. White tin has 4 metallically bonded Sn atoms per unit cell and belongs to the tetragonal Bravais lattice. The material occupies a lower symmetry space group, $I4_1/amd$ [13]. The structural differences between the α and β phases elicit different mechanical and electronic properties from the material. β-Sn is useful for large scale manufacturing since it is stable at high temperatures but exhibits no novel electronic properties. α-Sn is more brittle and sensitive to environmental factors making it harder to produce on a large scale, but it can be stabilized in a laboratory and has been found to exhibit unique electronic properties. The critical temperature of α-Sn can be increased if the α-Sn lattice is stabilized when grown on substrates such as InSb and CdTe which have similar lattice structures and spacing [14, 12]. Growing α-Sn on a lattice matched substrate stabilizes the diamond-like cubic structure by strain from the substrate. The study by [12] shows that α-Sn layers grown on InSb (100) substrates remain fully strained up to 400 nm film thickness and we expect that the 30 nm layer grey tin samples will be stable over time at room temperature.

Advancements in fabrication methods have led to more intricate materials and devices with improved electronic properties. Semiconductors are in increasingly high demand for use in technology across all sectors of the global economy. These technologies range from cheap

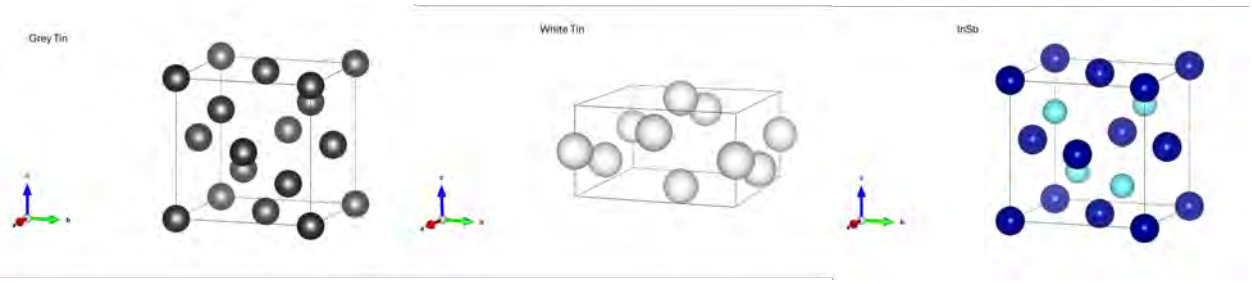

Figure 2: The unit cell structures for α-Sn (left), β-Sn (center), InSb (right) [15].

disposable batteries to large-scale military equipment, and it is essential that the devices operate efficiently. Semiconductors have relatively small energy gaps between their lowest unoccupied molecular orbital (the conduction band, CB) and the highest occupied molecular orbital (the valence band, VB). These materials are of particular interest because of their applications in microelectronics and photonics. Group IV elements are well known for their semiconductor properties with germanium (Ge) and silicon (Si) dominating the market. In addition to pure elemental structures the advancement in material growth methods has enabled the production of alloys, thin films, superlattices, and other novel structures that open the door to new possibilities for device fabrication. Ge_xSn_{1-x} alloys are of special interest since the band structure changes with composition and strain and their electronic properties can be tuned accordingly [16, 17]. They are especially good candidates for use in infrared detectors and could potentially replace the standard HgCdTe detector since Ge and Sn are less toxic. The goal for many of these studies is to investigate the influence of alloy compositions, strain, and doping on the materials electronic properties [18]. In addition to the magnitude of the gap energy, it is valuable to have a direct band gap transition as opposed to an indirect band gap transition. Direct transitions are transitions within the Γ valley and do not produce lattice vibrations because momentum is fully conserved by the

transition. Indirect transitions occur from the Γ valley to a satellite valley with a minimum at lower energy than the Γ valley. The net momentum is non-zero in this transition and a lattice vibration, a phonon, is produced so that momentum is conserved overall. Ge is an indirect material but can become direct by increasing the concentration of Sn atoms in the lattice [18]. The band gap energy in Ge_xSn_{1-x} alloys is tunable by changing the composition ratio [17]. Grey tin has potential for applications congruent to germanium tin alloys as an intrinsic semiconductor. The band structure of α-Sn is topologically protected and can be manipulated by changing the substrate material, interface preparation, layer thickness, strain, and doping. With the appropriate combination the band structure may be changed so that the material can behave as a topological insulator (TI) or Dirac semimetal (DSM) [19].

Molecular beam epitaxy (MBE) is one method used to grow epitaxial layers (such as α-Sn) on substrate materials (such as InSb or CdTe). MBE is done inside an evacuated chamber where a bulk material is fixed in place and its temperature maintained while surrounding cells containing source elements are heated until the elements sublime and deposit on the substrate surface as an epitaxial layer. In situ reflection high energy electron diffraction (RHEED) can be used to monitor growth and precisely control layer thickness by imaging the material during deposition. Atomic hydrogen cleaning removes oxides and other contaminants by annealing the substrate while exposing the surface to hydrogen radicals. Cleaning the interface to such a degree is essential because any contamination will ruin the overall crystal quality by changing the lattice structure.

The band structure of grey tin is interesting due to the negative energy of the electron-like s* band and the degeneracy of the p-like heavy-hole and light-hole bands at $\vec{k} = 0$. The

light-hole band has a positive curvature that is inverted relative to other group IV elements therefore appearing as a conduction band. The heavy-hole band has negative curvature like a valence band. The degeneracy and curvature inversion lead to referencing the material as a gapless semiconductor since the VB and CB are touching. As a consequence of the curvature inversion and position of the s* band inter-valence band transitions are allowed from the s* band into the heavy-hole band. The transition is the $\bar{E}_0$ since the energy gap is negative for this band arrangement. The transition is observable using infrared ellipsometry and has been recorded previously at 0.41 eV [18, 19]. From previous measurements [19] it is shown that the magnitude of the $\bar{E}_0$ absorption peak depends on the substrate material. Adding p-type dopants such as indium ions increases the number of holes in the valence band. Pure α-Sn is used as a reference sample for GeSn alloys and its optical properties have yet to be thoroughly characterized. There are few studies regarding the optical constants of α-tin. Many studies of the material have focused on the conditions for a phase transition of tin [12] or on Hall measurements [20] to determine carrier transport properties. Here we use temperature dependent Fourier Transform Infrared spectroscopic ellipsometry to measure intrinsic and n-type doped 30 nm thick α-Sn layers grown on InSb (100) substrates. We model the dielectric function using a basis spline (b-spline) polynomial and then determine the carrier density from the integrated peak intensity of the $\bar{E}_0$ transition using the Thomas-Reiche-Kuhn f-sum rule [2]. The data taken for 30 nm α-Sn layers on InSb (100) is compared to data for 70 nm α-Sn layers on InSb and CdTe substrates collected previously by [19]. The 30 nm α-Sn layer grown on the In rich interface has a larger oscillator strength than the layer grown on an Sb rich interface. The oscillator strength for both decreases towards low temperatures. Carrasco measured 70 nm α-Sn layers on InSb and CdTe substrates

for temperatures down to 77 K and modeled the the dielectric function using a parametric semiconductor model for the substrate and for the layer [19]. The study shows that the α-Sn layer grown on InSb had a large oscillator strength that appeared independent of temperature while the layer grown on CdTe had reduced oscillator strength that decreased at low temperatures. As an extension of this project I modeled the experimental data obtained by Carrasco using the b-spline function and applied the f-sum rule to find the carrier density.

2 THEORY

2.1 X-Ray Diffraction and High Resolution X-Ray Diffraction

X-ray diffraction (XRD) is a technique used for structural characterization of crystalline materials. A crystal is composed of a lattice plus a basis and is periodic in space. The lattice is described by the Bravais lattice vector (1), $\vec{R}$, which is formed from primitive translation lattice vectors: $\vec{a}$, $\vec{b}$, $\vec{c}$. These primitive lattice vectors are also components of the real space vector, $\vec{r}$. We make a translation from real space to reciprocal space by applying the relationship (3). The translation into reciprocal space is necessary because x-ray scattering is an indirect method that measures the electron density within the reciprocal space volume [21]. X-rays are high energy electromagnetic radiation that are represented by a plane wave solution (4). Inside a material the plane wave is scattered by electrons that have a periodic density within the lattice. If the scattering vector is observed then the plane wave must be periodic in the crystal and the scattering vector must be equal to a reciprocal lattice vector (2), $\vec{G}$. This leads to the Bragg's Condition (5), the diffraction condition for coherent scattered waves from a lattice. X-ray diffraction uses light with a wavelength on the same order of the atomic spacing between the lattice planes, Å, and when the lattice planes scatter waves there can be constructive or destructive interference. When the scattering is constructive such that the scattering vector is equal to a reciprocal lattice vector the waves are coherent and the scattering vector is observed [22, 21].

$$\vec{r} = x\vec{a} + y\vec{b} + z\vec{c} \tag{1}$$

$$\vec{G} = u\vec{a}^* + v\vec{b}^* + w\vec{c}^* \tag{2}$$

$$\vec{a}^* = \frac{2\pi}{V}(\vec{b} \times \vec{c}) \tag{3}$$

$$\vec{E} = \vec{E}_0 e^{i(\vec{k}\cdot\vec{r}-\omega t)} \tag{4}$$

$$2d\sin(\theta) = n\lambda \tag{5}$$

In addition to the angular dependence the intensity and selection rules must also be considered for interpreting diffraction data. The structure factor, $S(\vec{G})$, is used to determine the intensity and selection rules for a lattice and a particular basis that compose a crystal. To determine the selection rules $S(\vec{G})$ is calculated as a summation over the atoms in the basis and reciprocal lattice vectors (6). If the peak is not observable then the structure factor is 0 for a particular set of Miller indices. This explains why not all sets of Miller indices will appear in XRD spectra.

$$S(\vec{G}) = \sum_{i}^{N} f_i(\vec{G}) e^{i\vec{G}\cdot\vec{d}_i} \tag{6}$$

During a measurement we sweep the incident and diffracted beam angles and the scattering vector will be observed at an angle for different plane orientations inside the lattice. From the observed peak locations the Bragg equation (5) is used to determine the separation distance, d_{hkl}, between specific Bragg planes within the lattice. The Bragg equation depends on the lattice plane spacing, the diffraction angle, θ, the wavelength, λ, and the order of

diffraction, n. Based on the the structure factor, integrated peak intensity, and lattice plane spacing a crystals XRD spectra is characteristic of that lattice/basis combination and can be used to identify materials from a reference sample. For a cubic material (7) the formula for finding the lattice constant, a, is valid [3]. The value for the Bragg plane spacing is found from the Bragg condition (5) and the Miller Indices h,k, and l are determined by comparison with theoretical XRD spectra that was calculated from the simulated crystal structures in VESTA [15].

$$d_{hkl} = \frac{a}{\sqrt{h^2 + k^2 + l^2}} \tag{7}$$

High resolution XRD (HRXRD) uses incident beam optics that produce monochromatic x-rays and requires an extensive alignment procedure so that the diffraction plane is perpendicular to the Bragg plane of interest. The experimental data obtained for a thin film on a substrate will show a primary substrate peak with the highest intensity and a broader layer peak with a smaller intensity. In addition to the substrate and layer peaks there will be oscillations on the right and left sides of the layer peak called pendellösung fringes [21]. The peak positions are used to find the out of plane lattice constant, $a_\perp$. The equation that could be used to determine the layer thickness from the oscillation period given by [21, 23] is show in (8) and depends on the fringe spacing, $\Delta\theta_f$, the wavelength, λ, and the Bragg angle of the layer, θ_L.

$$t = \frac{\lambda}{\Delta\theta_f * 2 * \cos(\theta_L)} \tag{8}$$

For the analysis of HRXRD data we employed the program Epitaxy SmoothFit, an

associated software for the Empyrean machine from PANalytical [24]. The software simulates the experimental data based on user input describing the layer composition and lattice constants for the layer and substrate. The user then labels the substrate and layer peaks as well as the fringes. The parameters for background intensity and peak intensity are then adjusted to match the intensity of the experimental data. After obtaining a reasonable simulation of the experimental data the program calculates the layer thickness from the simulation fringe spacing. The other parameters that were determined using the HRXRD data are the in plane, $\epsilon_{||}$, and out of plane, $\epsilon_{\perp}$, lattice strain.

It is expected that the 30 nm α-Sn layer is pseudomorphic on the InSb (100) substrate and the in plane lattice constant, $a_{||}$, of the layer is expected to match the lattice constant of the substrate, $a_{||} = a_S$ and $\delta_{L||}$ in (12) is 0%. The symmetric (004) scan determines the out of plane lattice spacing for the material. The out of plane lattice constant is calculated using (7) and the d-spacing that was determined from the (004) symmetric rocking curve scan. The elastic moduli constants, c_{11} and c_{12}, from [6] are used to calculate the Poisson ratio (11), ν and then (9) for the parallel and (10) for the perpendicular lattice mismatch. The perpendicular lattice mismatch, $\delta_{L\perp}$, is found to be 0.19%.

$$\epsilon_{xx} = \epsilon_{yy} = \epsilon_{||} = \frac{a_{L||} - a_{L\infty}}{a_{L\infty}} = -0.16\% \tag{9}$$

$$\epsilon_{zz} = \epsilon_{\perp} = \frac{a_{L\perp} - a_{L\infty}}{a_{L\infty}} = 0.029\% \tag{10}$$

$$\nu = \frac{c_{12}}{c_{11}} = \frac{0.293}{0.69} = 0.43 \tag{11}$$

$$\delta_{L||} = \frac{a_{L||} - a_s}{a_s} = 0\% \tag{12}$$

$$\delta_{L\perp} = \frac{a_{L\perp} - a_s}{a_s} = 0.19\% \tag{13}$$

2.2 Spectroscopic Ellipsometry

Spectroscopic Ellipsometry is a non-destructive measurement technique that characterizes bulk materials and thin films using an optical probe. The technique is valued in the semiconductor industry as a means to characterize film thickness and optical properties of materials, devices, and device structures quickly and with high accuracy. The field of ellipsometry began by studying the elliptical polarization of light after reflection from a material. Methods and devices were developed to measure such changes in light and the whole field expanded and is now an essential tool for device manufacturing. One expansion is the devolvement of commercial ellipsometry equipment. Prior to commercial ellipsometers everyone constructed their own systems and analyzed the data using time intensive numerical approaches. Now with commercial ellipsometry equipment and data analysis software it is possible to measure and analyze more complicated data sets accurately and in a fraction of the time. The three ellipsometers used for this study are manufactured in Lincoln Nebraska by the J.A. Woollam Company and have each been designed with certian optical components to operate within a given spectral region between the infrared and the vacuum ultra-violet.

Ellipsometry is based on the concept that light is an electromagnetic wave interacting with materials based on boundary conditions that are derived from Maxwells equations and must be fulfilled for the fields at an interface. The unpolarized electromagnetic wave oscillates with

a certain phase and amplitude in all directions perpendicular to the direction of propagation defined by the wave vector $\vec{k}$. When the direction of oscillation and the phase have been fixed the light becomes polarized. Polarized light comes in three flavors and is essential for extracting useful optical data since an ellipsometry measurement relies on quantifying the change in polarization after reflection by a material. The three flavors of polarization are: linear polarization, circular polarization, and elliptical polarization. The source light for an ellipsometry measurement, the incident wave vector, $\vec{k}_i$, has two linearly polarized waves called, r_s and r_p, with the same phase and amplitude. Their directions of polarization are such that one electric field vector, $\vec{E}_p$, oscillates parallel to the plane of incidence, while the other electric field vector, $\vec{E}_s$, oscillates perpendicular to the plane of incidence. The plane of incidence is defined as the plane that contains $\vec{k}_i$ and the surface normal vector that is defined by the sample orientation in the experimental set up. The angle of incidence is defined as the angle between the $\vec{k}_i$ and the surface normal vector. When the incident beam encounters a change in medium, an interface, it undergoes reflection and transmission at the boundary. The boundary conditions obtained from Maxwells equations determine that the $\vec{E}_{\parallel}$ and $\vec{D}_{\perp}$ vectors must be continuous at the interface [25]. By passing through the interface the relative polarization between $\bar{E}_p$ and $\bar{E}_s$ will change. This change in polarization between the incident beam and the reflected beam can be quantified by measuring the difference in amplitude, Ψ, and phase Δ for $\bar{E}_p$ and $\bar{E}_s$. This difference is quantified based on Fresnel's reflection and transmission coefficients for the behavior of light at an interface. Equations (14) and (15) show the reflection coefficients for p and s light waves [26]. The transmission coefficients are described in a similar way, t_s and t_p, and since the intensity is related to the square amplitude of the electric field the squares of these coefficients represent reflected

and transmitted intensity [26]. Considering momentum and energy conservation rules the reflection and transmission conditions dictate that the sum of reflected light intensity R and transmitted light intensity T should be equal to the total intensity of the incident beam [25]. The ratio of reflected intensities, $\frac{R_p}{R_s}$, is equivalent to the square of the tangent of the ellipsometric angle, Ψ [26]. The relationship leads to the fundamental ellipsometry equation (16) that depends on the phase Δ and $\tan(\Psi)$. The ellipsometric angles Ψ and Δ are used to are related to the pseudo-dielectric function via equation (17) [27]. The experimental data is then modeled by applying known theoretical descriptions to extract the dielectric function and optical constants of the material as a function of wavelength. Equation (20) shows the relationship between the dielectric function and complex reflective index.

$$r_p = \frac{E_{rp}}{E_{ip}} = \frac{n_t cos(\theta_i) - n_i cos(\theta_t)}{n_t cos(\theta_i) + n_i cos(\theta_t)} \tag{14}$$

$$r_s = \frac{E_{rs}}{E_{is}} = \frac{n_i cos(\theta_i) - n_t cos(\theta_t)}{n_i cos(\theta_i) + n_t cos(\theta_t)} \tag{15}$$

$$\rho = \tan(\Psi)e^{i\Delta} = \frac{R_p}{R_s} = \frac{|r_p|^2}{|r_s|^2} \tag{16}$$

$$\langle \epsilon \rangle = \sin^2(\theta_i)[1 + \tan^2(\theta_i)(\frac{1-\rho}{1+\rho})^2] \tag{17}$$

$$\tilde{n} = n + ik \tag{18}$$

$$\epsilon = \epsilon_1 + i\epsilon_2 \tag{19}$$

$$\epsilon = \tilde{n}^2 \tag{20}$$

2.3 Lorentz Model

Depending on the material, material structure, and incident wavelength the optical response will vary. Experimental ellipsometry data has features such as peaks and valleys, trends in slope, or periodic oscillations, that will appear in specific spectral regions and are caused by things such as inter valence band transitions, the presence of free carriers, interference effects from thin films, or behavior outside of the measured region. It is important to select a model for the experimental data that justifies the optical response of a given material using known descriptions from electromagnetic theory. For this study I have measured two very different materials: the first is a a bulk insulating material that is transparent from the infrared to the near ultra violet, the other is a thin film semi metal that was deposited on a semiconductor substrate and is not transparent in the infrared. Different considerations for modeling are required to describe the data for each material. In the insulating material we observe an infrared active phonon and no absorption until high energies. The other material is a thin semi metallic film that has an inter valence band transition observable in the infrared.

The Lorentz oscillator model treats atoms in a lattice as a 3-D series of masses connected by springs with a certain spring constant. This is because the charges are not free they are instead bonded to neighboring atoms. When an electromagnetic wave interacts with the lattice a dipole moment is induced causing polarization of the bound charges. Newtons second law can be applied to describe the response of the spring mass system when there is an external polarization applied. Polarization is proportional to the electric displacement

though the susceptibility, χ [28]. The following equation shows the relationship between the relative dielectric constant, ϵ, the polarization, P, and the dielectric susceptibility. The electric field, $\vec{E}$, is proportional to the plane wave solution (4).

$$\frac{\epsilon}{\epsilon_0} = \epsilon = 1 + \frac{P}{\epsilon_0 E} = 1 + \chi \tag{21}$$

The dielectric constant (19) is a complex number with real and imaginary parts that are frequency dependent and when measured as a function of frequency it is called the dielectric function. The real part ϵ_1, corresponds to the dispersion and the imaginary part ϵ_2, corresponds to the absorption of the material. For a Lorentz oscillator (22) the dielectric function follows the form where ω_P^2 is the plasma frequency, ω_0 is the resonant frequency of the spring, ω is the applied frequency, and γ is the damping coefficient of the system. The plasma frequency (23) is a constant proportional to the square of the free electron charge e, the electron density of the material N_e, the vacuum permittivity ϵ_0, and the free electron mass m_e [28].

$$\epsilon(\omega) = 1 + \frac{\omega_P^2}{(\omega_0^2 - \omega^2) + i\gamma\omega} \tag{22}$$

$$\omega_p = \frac{e^2 N_e}{\epsilon_0 m_e} \tag{23}$$

The Lorentz oscillator description of the dielectric function appears as a peak in ϵ_2 centered at the resonant frequency ω_0 and with a broadening, γ. In ϵ_1 the Lorentz oscillator appears as a wiggle that crosses zero at the same frequency as ω_0. In other words, ϵ_1 and ϵ_2 are not independent of each other and they are connected by the Kramers-Kronig (KK) relationship which states generally that if the values of ϵ_2 are known then ϵ_1 can be calculated from the KK relationship [26]. When there is a peak in ϵ_2 there must be a wiggle in ϵ_1 and it is this relationship that maintains physicality of the oscillator models.

Experimental data is typically modeled using a sum of oscillators such as the Lorentzian to describe the peaks and wiggles at different frequencies. Each oscillator contributing to the sum has the fitting parameters for amplitude A_n, broadening γ_n, and position E_n. The Lorentz model is a physical model based on the dynamics of a three dimensional mass-spring system and can be used to describe absorption features caused by lattice vibrations or inter valence band transitions. Calcium fluoride is an insulator with one infrared active phonon mode and one Raman active phonon mode [9, 29]. The infrared active phonon mode splits into one transverse optical (TO) and one longitudinal optical (LO) phonon. The TO phonon mode is directly observable as a sharp peak in ϵ_2 and the LO phonon mode is found from the peak position in the imaginary part of the loss function (25). Here we use the Lorentz model to describe the restrahlen band. The restrahlen band is a region of high reflectivity that appears near the lattice resonant frequencies and in isotropic materials such as calcium fluoride the p and s components are totally reflected [30]. At the TO frequency the reflectivity increases and then remains high until the LO frequency where the reflectivity drops off again. The rise and drop in reflectivity appear as a plateau in the ellipsometric angle Ψ. Equation (24) shows the Lorentz oscillator model in terms of its application to the phonon modes.

The separation between LO and TO modes is indicative of the bond iconicity and the mode frequency corresponds to the bond strength between the atomic masses [30]. Calcium fluoride is a highly ionic compound and the restrahlen band is expected to be wide [31]. Typically infrared data is modeled by a summation of Lorentzian functions that correspond to the infrared active phonon modes. The TO pole (ω_{TO}) appears in the imaginary part of the dielectric function while the LO pole (ω_{LO}) appears in the imaginary part of the loss funciton. The high frequency dielectric constant ϵ_∞, is related to the static dielectric

constant ϵ_s, through the Lydanne-Sachs-Teller (LST) relationship for the TO and LO phonon modes [30]. The equations (24) and (25) are summations over all observable phonon modes. In the equations the summation is not included because CaF_2 has one directly observable phonon, the IR active TO phonon.

$$\epsilon = \epsilon_\infty + \frac{A\omega_{TO}^2}{\omega_{TO}^2 - \omega^2 - i\omega\Gamma_{TO}^2} \tag{24}$$

$$\epsilon^- = \epsilon_\infty^- + \frac{B\omega_{LO}^2}{\omega_{LO}^2 - \omega^2 - i\omega\Gamma_{LO}^2} \tag{25}$$

$$\epsilon_S = \epsilon_\infty + \frac{\omega_{LO}^2}{\omega_{TO}^2} \tag{26}$$

The high-frequency dielectric constant ϵ_∞ reduces almost linearly with increasing band gap and for materials where there is no iconicity ϵ_s is equal to ϵ_∞ [28]. This is the case for grey tin since there is no difference in iconicity between and two tin ions. The relationship between ϵ_s and ϵ_∞ for an ionic compound such as calcium fluoride is given by (27) [32]. The value A_{TO} is the amplitude of the peak in the imaginary part of the dielectric function corresponding to the TO phonon mode.

$$\epsilon_s = \epsilon_\infty + A_{TO} \tag{27}$$

In previous studies they have modeled the visible dielectric function of CaF_2 using Sellmeir dispersion formulas [8]. Here we have modeled the infrared dielectric function of calcium fluoride using two Lorentz oscillators that describe the restsrahlen band in Ψ. The VUV dielectric function of calcium fluoride was modeled using a combination of Gaussian functions and high energy poles associated with the fundamental absorption gap that is outside of the measured spectral region. Due to wavelength differences the infrared ellipsometer is not as sensitive to thin films as in the visible and therefore the VUV model includes a surface layer that is not included in the infrared model.

2.4 Basis Spline Polynomials

For more complex materials such as thin semi metallic epitaxial films on a substrate the optical response is not easily described by the Lorentz oscillator model. A oscillator model for this type of sample should consider the film thickness, the optical properties of the substrate, the contribution of free carriers, and the influence of other inter band transitions (critical points). Oscillator models describing these features include many fitting parameters and are often not intuitive to the user, particularly when the goal is only to find a smooth function that follows the experimental data. Evaluating these exact contributions is not the focus of this research project and it has been shown that the basis spline representation can describe the dielectric function of materials [33]. For these reasons we have opted out of the standard physics based oscillator models in favor of a non-physical basis spline (b-spline) polynomial to determine the delectric function of the α-Sn layers thus qualitativly describing the $\bar{E}_0$ transition. An example of the b-spline polynomial curve is given by [26] where it is demonstrated that the b-spline method produces a smooth function that follows the optical response of a given material using few fitting parameters. The b-spline is a summation of basis functions whose center positions are separated by a specified distance called the node spacing [34]. The basis functions are localized polynomials that are summed together to form the b-spline curve [26]. Because the individual basis functions are localized at the node point adjustments made in one region will not influence basis functions outside of that region; the basis functions are independent of each other [26]. This is not the case for the standard oscillator model where the oscillator parameters are dependant on each other. The b-spline is used to describe absorption features in ϵ_2 and then ϵ_1 is determined

from a KK transformation. The value of ϵ_2 is forced positive to ensure physical results and avoid negative absorption features. The node spacing can be adjusted to resolve sharp and broad features but it is important to select a reasonable node spacing. With an appropriate node spacing optical features such as an absorption peak can be resolved with high accuracy and without introducing a lot of artificial oscillations. If the node spacing is too small the data will be overfit and there will be additional oscillations that are introduced by the model weaving through all data including the noisy data. This issue with using a small node spacing is similar to issues with using a point-by-point fit (wavelength by wavelength fit) that interpolates through all data points including noise and introducing artifacts in the model. In order to use a b-spline model for finding the layer optical constants the layer thickness and substrate optical constants should be known. For this study of epitaxial grey tin films on InSb (100) substrates the grey tin layer thickness was confirmed from HRXRD (004) symmetric rocking curve scans and the substrate optical constants have been determined previously down to 77 K for bulk InSb (100) wafers [35] .

2.5 Optical Sum Rules

Optical sum rules are derived from dispersion relationships and the f-sum rule shown in (28) is one such rule [2]. In the description we consider N number of electrons in a volume V to be a rigid mass that responds collectively to a uniform oscillating electric field when the driving force is sufficiently high [36]. The equation of motion for the system is then related to the overall polarization and ultimately the real part of the dielectric function, ϵ_1, found via KK transformation of the imaginary part, ϵ_2 [36, 37]. These properties lead to a relationship between ϵ_2 and ω_p. Absorptions due to IVB transitions are observed as peaks

in ϵ_2. The magnitude of the peak depends on the number of particles contributing to the transition. Each electron in an atom has a certain resonance frequency and if measured over a sufficiently large frequency range a summation of the oscillator strengths, $f(\omega)$, for all the absorption peaks will be equivalent to atomic number, Z [2]. This summation over $f(\omega)$ is known as the Thomas-Reiche-Kuhn f-sum rule [2]. Over a continuous spectrum the summation becomes an integral (28) that is proportional to the plasma frequency squared (23). The proportionality constant depends on the number of electrons per volume N, the rest mass of the electron m_e, electron charge e, and the vacuum permittivity ϵ_0 [36].

$$\int_0^\infty \omega\epsilon_2(\omega)d\omega = \frac{1}{2}\pi\omega_p^2 \tag{28}$$

For this analysis we have modified equation (28) so that ω_p could be used to determine the carrier density of the grey tin layers from the oscillator strength of the $\bar{E}_0$ IVB transition observed in ϵ_2. First, the measured spectral range is limited by the instrumentation and therefore we are limited to energies between 0.1 and 0.8 eV and consequently the integration limits are restricted to the region under the $\bar{E}_0$ peak. Second, the absorption peak in ϵ_2 is attributed to IVB transitions from Γ_7^- to Γ_8^{+c} meaning that the effective mass of the Γ_7^- heavy holes, m_{hh}^*, should be considered. The heavy hole effective mass is known from magneto-reflectance measurements [20]. Third, the energy or the absorption peak maximum is making the most contributions to the $\bar{E}_0$ transition and is pulled out of the integral as a constant value. Reduced Plancks constant, $\hbar$, is added to make the conversion from frequency units to energy units and the electron density "N" is renamed "p" to indicate that the carriers are holes rather than electrons. The modified equation is shown in (29). A linear background is

subtracted from $\epsilon_2(E)$ and the integral from E_a to E_b over $\epsilon_2(E)$ is taken as the integrated peak intensity. The equation is then solved for carrier density, p, and plotted as a function of temperature.

$$\bar{E}_0 \int_{E_a}^{E_b} \epsilon_2(E) dE = \frac{\pi}{2} \frac{p e^2 \hbar^2}{\epsilon_0 m_0 m^*_{hh}} \tag{29}$$

2.6 Fermi Dirac Carrier Statistics

One outcome of this project is to determine the influence of the substrate preparation and substrate material on the oscillator strength of the $\bar{E}_0$ transition and calculate the heavy-hole density as a function of temperature by applying the f-sum rule. The results from experimental data are compared with a theoretical calculation of the carrier density for intrinsic α-Sn. The theoretical carrier density calculation [38] is based on degenerate Fermi-Dirac carrier statistics and uses effective masses that have been determined by magneto-reflectance measurements [20]. The density of states in each band changes with the chemical potential and temperature as shown in (30). The Γ_7^- VB is always fully occupied and the zero energy point is set at the Γ_8^+ degeneracy point. For intrinsic α-Sn at 0 K the Γ_8^+ band is fully occupied and IVB transitions are not allowed. At higher temperatures there are unoccupied heavy hole states especially for electron deficient p-type samples. Increasing the number of heavy hole states increases the strength of the $\bar{E}_0$ transition from Γ_7^- to Γ_8^+ and is observed as a change in amplitude of the absorption peak in infrared SE measurments [38, 19]. The number of heavy holes will depend on the preparation method used to grow the grey tin which has been demonstrated perviously by [19]. We expand on this study by measuring two 30 nm α-Sn layers grown on InSb (100) substrates with different interface

preparations leading to one indium rich interface (sample AE225) and one antimony rich interface (sample AE227).

$$f(E) = \frac{1}{e^{\frac{E-\mu}{k_B T}} + 1} \tag{30}$$

3 METHODS

3.1 Sample Preparation and Structural Characterization

The calcium fluoride samples purchased from MTI corporation were ready for measurements in the condition they were received in and no further steps were taken to polish, roughen, or clean the samples. The 30 nm thick α-Sn samples: AE225 and AE227 were prepared by collaborators at the University of California at Santa Barbara using MBE. The grey tin samples were delivered in a vacuum sealed bag and measurements were taken within a few weeks of breaking the vacuum seal. Structural characterization of the calcium fluoride samples was done prior to ellipsometry measurements using XRD. Structural characterization of the epitaxial grey tin layers was preformed after temperature dependent ellipsometry measurements and included measuring powder x-ray diffraction scans as well as HRXRD to measure a symmetric (004) rocking curve scan to confirm the 30 nm layer thickness for sample AE225 and justify the layer thickness required to model the ellipsometry data.

Samples were measured using the Empyrean x-ray diffractometer from Malvern PANalytical. The Empyrean is a 5-axis x-ray diffractometer that uses an in-plane vertical goniometer and horizontal sample stage. X-ray generation is done using a copper (Cu) target that emits both continuous and characteristic radiation due to emissions from the oscillations of electrons in the Cu target. The Cu target is bombarded with an electron beam from a tungsten (W) fillament by applying a voltage to the fillament. The characteristic radiation of Cu includes emissions from K_{α_1}, K_{α_2}, and K_{β}. Cu-K_{α_1} has a wavelength of 1.540598 Å and produces diffraction peaks with the highest intensity. Cu-K_{α_2} produces a diffraction peak

with half intensity that is at a slightly larger 2θ position. Cu-K_β radiation is mostly blocked by a nickel (Ni) filter in the diffracted beam optics [22]. The water-cooled x-ray tube is line focused and made of an evacuated bulb with a W filament cathode and a Cu anode. For data collection we apply 45 kV and 40 mA to the x-ray tube. The radiation emitted by the source is passed through a series of incident beam optics that shape and guide the beam onto the sample where the beam gets reflected and passed through a series of diffracted beam optics before the signal is collected in the detector and processed on a computer. High resolution XRD uses a different incident optics component called the hybrid monochromator that emits monochromatic x-rays and requires an extensive alignment procedure so that the Bragg plane of interest is perpendicular to the diffraction plane.

The incident beam optics that were used to measure XRD spectra for calcium fluoride include the Bragg-Brentano^{HD} (BBHD) a 1/4° divergence slit, a 10 mm beam mask, and a 1° anti-scatter slit. The diffracted beam optics include a programmable anti-scatter slit (PASS) with an automatic slit width 0.5 mm, 0.04 rad soller slit, a 0.02 mm thick Ni filter, and the PIXcel detector. The beam optics for measuring the grey tin samples are the incident beam optics were changed to use a 1/2° anti-scatter slit and a 2 mm beam mask. The experimental set up is labeled in Figure 3.1. For measurements the sample is first mounted and aligned on the sample stage and fixed with small brackets. Alignment of the sample starts with aligning the 2θ position such that the beam enters the detector with maximum intensity then the sample height is adjusted to cut the beam in half. This alignment ensures that the beam hits the sample in the center with maximum intensity. During measurements the sample remains fixed while the goniometer rotates to collect data over a defined 2θ range. As the goniometer scans the range the detector is counting events and at particular angles where

the Bragg diffraction condition is met there is constructive interference after reflection from the sample causing an increase in the number of detected events. The data appears as a series of peaks with a linear background. Experimental data for each material is compared with calculated lattice spacing values from VESTA [15].

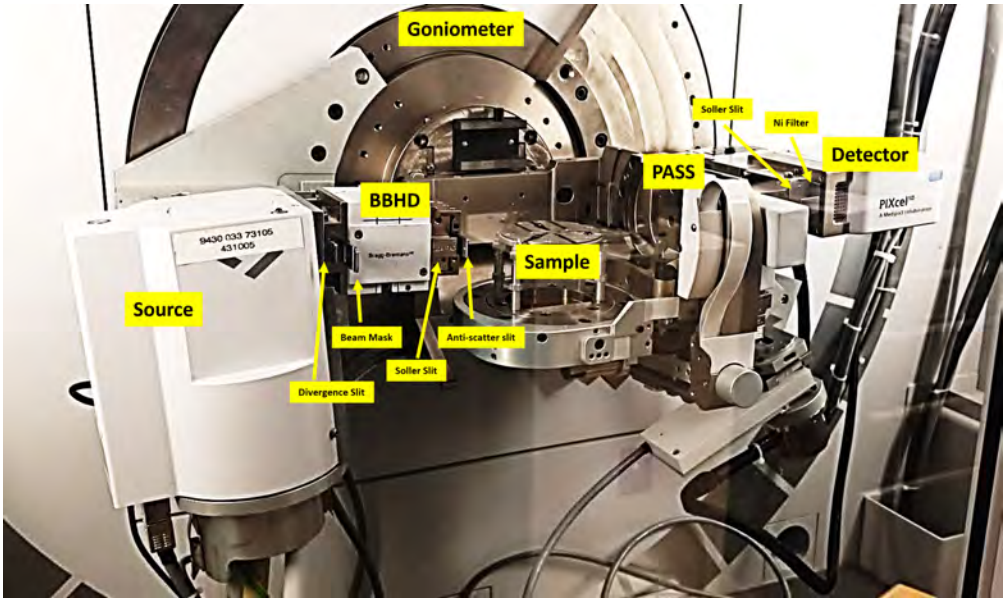

Figure 3: Experimental set up for collecting XRD data. The incident beam optics are to the left of the sample stage and the diffracted beam optics are to the right.

Powder diffraction measurements were collected for a 99.95% tin powder, and two calcium fluoride powders with 99.95% and 99.99% purity. The powders were measured in the same Empyrean XRD from Malvern PANalytical by lightly packing the powder into a metallic dish about 0.2 cm deep and 2.0 cm diameter. The incident beam optics used for the calcium fluoride powder were the Bragg-Brentano^{HD} (BBHD) with a 4 mm beam mask, a 1° anti-scatter slit, and a 1/4° divergence slit.

The incident beam optics used for the tin powder were the Bragg-Brentano^{HD} (BBHD) with a 10 mm beam mask, a 1/2° anti-scatter slit, and a 1/4° divergence slit. The diffracted beam optics used were a programmable anti-scatter slit (PASS) with a 0.5 mm slit width,

0.04 rad soller slit, a 0.02 mm thick Ni filter, and the PIXcel detector. The diffracted beam optics were the same for both powder scans. The same alignment for 2θ and sample height is done to maximize the intensity into the detector. During measurements the sample remains fixed while the goniometer rotates to collect data over a defined 2θ range. Experimental data for the powders are compared with the theoretical diffraction spectra provided by VESTA in order to determine the Miller indices corresponding to each diffraction peak[15].

HRXRD was used to measure $\omega - 2\theta$ scans for AE225 and AE227. The incident beam optics consists of a parabolic mirror and a 2-bounce Ge(220) hybrid monochromator with a 10 mm beam mask and a $1/32^\circ$ divergence slit. The diffracted beam optics include the PASS, 0.04 rad soller slit, 0.02 mm Ni filter, and the PIXcel detector. The optical set up is shown in Figure 4. The sample is mounted on the sample stage and fixed with small brackets. The alignment starts with the same 2θ and z axis procedure and then the geometry of the beam path is specified so that the substrate Bragg planes are perpendicular to the incident beam [21]. After fixing the beam path geometry further alignments are made for 2θ (incident/diffracted beam angle), ω (in scattering plane sample tilt), ϕ (sample rotation), and χ (out of scattering plane sample tilt). The position of all parameters are adjusted until the detected x-ray intensity is at a maximum and the peaks are narrow. During the coupled 2θ-ω rocking curve the parameters 2θ and ω move together with the ratio $\frac{\Delta\omega}{\Delta 2\theta} = 1/2$ and with fixed alignment offsets.

3.2 Infrared Ellipsometry

Infrared ellipsometry data for the calcium fluoride and grey tin samples is collected on the IR-VASE Mark II ellipsometer. The IR-VASE uses a globar light source that is not

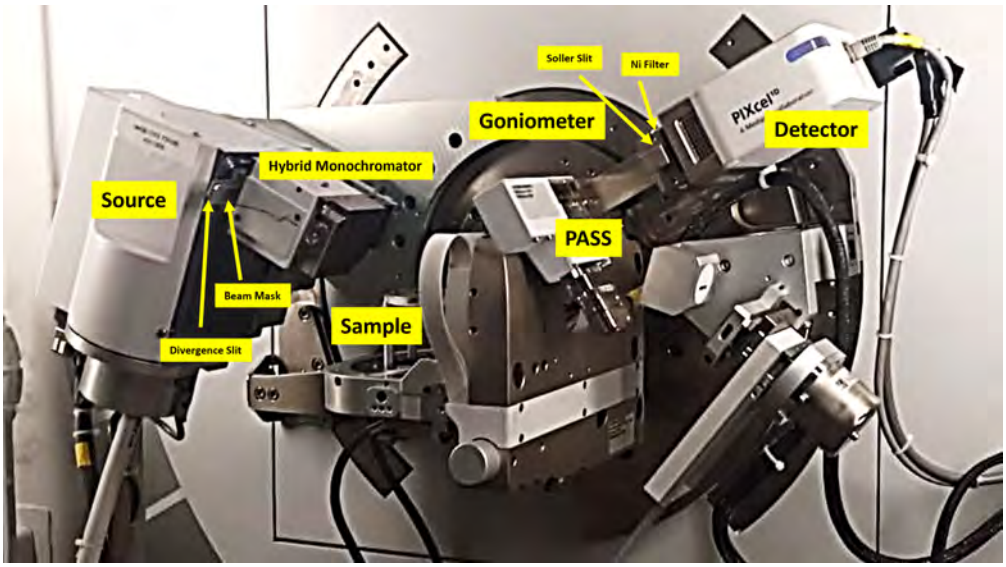

Figure 4: Figure shows labeled optical set up for symmetric (004) rocking curve.

monochromatic and has a spectral range from 1,400 nm to 40,000 nm (0.03 - 0.8 eV).

For infrared ellipsometry the light source enters a Michelson Interferometer that is able to discern different wavelengths. The interferometer output enters the beam folding optics to redirect the light towards the sample. The reflected light then enters another set of beam folding optics before finally entering the detector [30]. One issue with IR ellipsometry is the intensity of the light source, this is overcome by heating a silicon carbide rod (globar) that will emit diverging light which is then redirected by mirror optics into the intended beam path. Since the beam is not collimated the angle of incidence varies slightly in the incident beam causing depolarization [30].

Infrared SE measurements that are collected in ambient conditions have the samples mounted on the sample stage using slight vacuum pressure. The x-y alignment is preformed with the sample normal anti-parallel to the incident beam and the x-y position is adjusted so that the light is reflected directly back with equal intensity in all four quadrants of the alignment detector. The sample and detector are then rotated so that the angle of incidence

is 70° and the sample is moved in the z direction until the reflected beam enters the center of the detector iris with the maximum intensity. A measurment is then collected with specified aquisition parameters and the detector transfers the desired signals to the computer where the WVASE-IR software displays the experimental data.

3.3 Visible Ellipsometry

The Vertical Variable Angle Spectroscopic Ellipsometer (V-VASE) is a rotating analyzer ellipsometer (RAE) that uses a xenon light source and covers a spectral range from 190 nm to 2500 nm (0.5 - 6.5 eV). The V-VASE is composed of a monochromator, a fiber optic cable, an input unit, the sample stage, goniometers, and the detector. To collect SE data the xenon lamp is ignited and warmed to produce the source light. The light is focused on the monochromator which selects the wavelength based on input from the computer. The monochromatic light then enters the beam modulator that is a mechanical chopper which modulates the light intensity and filters out undesired harmonics. The fiber optic cable directs the beam to the input unit which collimates and polarizes the light. The AutoRetarder is an additional compensator working with the input unit to add polarization states. Then the incident beam, monochromatic and polarized, exits the first aperture where it passes through air and then is reflected by the sample into the detector unit. The reflected beam enters the detector unit through the iris where the light is modulated by a rotating polarizer (the analyzer) and then is registered in the detector and the desired signals are sent into the computer. On the computer the experimental data appears in the WVASE32 software. The description of hardware components was pulled from the VASE users manual by the J. A. Woollam Company [27]. There are two detectors used in the V-VASE that

cover different wavelength regions. The Si photo diode detector covers the range up to 1100 nm and then there is a transition to an InGaAs detector that covers the region towards 2500 nm. Samples are mounted on the stage with light vacuum pressure and the alignment procedure begins with the x-y alignment to maximize the intensity then the z-axis alignment to maximize intensity into the detector.

For VUV ellipsometry, which is required to measure up to 9 eV, the set up is similar to the V-VASE ellipsometer with a few exceptions. The VUV-VASE has a spectral range from 140 nm to 1700 nm (0.7 - 9 eV) and also uses RAE with an AutoRetarder and a xenon light source at lower energies. Unlike the ellipsometers described above measurements taken with the VUV-VASE must be done within a nitrogen rich atmosphere therefore the whole ellipsometer is enclosed in a nitrogen purged chamber. In order to achieve the shortest wavelengths the source of light source is changed to Deuterium. Additionally, the detector system is supplemented with a photomultiplier tube for detection at the shortest wavelengths [27].

3.4 Temperature Dependent Ellipsometry

Previously low temperature measurements were run using liquid nitrogen and were restricted by the limited Dewar size and minimum temperature of 77 K. In the spring of 2024 I worked with two other students to unpack, install, and operate a closed loop recirculating helium system with the condition that the new system had to be compatible with our existing commercial ellipsometers from J.A. Woollam Co. and continuous flow cryostats from Lakeshore Cryotronics. Our existing ellipsometers have vertical sample stages and cryostat attachments. The vertical arrangement posed some challenges and required an additional lift cart

to elevate the cold head and transfer arm to the height of our cryostat. The system was installed with the help of two peers over the course of one semester.

Before delivery we made a Gantt chart shown in Figure 5 to plan the installation process. Time was set apart for unpacking the cryocooler, electrical work orders, connecting hoses and fitting, checking arrangement, ordering additional parts, testing and troubleshooting, designing and running the experiment, analyzing data, and compiling the results.

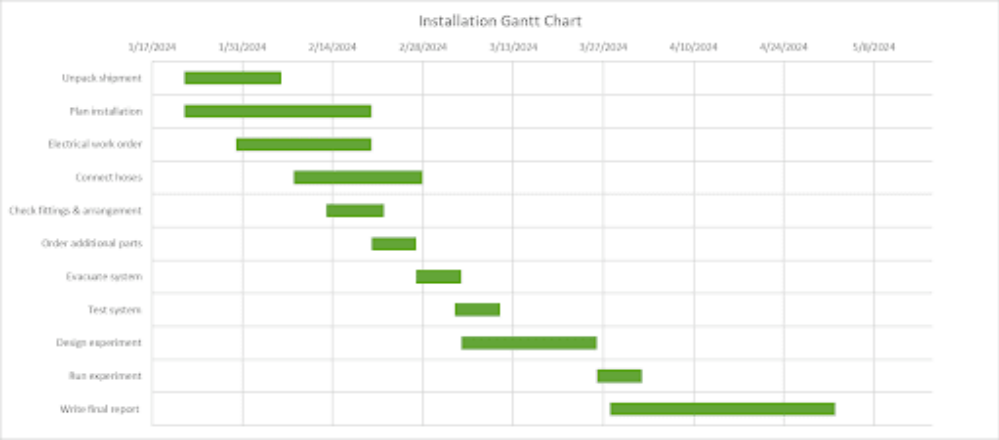

Figure 5: Gantt chart describing the installation timeline for the recirculating helium system.

Table 1: System components and function in the recirculating cooler system.

Component	Operations
Helium storage tank	Stores gaseous helium between cryocooler uses
Zeolite trap	Filters circulating helium
Compressor	Compresses helium during circulation
Cold head	Connects to compressor & transfer arm
Cryostat	Stores liquid helium
Transfer arm	Transfers cooled helium to cold finger
Vibration isolator	Separates pump vibrations from sample
Circulation pump	Circulates helium for cool down
Turbo pump & roughing pump	Evacuate system

The closed loop system consists of a FA-50L helium compressor purchased from Sumitomo Coorporation and the gas handling system (GHS) with cold head purchased from LakeShore Cryotronics. Cooling power is a product of the Joule-Thompson effect which generally states

that in certain conditions the gases undergoing a pressure reduction may experience a drop in temperature. Cryocoolers are devices that generate a net decrease in the gas temperature and require special conditions to operate effectively. The cooling procedure involves three phases: the first is the evacuation of the GHS, the second is room temperature circulation of helium, and the third is the final cool down where the base temperature of 5 K can be achieved. The GHS includes a 30 L He storage tank maintained at 5 psi, a circulation pump, a zeolite trap, and a vibration isolator. During phase one the storage tank is kept closed and the valves between the remaining components and the transfer arm are opened into a turbo pump until the pressure is less than $1 \cdot 10^{-5}$ Torr. In phase two the evacuation valve that was used to pump out the GHS is closed and the storage tank valve is opened. The circulation pump is running in phase two so that He gas is cycled around the evacuated GHS space at room temperature. In phase three the helium compressor is started and this begins the cycling of helium into the cryogen space of the sample chamber. Before the sample starts to cool the first and second stage heat exchangers of the cold head are cooled to 3 K and 35 K then the sample temperature will begin to drop. The base temperature is achieved by adjusting the pressure of delivered He gas from the storage tank and opening the needle valve slightly to maintain maximum cooling power.

Uncompressed He gas starts in the helium storage tank, passes the zeolite trap, before making its way through the cold head and into the compressor. The now compressed helium travels back through the cold head, through the transfer arm and into the cryogen space of the ultra-high vacuum (UHV) cryostat where the sample is cooled through the cold finger via thermal contact. The helium exits through the exhaust port and then passes the vibration isolator to the storage tank. A circulation scroll pump continues cycling the He gas through

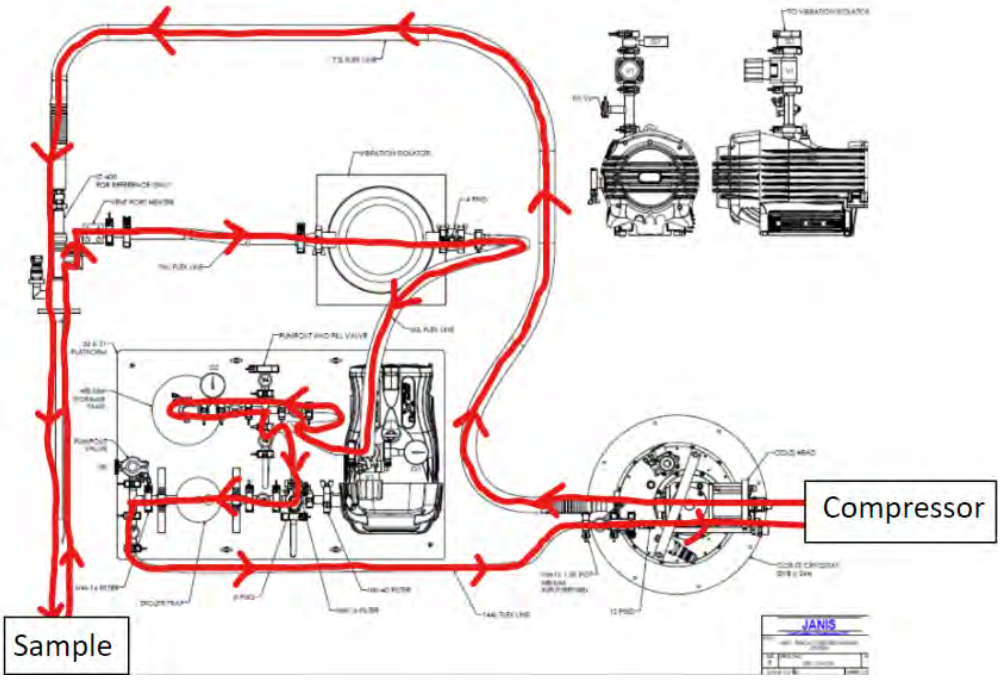

Figure 6: An overview of the full helium circulation system, provided by the manual and edited for clarity.

the GHS. We recorded the initial readings for the pressure gauges located at different parts of the GHS: the cold head, the storage tank, and the circulation pump. And then recorded the pressures during and after each phase of the cool down procedure. This was necessary to ensure that there was no major leaks in the system especially since a He detector is out of our budget for this project. Upon delivery there was pressurized He in the supply and return lines and 30 L in the GHS storage tank and they were handled with care. Because the helium was contained in the return and supply lines, the compressor could not be connected to the rest of the system until the end of the installation process, when the cryostat was prepared and evacuated for sample cooling.

Several electric work orders were requested to complete the wiring and setup for the compressor while the rest of the system was installed. We labeled the hoses and laid out the arrangement to ensure all parts were available and ordered additional parts as needed.

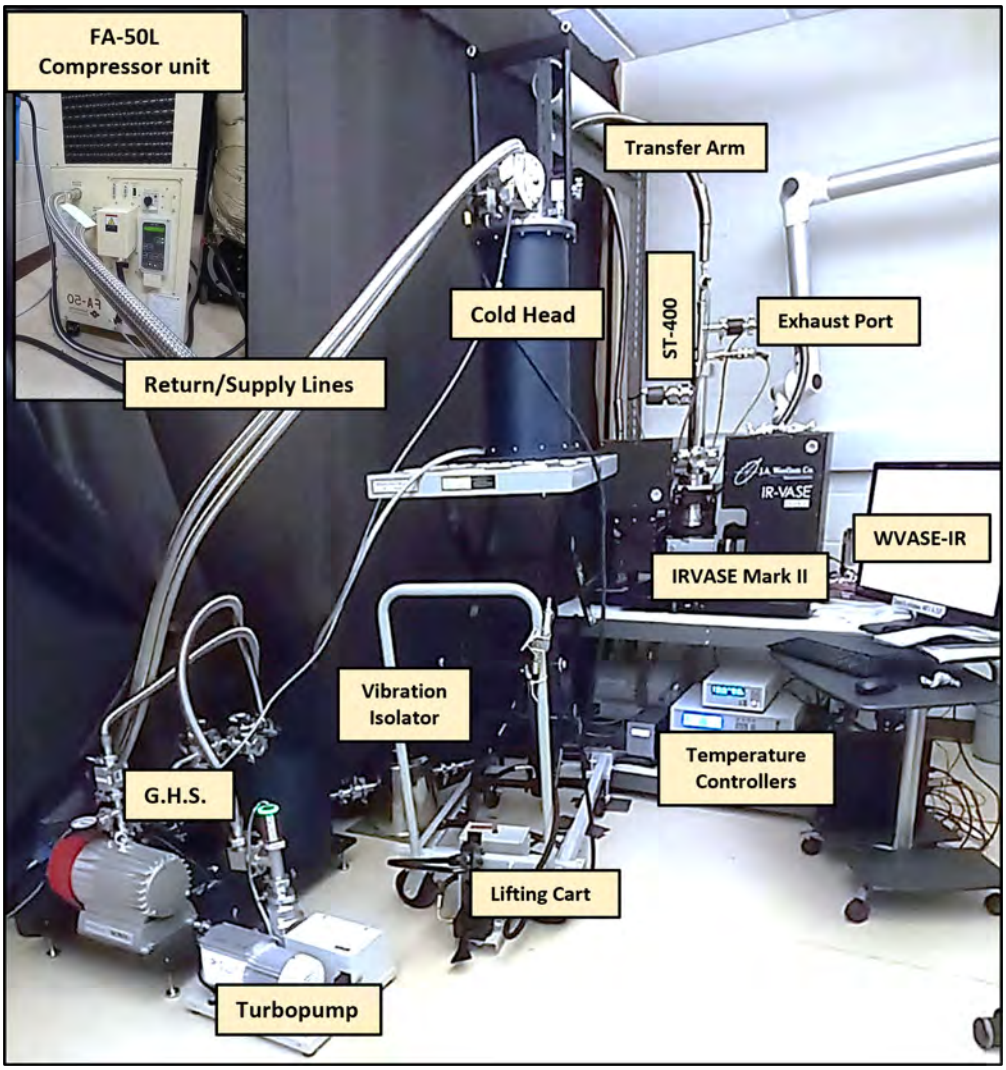

Figure 7: Final arrangement of the recirculating He system with component labels.

The cold head was fixed to the lifting cart with velcro strips. Finally, all hose connections were made for the GHS. Once the gas handling system was complete a NiO test sample was prepared for a temperature series. The sample had to be mounted on a cold finger that uses a Si diode sensor since these are more accurate with low temperature measurements than thermocouples. We chose to use Coldfinger #4 which has two Si diodes, one in the cryogen space and the other on the sample stage. Coldfinger #4 does not have the additional heater component mounted near the transfer arm to prevent frost formation. Because of this the

room humidity condenses and freezes at the top of the cryostat forming a thick layer of ice during measurements. The heater box was attached later by the J.A. Woollam Company and is not apart of the original Lakeshore design.

After mounting the sample the transfer arm is inserted into the top of the cryostat and the evacuation process for the cryostat chamber begins. First the dry scroll pump is started and the UHV pressure reaches $1 \cdot 10^{-2}$ Torr then the turbo pump is started and the pressure drops to less than $1 \cdot 10^{-7}$ Torr. Using the dry scroll pump for the initial evacuation prevents damage in the turbo pump. During the evacuation of the cryostat the first phase of the cool down procedure runs simultaneously. The GHS is evacuated using a backing pump and turbo pump system that is separate from the cryostat pumping system. The GHS should always be evacuated to a pressure less than $1 \cdot 10^{-4}$ Torr over the course of three hours or longer. If this pressure can be achieved a leak is unlikely. The GHS can consistently be evacuated to at least $1 \cdot 10^{-5}$ Torr and no leak is suspected. Phase two cycles helium through the system for several hours before the final cool down of the sample. The final cool down involves adjusting the needle valve on the cold head to achieve the appropriate flow and maintain cooling power. After the low temperature is reached at the sample the needle valve is closed fully to decrease pressure in the cold head and during this time the sample temperature rises about 25 K. After the pressure reaches -8 psi in the cold head the needle valve is opened 3/8 of a turn and the temperature of 5 K is reached in about 30 minutes. The lowest base temperature of 3 K can be acheived by making repeated adjustments of the needle valve that are accompanied by waiting periods to let the temperature stabilize.

Temperature dependent ellipsometry measurements were collected for grey tin samples AE225 and AE227 from 295 K to 10 K inside a UHV cryostat mounted on the IR-VASE

Mark II. The UHV cryostat chamber is outfitted with diamond windows that are transparent in the infrared region. The cryostat chamber is mounted on the goniometer and replaces the standard sample mounting stage for the IRVASE-Mark II ellipsometer. Low temperatures were reached by employing the cryogen free closed loop helium re-circulation system described previously. Samples AE225 and AE227 are thin and brittle. The α-Sn phase is stabilized at room temperature by the InSb substrate and the structure is sensitive to pressure and temperature. High pressures and high temperatures are likely to cause a phase transition and were avoided. The samples were fixed to the stage from the backside using silver conductive paint. Light pressure with a microfiber cloth was applied to level and maximize contact with the sample stage. The silver paint cured overnight in air at room temperature. Sample AE225 was mounted on a gold plated sample holder with a solid back. Sample AE227 was mounted on a gold plated sample holder with a hole behind the sample (this stage would be intended for transmission measurements). The samples were mounted on different stages so that they could be measured in quick succession, but because we used the transmission sample stage the experimental data for AE227 has larger depolarization than AE225. The depolarization for AE227 is about 12 % and for AE225 it is about 2 % across the whole measured region. The sample stage is mounted on the end of the cold-finger using three screws. There is a thin copper sheet between the stage and the cold finger end that increases thermal conductivity to the sample. Attached to the back of the sample holder with another screw is the silicon diode that measures the sample temperature via the negative relationship between the temperature coefficient and forward bias [39]. The whole cold finger assembly is inserted vertically into the cryostat chamber and the two sections are sealed using a copper gasket and fine threaded screws tightened

in a star-type pattern to prevent leaks. The cold finger design seperates the cryogen space from the vacuum space preventing any cryogen from contaminating the UHV chamber and sample. There are temperature sensors in each part of the cold finger: a silicon diode on the sample holder and a silicon diode in the cryogen space. The cryostat chamber is pumped out overnight to a pressure less than $1 \cdot 10^{-7}$ Torr and left under vacuum during the remaining cooling procedure. The cryostat is evacuated over the course of several days prior to measurement to remove water vapor and other contaminants from the chamber. Typically the sample would be baked overnight at temperatures above 400 K to remove water vapor but we do not do this for α-Sn in effort to preserve the diamond like structure of the epitaxial layers and prevent the phase transition to β-Sn. The temperatures of the first and second stage heat exchangers are monitored using a Lakeshore 336 PID temperature controller. The temperature of the first stage stays around 35 K and the second stage heat exchanger stays at 3 K after the third phase of the cool down procedure therefore this controller is only used to display the temperature and these temperatures are not recorded. The temperatures of the two Si diodes inside the cold finger are monitored simultaneously using a Lakeshore 335 temperature controller. The 335 is a proportional-integral-derivative (PID) controller that we use to maintain a specified temperature with accuracy and precision over an extended period of time. The 335 temperature controller displays both the sample temperature (input B) and cryogen space temperature (input A) and is linked to the computer running the data collection software, WVASE-IR. The software includes a feature that allows users to program steps in a series so that temperature changes are done automatically.

4 CALCIUM FLUORIDE

4.1 Sample Description

Four 10 x 10 x 1 mm square CaF_2 wafers were purchased from MTI Corporation; two samples with a (100) surface orientation and two samples with (111) surface orientations. For each surface orientation we have a single side polished sample (1sp) and a double side polished sample (2sp). The double side polished sample is not compatible with ellipsometry measurements due to higher depolarization caused by reflections from the backside sample surface therefore we use single side polished samples where one side has been roughened by a chemical or mechanical process. Backside roughening is done so that light is scattered, not reflected, at the back surface. In 2sp samples the transmitted light refracts into the material then is partially reflected off of the backside surface leading to an infinite series of reflections. The polarization of the reflected rays, such as a circular polarized ray and a linearly polarized ray, can interfere and appear as elliptically polarized in the detector [28]. These interferences are the depolarization effect and the magnitude depends on the angle of incidence. Depolarization contributes to errors in experimental data and is ideally close to zero for ellipsometry measurements. The depolarization can be reduced by changing the interface at the backside of a sample such that the light is scattered rather than reflected. Surface roughening can be done chemically or mechanically depending on the material and the degree of roughening that is needed to scatter light at the backside and minimize the depolarization. The depolarization for the 2sp substrate shown in Figure 9 is 0 % for small angles of incidence but increases to 4 % at larger angles of incidence. The 1sp substrate

shown in Figure 8 shows depolarization that is mostly independent of the angle of incidence. The magnitude decreases for the 1sp substrate from 2 % at 0.5 eV to 0 % above 2 eV at all angles of incidence. Above 5.5 eV the data becomes noisy due to lost intensity in the Xenon lamp at energies on the tail end of the blackbody spectrum. The 1sp samples did not require further roughening since the depolarization is already near 0 % for all incidence angles, see Figure 8 and 9 to compare.

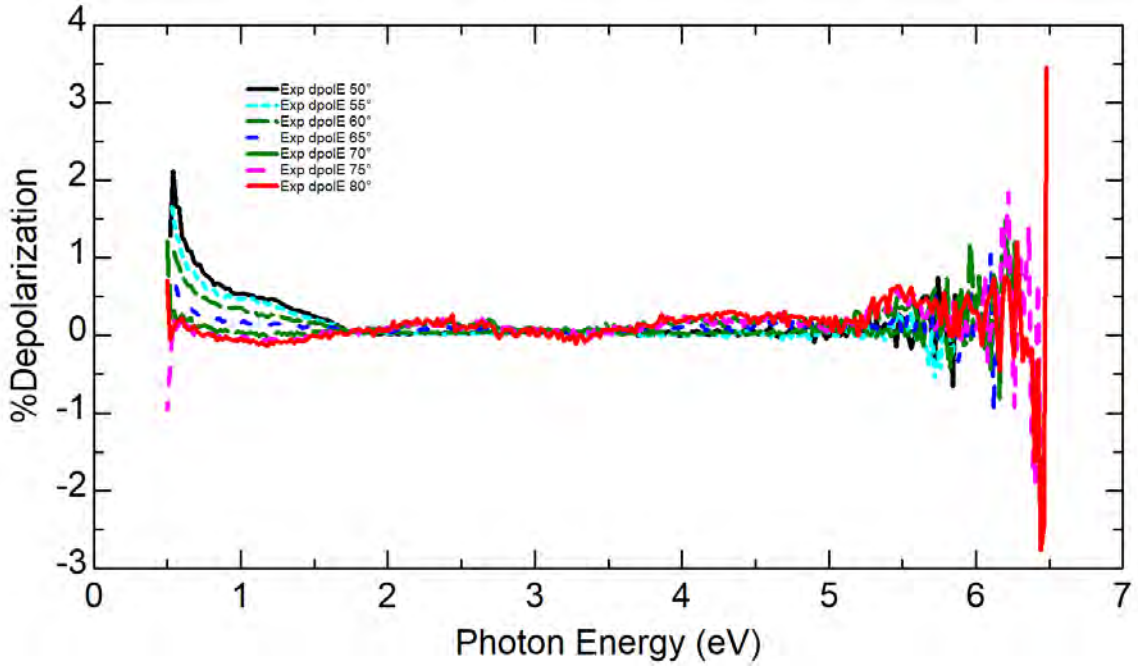

Figure 8: The depolarization for a 1sp calcium fluoride sample at angles of incidence ranging from 50° to 80°.

MTI Corporation uses the Czochralski (CZ) method for bulk calcium fluoride crystal growth. The process begins with a calcium fluoride powder purchased from an unidentified vendor and then the CZ method is used to produce bulk calcium fluoride substrates. For structural verification they use x-ray diffraction to determine the crystal orientation and cuts are made using a wire saw. The substrate is then polished by grinding and chemical mechanical polishing (CMP). We discuss the effect of the polishing method on the substrate

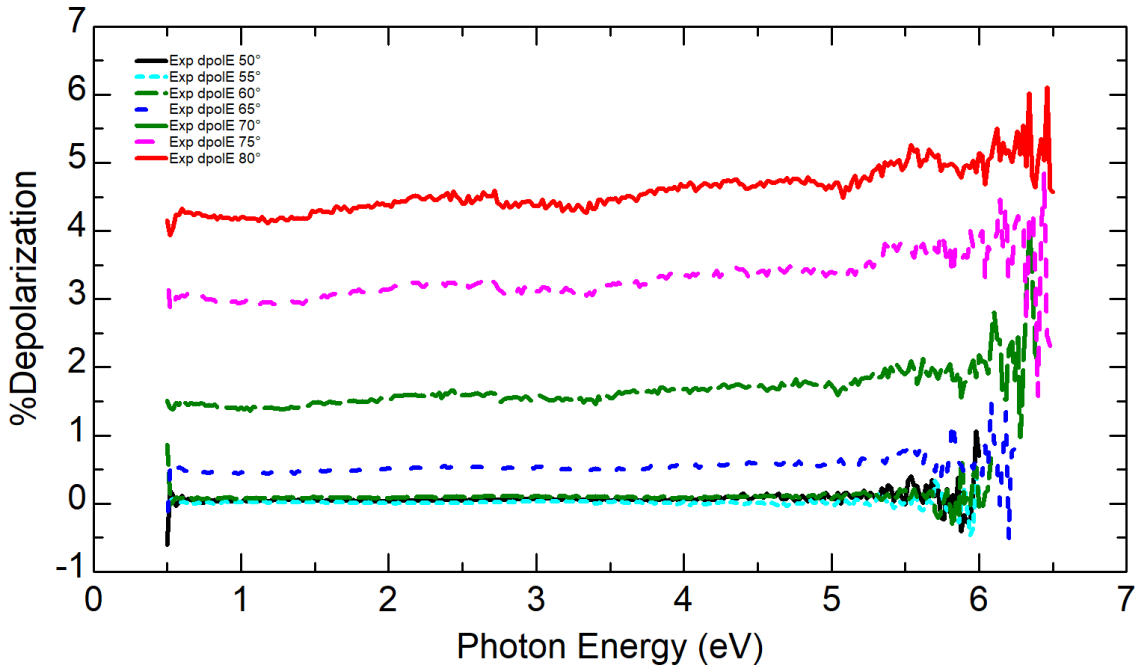

Figure 9: The depolarization for a 2sp calcium fluoride sample at angles of incidence ranging from 50° to 80°.

surface since in the visible spectra there is a negative $\langle \epsilon_2 \rangle$ around 7 eV indicating the presence of a surface layer with a larger refractive index than the bulk substrate. The CZ method uses a seed crystal that is inserted into a crucible containing a molten element and then slowly pulled and rotated until the crystal reaches the desired diameter. The crystallization occurs as the seed is pulled away from the molten element due to the temperature gradient that allows the molten element to cool and crystallize according to the seed structure. The process uses high temperatures and is done inside of a chamber that is evacuated or filled with an inert gas to prevent oxidation of system components that would introduce impurities into the crystal. The quality of the crystal depends on the purity of the seed crystal and melt as well as the rate of pulling and rotation. The temperature and the rate of pulling and rotation are typically controlled digitally to ensure accuracy and consistency.

4.2 X-Ray Diffraction of Calcium Fluoride

To verify the surface orientation and lattice spacing the bulk crystals were measured using XRD across 2θ from 10° to 100°. Similar scans were taken for two powders: 99.95% and 99.99% pure CaF_2 powders. The bulk crystals were placed in the center of the sample stage and held in place with clips. The powder grains will have random orientations in the dish and because of this we observe diffraction peaks from a variety of Bragg planes including the (200) and (111) planes. The (100) diffraction peak is forbidden by selection rules for fluorite structures that eliminates Miller indices which are mixed, not all even or all odd [3]. The bulk (100) and (111) CaF_2 substrates are expected to have diffraction peaks only for the (200) and (111) planes, respectively. Because the powders will show diffraction peaks for many planes we can compare the 2θ peak positions to confirm the surface orientations for the bulk substrates. Additional peaks would indicate that the samples may be polycrystalline or full of impurities. The Miller indices were matched using the ICDD PDF card database (reference code: 00-035-0816). The comparison shows that the peak positions for the bulk (100) and (111) CaF_2 do correspond to the expected Bragg planes and there are no other peaks that would indicate a polycrystalline structure or high concentrations of impurities. The plane spacing, d_{hkl}, was found using (5) and then the lattice spacing was calculated from the relationship for cubic crystals shown in equation (7) [3]. Figure 10 shows the diffraction patterns for the powders and bulk substrates with labeled Miller indices.

4.3 Optical Constants of Calcium Fluoride

Spectroscopic ellipsometry (SE) data was measured using three J.A. Woollam Co., Inc. ellipsometers: the IR-VASE Mark II ellipsometer, the V-VASE ellipsometer, and the VUV-VASE

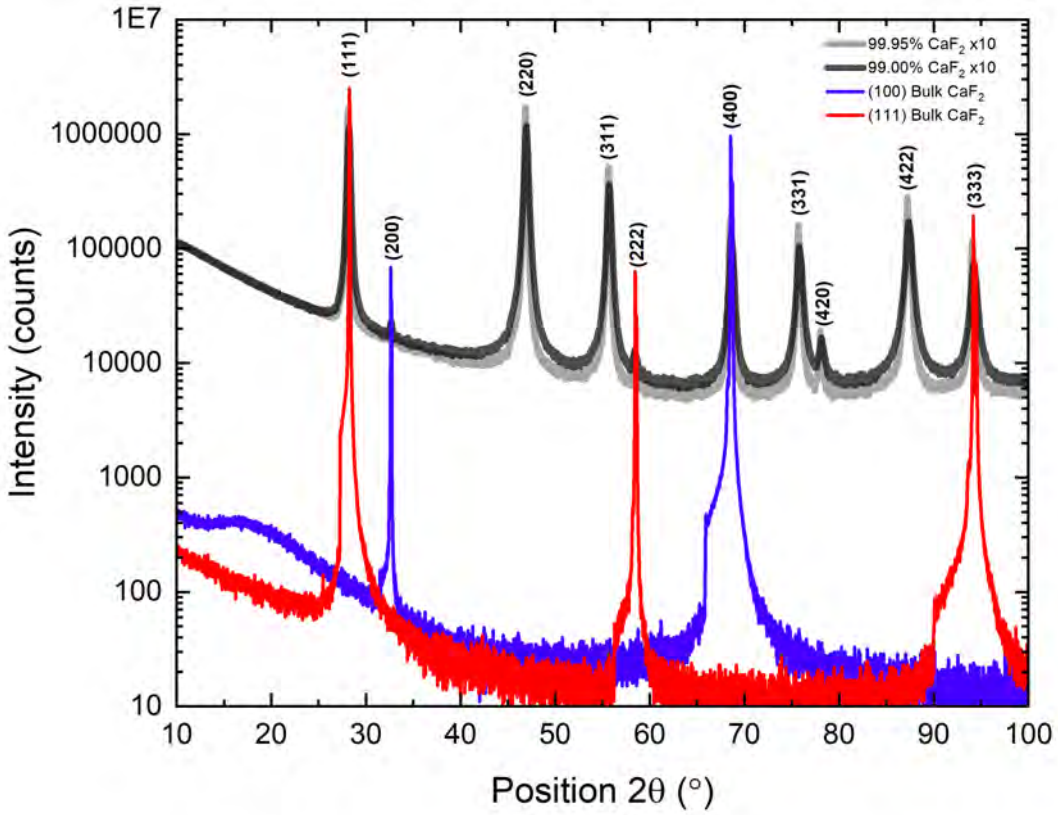

Figure 10: The powder data is magnified by 10x for comparison with the bulk spectra. The 2θ peak positions and magnitudes of the (100) and (111) bulk crystals indicate that the substrates are highly crystalline and lack impurities.

ellipsometer. To find the best acquisition parameters for infrared measurements several scans were taken on the IR-VASE using different resolutions. This was done to resolve the sharp TO phonon peak and minimize the signal to noise ratio, see Figure 11. The 1 cm^{-1} scan has the lowest low signal to noise ratio and anything larger than 4 cm^{-1} did not fully resolve the sharp phonon peak. The data presented here was obtained using 2 cm^{-1} resolution with 1 measurement cycle and a zone averaged polarizer and analyzer. The compensator used 15 positions per cycle and 50 scans were taken per compensator position. The bandwidth was 0.001 μm. Infrared data was taken at angles of incidence 50°, 60°, and 70° for calcium fluoride (100) and (111) 1sp substrates.

Measurments on the V-VASE were collected using 50 revolutions per measurement and employing the AutoRetarder and zone averaged polarizer. Measurements using the VUV-VASE by collaborators at the University of Nebraska Lincoln. Scans by the VUV-VASE measure eleven elements of the Mueller Matrix and they employ an AutoRetarder and zone averaged polarizer. The VUV data was taken with 10 revolutions per measurement. The data in this region is smooth and does not have any sharp features to resolve therefore it is reasonable to use a smaller step size and reduce the overall scan time. Visible and VUV-VASE data was collected at angles of incidence 50°, 60°, and 70° for calcium fluoride (100) and (111) 1sp substrates.

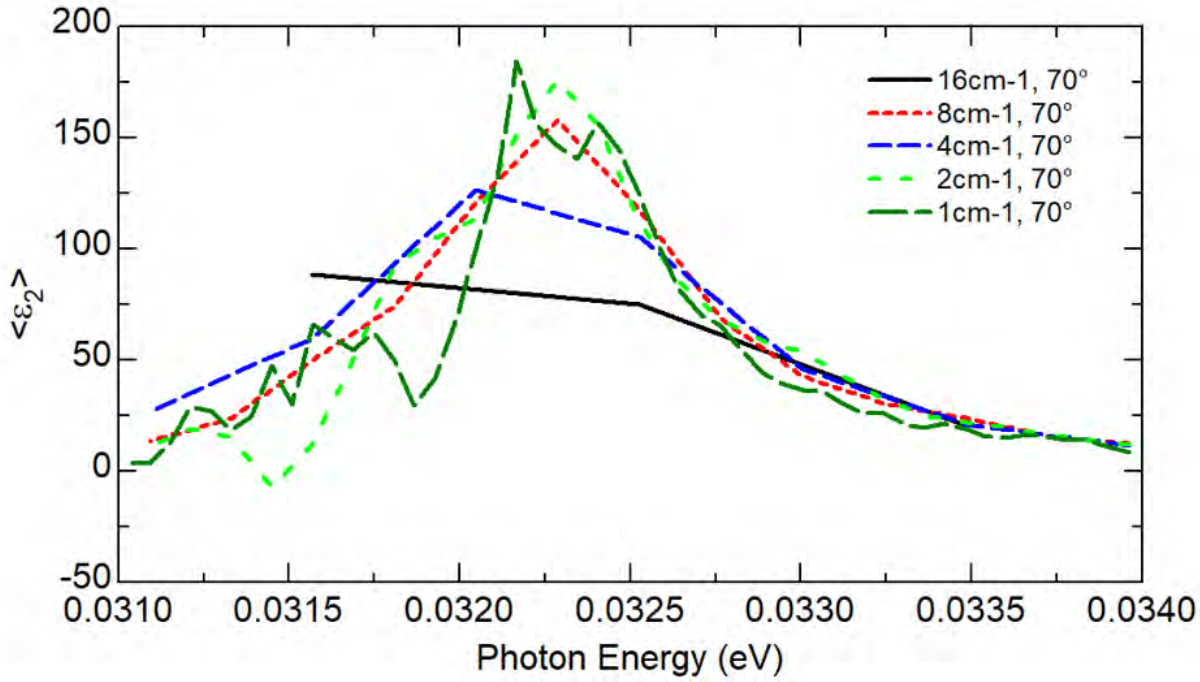

Figure 11: The TO phonon peak in CaF_2 (111) measured using different resolutions.

The data from each ellipsometer was modeled independently using the associated J.A. Woollam Co. software (WVASE32) and then merged to obtain the optical constants across a continuous spectrum at several angles of incidence from 50° to 70°. The VUV-VASE

ellipsometer provided data for eleven elements of the Mueller Matrix, but because CaF_2 is an isotropic structure the off-diagonal blocks of the Muller Matrix are zero and therefore they are not considered in this analysis [40]. We describe the experimental data using a KK consistent model and with fitting parameters that are adjusted to minimize the mean square error (MSE). Results for the CaF_2 (111) and (100) bulk substrates are expected to be the same due to the fluorite structure being isotropic. For CaF_2 (100) $\lambda_{LO} = 20.82$ μm and $\lambda_{TO} = 38.48$ μm (259.2 $cm^{-1} \pm 0.249$ cm^{-1}). For CaF_2 (111) $\lambda_{LO} = 20.95$ μm and $\lambda_{TO} = 38.23$ μm (260.5 $cm^{-1} \pm 0.160$ cm^{-1}). IR data also shows a dip in the reststrahlen band attributed to two phonon absorption. Visible data shows normal dispersion and zero absorption which is expected since this is within the transparent region of the material. In near UV data we observe a small negative pseudo-absorption in $\langle \epsilon_2 \rangle$. VUV ellipsometry is more sensitive to thin films and this non-physical result in the pseudo-dielectric function is attributed to the presence of a surface layer with a higher refractive index than the substrate.

4.4 Analysis and Results

The optical response for two 10 x 10 x 1 mm single-side polished CaF_2 (111) and CaF_2 (100) bulk samples over the range 0.14 to 40 μm is reported here and compared with previous optical data from [1]. Infrared and near UV data was analyzed separately and then the results from each region were merged to cover the full spectral range.

IR data was measured for angles of incidence 50°, 60°, and 70° from 1.5 to 40 μm using the IR-VASE Mark II and fitting was done using the associated WVASE software. Infrared data for the ellipsometric angle Ψ shows the reststrahlen band, a region of high reflectivity occurring between the IR active phonon modes. The infrared active modes are the TO and

LO phonons. According to the LDS relationship given in equation (26) the TO mode is observed in ϵ_2 and the LO mode is seen as a peak in the imaginary part of the loss function, $\mathrm{Im}(\epsilon^{-1})$. The same analysis is used for both CaF_2 (111) and CaF_2 (100) substrates. CaF_2 is an isotropic structure and as expected the optical constants and phonon modes for the (111) and (100) substrate orientations were found to be the same within the experimental uncertainty of 1%.

The experimental data was modeled using two Lorentzian oscillators, a variable and then fixed ϵ_S offset, and a fixed UV pole. The first Lorentzian describes the general structure of the reststrahlen band and is commonly used for modeling infrared phonon modes [30]. A second Lorentzian with anharmonic broadening describes a dip in the reststrahlen band that is associated with two phonon absorption. The model describes ellipsometric angles Ψ and Δ and the pseudo-dielectric function. The model represents the complex dielectric function (19) since dielectric polarization is related to the dielectric constant by the relationship (21). The complex refractive index is related to the dielectric constant in (20) [28]. The absorption peak in ϵ_2 corresponds to the TO phonon mode and occurs at the transition from high to low reflectivity. The fitting parameters for the frequency ω, amplitude A, and broadening Γ, are listed in table 2. The first Lorentzian is associated with the TO pole and the fitting parameters are labeled with the TO subscript. The second Lorentzian associated with the two phonon absorption is labeled with a "2ph" subscript. The second Lorentzian is anharmonically broadened with the parameter C. The parameters for the LO mode can be determined by preforming an alternative fit using the Lowndes model that describes the TO and LO poles.

The restrahlen band is a region of high reflectivity that appears between the lattice

Table 2: Infrared spectrum fit parameters and optical constants for calcium fluoride (100) and (111) substrates compared to literature values tabulated in the Handbook of Optical Constants of Solids II [1].

	(100)	(111)	HOC.II
ϵ_∞	1.991 ± 0.001	1.973 ± 0.001	2.045
A_{TO}	4.418 ± 0.029	4.161 ± 0.021	
ϵ_s	6.409 ± 0.001	6.134 ± 0.001	
ω_{TO} [cm^{-1}]	259.2 ± 0.249	260.5 ± 0.160	257
Γ_{TO} [cm^{-1}]	4.198 ± 0.465	4.001 ± 0.294	
ω_{2ph} [cm^{-1}]	333.7 ± 1.490	330.99 ± 1.640	328
Γ_{2ph} [cm^{-1}]	75.53 ± 3.560	103.1 ± 2.640	
C_{2ph} [cm^{-1}]	0.289 ± 0.025	0.121 ± 0.121	

resonant frequencies and in isotropic materials the p and s components are totally reflected [30]. At the TO frequency the reflectivity increases and then remains high until the LO frequency where the reflectivity drops off again. The band is seen in the ellipsometric angle Ψ and is plotted for CaF_2 (100) and (100) substrates in Figures 12 and 13. The exact onset of reflectivity depends on the angle of incidence but the TO and LO mode frequencies do not. The figures for both substrates show that the onset of reflectivity is lower at larger angles of incidence. In the band of high reflectivity ellipsometry measurements are highly sensitive to small absorption processes and the dip in the restrahlen band near 33 μm that is attributed to two phonon absorption in the lattice [1]. The dip is seen in both the (100) and (111) substrates indicating that it is not an artifact since the feature is independent of the sample.

The loss function (25) was calculated for CaF_2 (100) and (111) substrates using the infrared dielectric function obtained from the Lorentz model of the experimental data. Shown in Figures 14 and 15 is the dielectric function and magnified loss function to demonstrate the pole positions of the TO and LO phonon modes. The real and imaginary parts follow KK consistency. The magnitude of the loss function is much smaller than the dielectric function

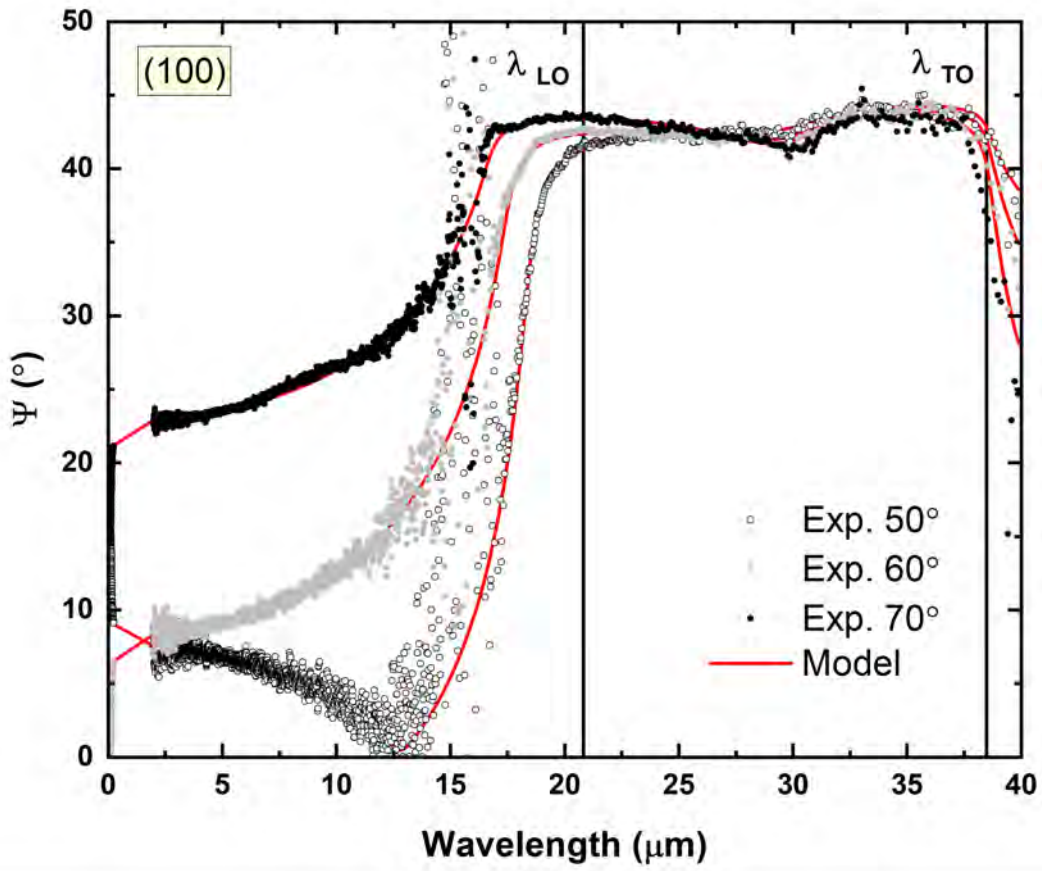

Figure 12: The ellipsometric angle, Ψ plotted versus wavelength shows the restrahlen band at angles of incidence 50°, 60°, and 70° for CaF_2 (100).

due to dielectric loss at the LO mode [30]. The broadening of the two-phonon mode is much larger than that of the TO mode.

Visible and VUV data was collected for angles of incidence 50°, 60°, and 70° from 0.15 to 1.70 μm using the V-VASE and VUV-VASE ellipsometers. The model describing this region started with only a substrate layer and later a surface layer was added to account for a region around 0.18 μm that shows small negative values for $\langle\epsilon_2\rangle$. The substrate layer contains two Gaussian oscillators and a UV pole. The first Gaussian oscillator describes a small peak in the region where $\langle\epsilon_2\rangle$ is negative. The second Gaussian oscillator is used to describe large absorption features that exist outside the measured spectral region towards

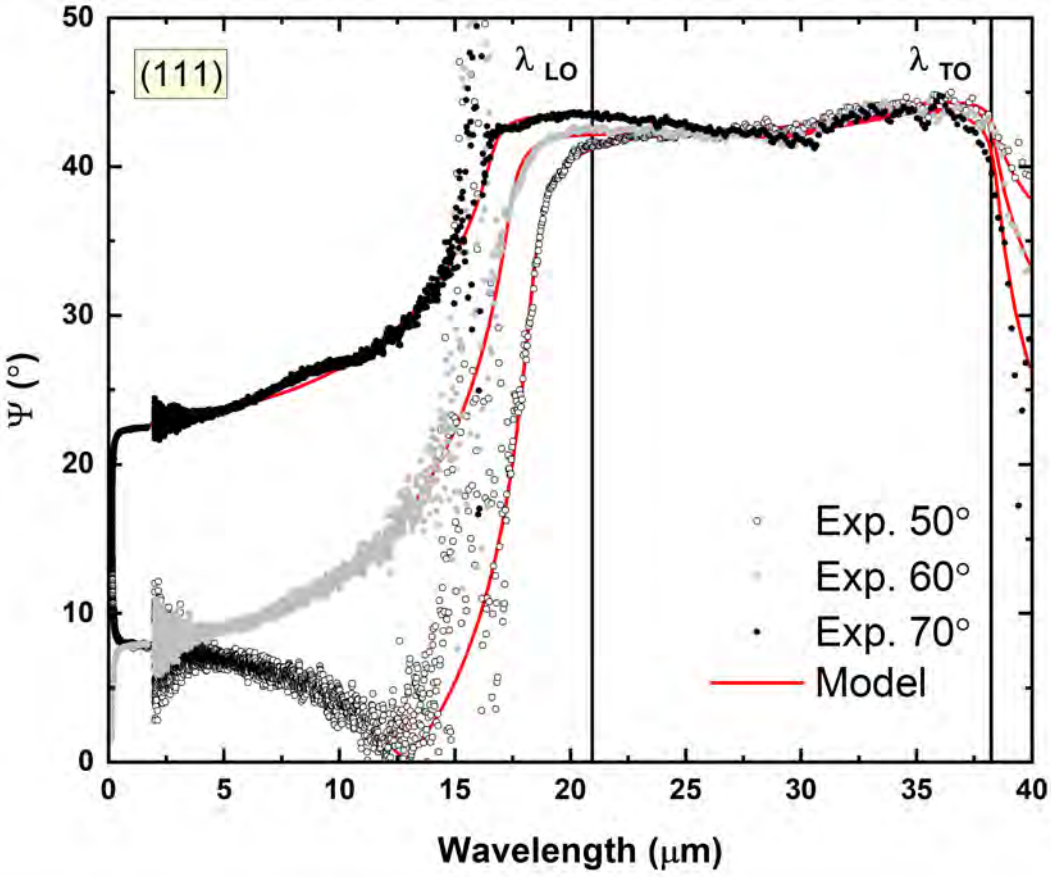

Figure 13: The ellipsometric angle, Ψ plotted versus wavelength shows the restrahlen band at angles of incidence 50°, 60°, and 70° for CaF_2 (111).

the band gap of CaF_2 near 12 eV [8]. Using the UV pole and second Gaussian seems redundant becuase both describe the onset of absorption at higher energies, but the fit quality is significantly improved by including both. Using only the pole above 15 eV to describe the absorption leaves the MSE larger than 7 for the overall fit, but if the second Gaussian is included near 9.5 eV then the MSE is closer to 3.5. Due to the appearance of a negative pseudo-absorption feature a surface layer was added and the layer thickness was included as a fitting parameter. The surface layer thickness was found to be 21 Å and 64 Å for the (100) and (111) substrates, respectively. Adding the surface layer improved agreement with experimental data, reducing the MSE to a value near 3 for both substrates.

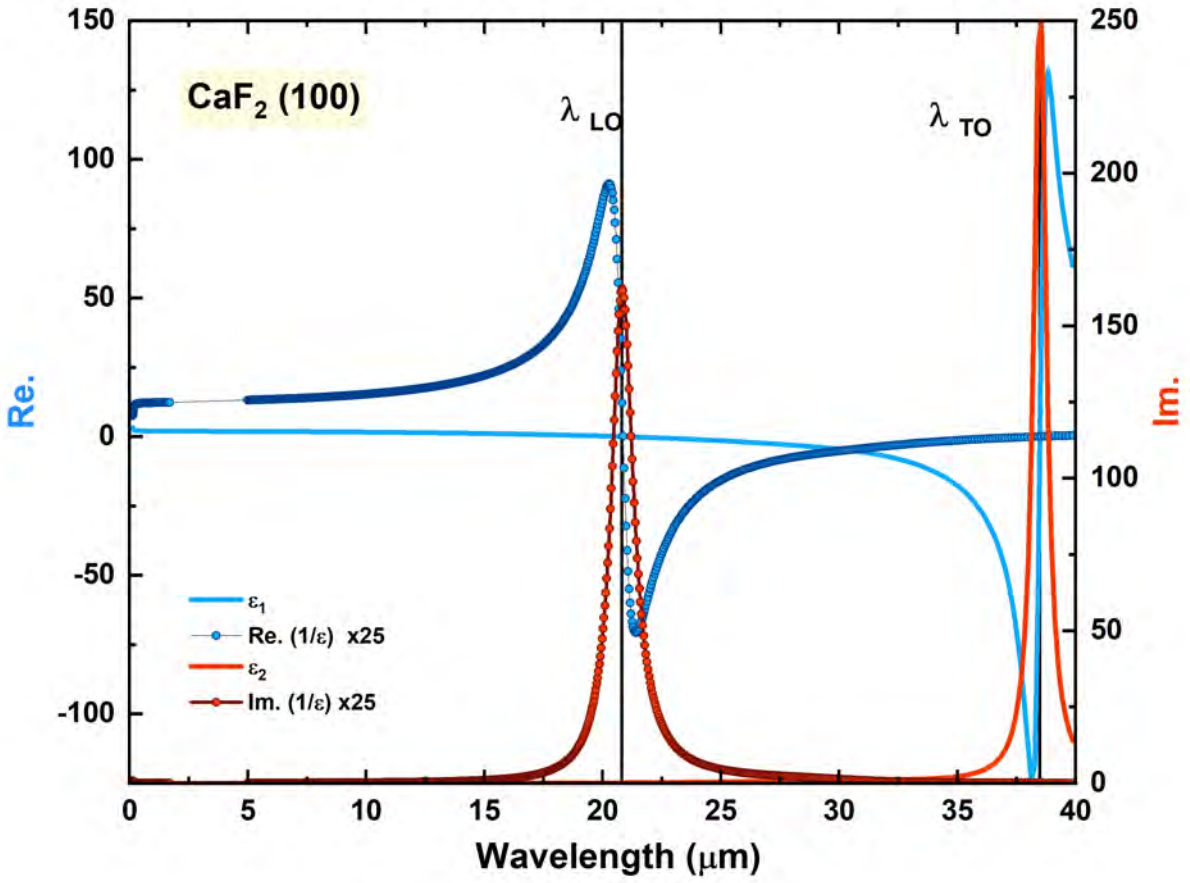

Figure 14: The dielectric function and magnified loss function for CaF_2 (100) with the TO and LO phonon modes labeled.

After minimizing the MSE, the fitted parameters and layer thickness are fixed and a point-by-point fit is used to extract the dielectric function by fitting the layer optical constants. The point-by-point fit gives an acceptable fit because the data in this region is very smooth and the signal to noise ratio is excellent. The fitting parameters for calcium fluoride (100) and (111) are given in table (3). The UV poles are oscillators with zero broadening and are described with a position in energy units, E, and a magnitude, A. The parameters E and A for the UV poles are labeled with a "pole" subscript. The parameters E, A, and Γ for the first Gaussian that describes the small peak in the negative absorption region are labeled

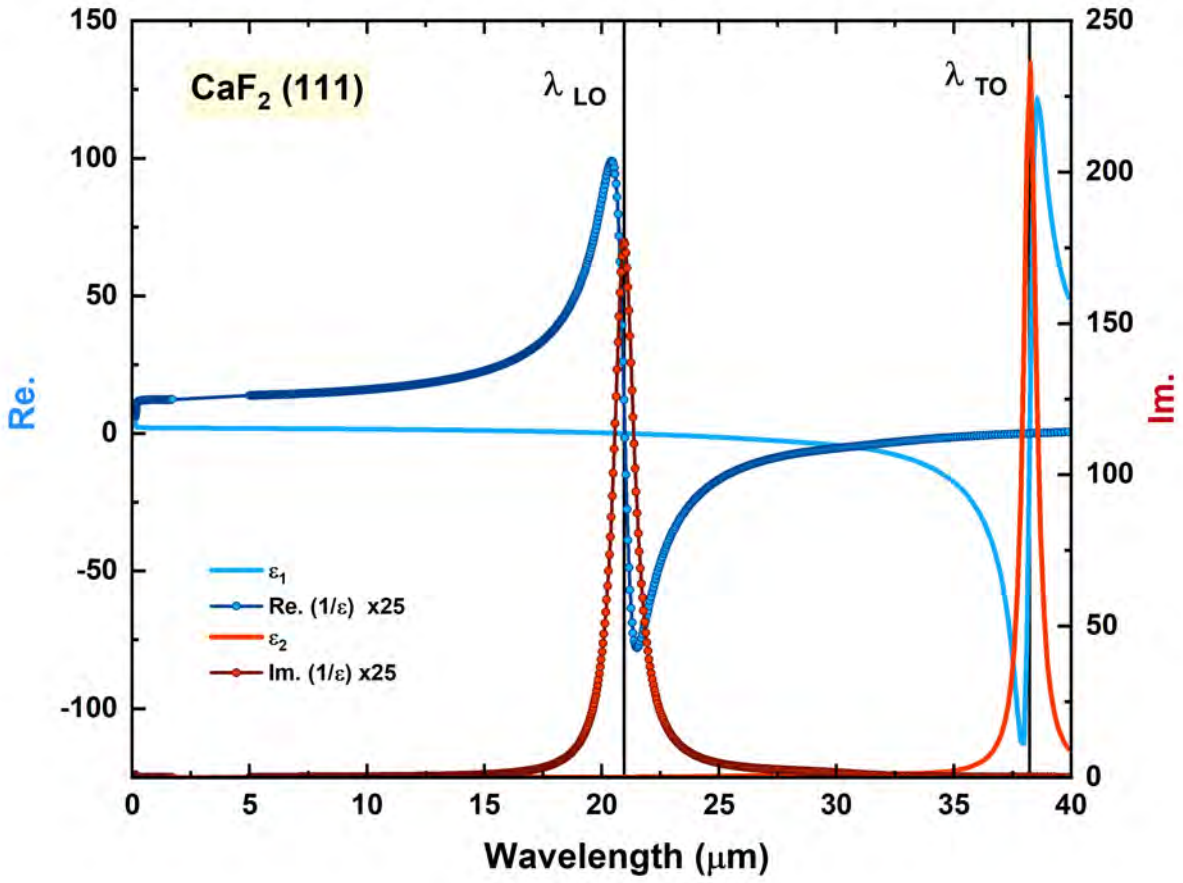

Figure 15: The dielectric function and magnified loss function for CaF_2 (111) with the TO and LO phonon modes labeled.

with the subscript "1". The second Gaussian has parameters A, E, and Γ labeled with the subscript "2".

Table 3: Fitting parameters for CaF_2 (100) and (111) substrates in the visible and VUV spectral region.

-	(100)	(111)
A_{pole}	224.1 ± 2.390	261.0 ± 6.030
E_{pole} [eV]	15.35 ± 0.208	17.62 ± 0.327
A_1	0.993 ± 0.104	0.042 ± 0.009
E_1 [eV]	7.344 ± 0.114	7.593 ± 0.040
Γ_1 [eV]	2.895 ± 0.137	0.442 ± 0.109
A_2	0.904 ± 0.081	3.523 ± 0.152
E_2 [eV]	9.459 ± 0.104	9.560 ± 0.050
Γ_2 [eV]	1.159 ± 0.010	0.775 ± 0.053

Calcium fluoride is transparent in the visible region and we expect that there will be no absorption in this region. The band gap of CaF_2 is near 12 eV which will cause increased absorption at the higher energies that is accounted for in the model with the UV pole that has a position slightly above the band gap energy and magnitude is allowed to vary. The pseudo-dielectric function has a negative absorption region in the imaginary part between 3.5 and 8.5 eV. The magnitude is small between 0.1 and 0.3 and the same feature appears in both samples. This non-physical feature is likely caused by the surface layer having a larger refractive index than the bulk substrate. This is illustrated in Figures 16 and 17 where the value ϵ_1 for the layer is larger than either the substrate or pseudo-dielectric function. When doing the point-by-point fit the value of ϵ_2 is fixed positive to obtain physical optical constants. This is seen in the dashed line that remains constant at 0 until it reaches the high energy region where the onset of absorption begins.

A 1965 study by [41] investigates the presence of colour centers in alkaline earth fluorides and states that contamination by oxygen ions or hydroxyl ions causes the onset of absorption to decrease in the visible and VUV spectra. Defects that arise from the crystal growth process are identified by [4] as oxygen ions filling in for fluorine vacancies in the CaF_2 lattice. In the study by [4] the influence of defects was studied by comparing band energy diagrams for a perfect CaF_2 lattice and ones that contain impurities. The width of the gap E_g for CaF_2 is between the fluorine 2p VB and the CB formed by 3d and 4s states in calcium [4] and there were discrepancies between the calculated gap energy and the observed value reported by [10]. The band energy diagrams show that when there is a single vacancy in the CaF_2 cell the 2p fluorine band narrows slightly and the calcium 3d band splits into three levels [4]. Because of this the onset of the absorption decreases to 7 eV when approaching the gap

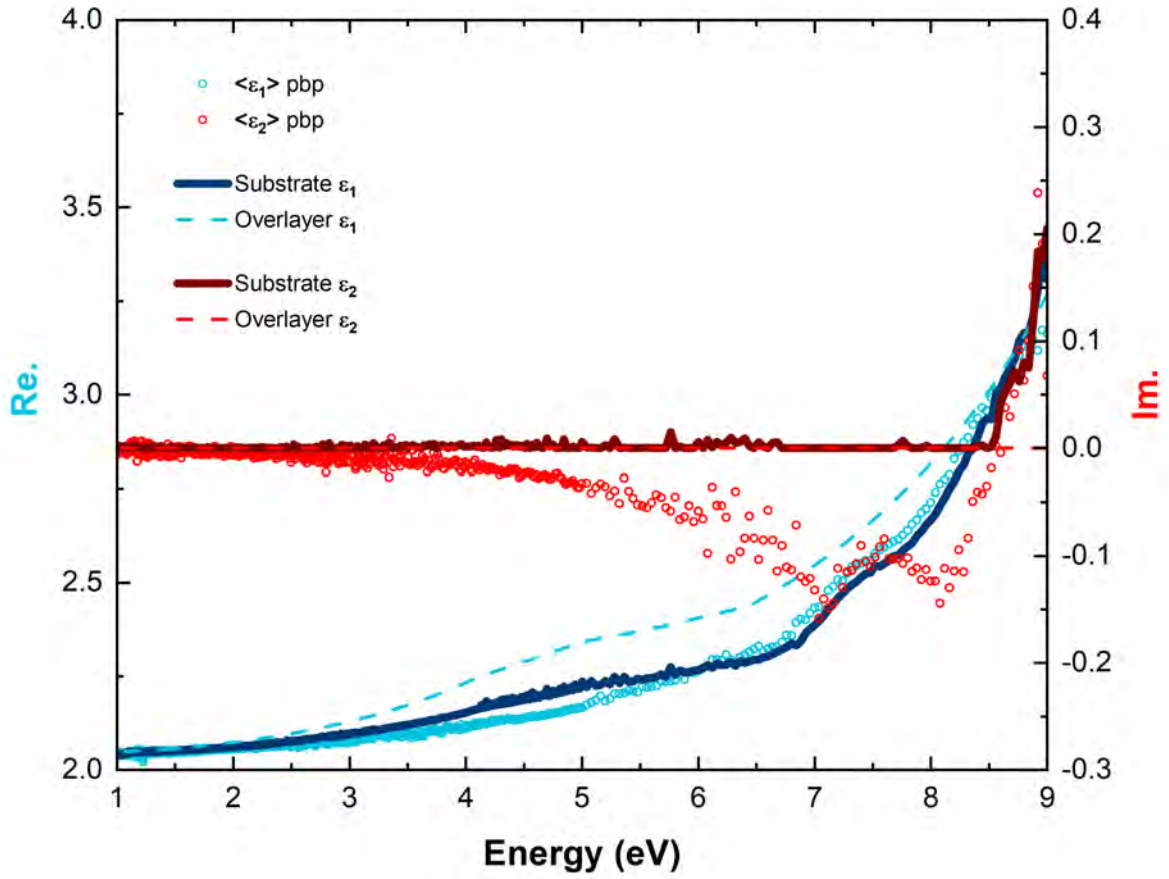

Figure 16: Plot shows the substrate and layer optical constants for CaF_2 (100) alongside the pseudo-dielectric function.

transition [4].

When interpreting the visible and VUV spectra for the MTI Co. CaF_2 substrates we should also consider the influence of vacancies and vacancies filled by oxygen ions, called "color centers". Based on the study from [4] and the IR SE experimental data the onset of absorption around 7.5 eV may be attributed to the presence of color centers in the CaF_2 lattice. The MTI Co. substrates were prepared under identical conditions and experimental data shows the same features for both samples indicating that the early onset of absorption is not an artifact of one sample or the experimental set up. This point is further emphasized in Figures 18 and 19 that compare the optical constants tabulated in [1] with our findings.

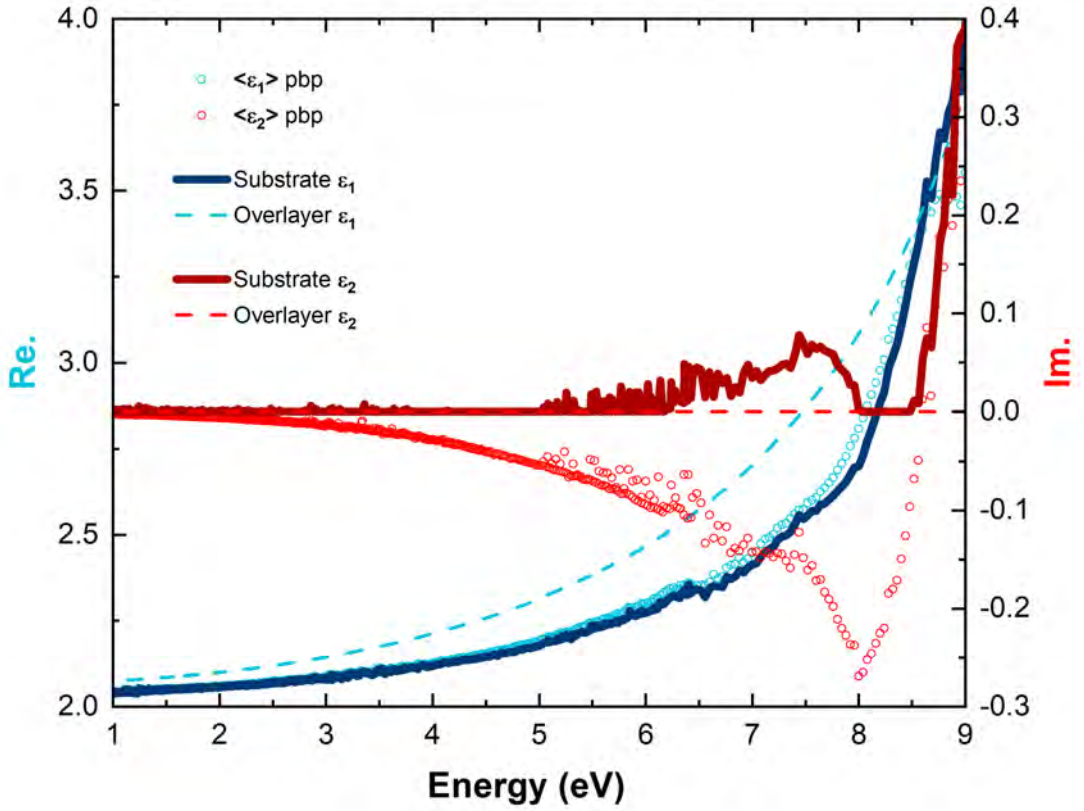

Figure 17: Plot shows the substrate and layer optical constants for CaF_2 (111) alongside the pseudo-dielectric function.

From these figures it is seen that the onset of absorption in the calcium fluoride substrates produced by MTI Co. occurs at lower energies than for the synthetic and natural calcium fluoride crystals measured by [8] and compiled in [1].

In Figures 20 and 21 we show the TO phonon mode for our CaF_2 samples next to the data compiled in [1]. There appears to be a significant difference between the two data sets with the MTI samples appearing about 0.5 meV above the literature values. The broadening and amplitude of the peaks are consistent. CaF_2 (100) has a TO mode about 0.5 meV larger than the literature values. The sample CaF_2 (111) has a TO mode closer to 1 meV larger than the literature values. The study by [8] that comprises the infrared region of the

tabulated CaF_2 optical constants used a Sellmeier dispersion formula to model the dispersion and then calculate the refractive index at 24° [1]. The infrared SE data for our CaF_2 sample was collected in ambient conditions at temperatures near 24°. Therefore, we rule out the possibility that the shift in the TO phonon mode is attributed to a temperature dependence. There is a slightly larger shift from the literature values for the (111) substrate and it was also found by analysis of the visible and VUV data that the (111) sample has a thicker overlayer than the (100) sample. The overlayer in CaF_2 (111) is 64 Å and for CaF_2 (100) the overlayer is 24 Å. There is also a sharper rise in ϵ_1 approaching the abosrption edge than for the (100) sample. Because of these factors it seems reasonable to believe that the shift in the TO phonon mode may be caused by defects in the lattice that have slightly changed the lattice structure and consequently the bond strengths in the unit cell effectively changing the phonon resonant frequency. Another detail that supports this claim is the slight variation in lattice constants between the (100) and (111) samples. The lattice constants of the (100) and (111) were measured at 5.4778(2) Åand 5.4639(8) Å, respectively. The unit cell of calcium fluoride is isotropic and therefore we would expect no difference in lattice constants, but if we consider the influence of defects then it is possible that the lattice constant may change as well.

The merged data is displayed as the complex refractive index, (18), from 0 to 40 μm. In Figures 22 and 23 the experimental data is plotted alongside the compiled tables published in the Handbook of Optical Constants of Solids II [1]. The tables were compiled from reflection and transmission experiments conducted by several groups [8, 9]. Towards longer wavelengths there are fewer data points. The experimental data for the refractive index and extinction coefficient for the commercial CaF_2 bulk substrates agree well with the values

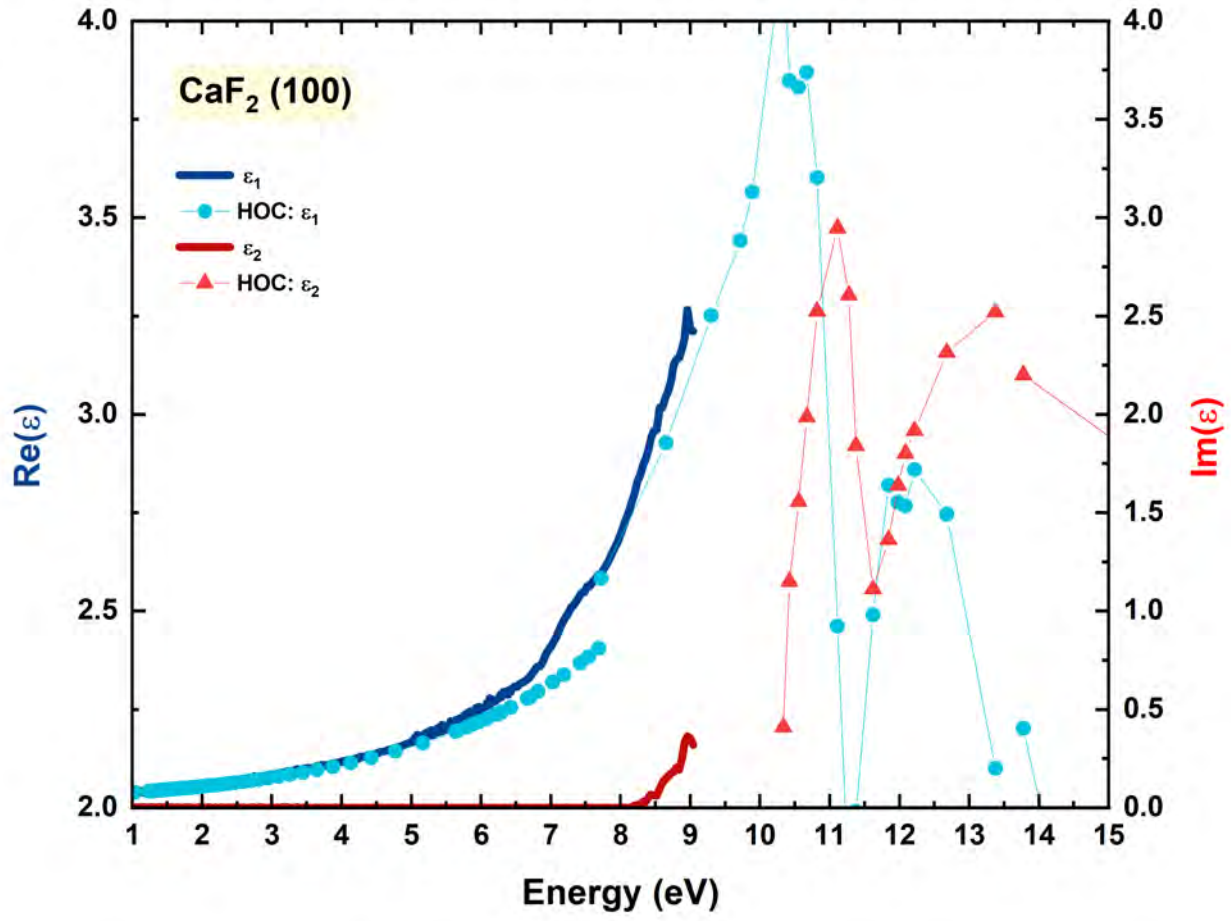

Figure 18: Visible and VUV data for for calcium fluoride (100) manufactured by MTI Co. compared to optical constants tabulated in the Handbook of Optical Constants of Solids II.

published in [1], and shows the slight variation in the resonant frequency for the TO phonon mode. We see that the LO phonon mode occurs where n = k and that the TO phonon mode is at the maximum in the extinction coefficient. Below the LO mode the extinction coefficient is zero and the refractive index approaches a constant value.

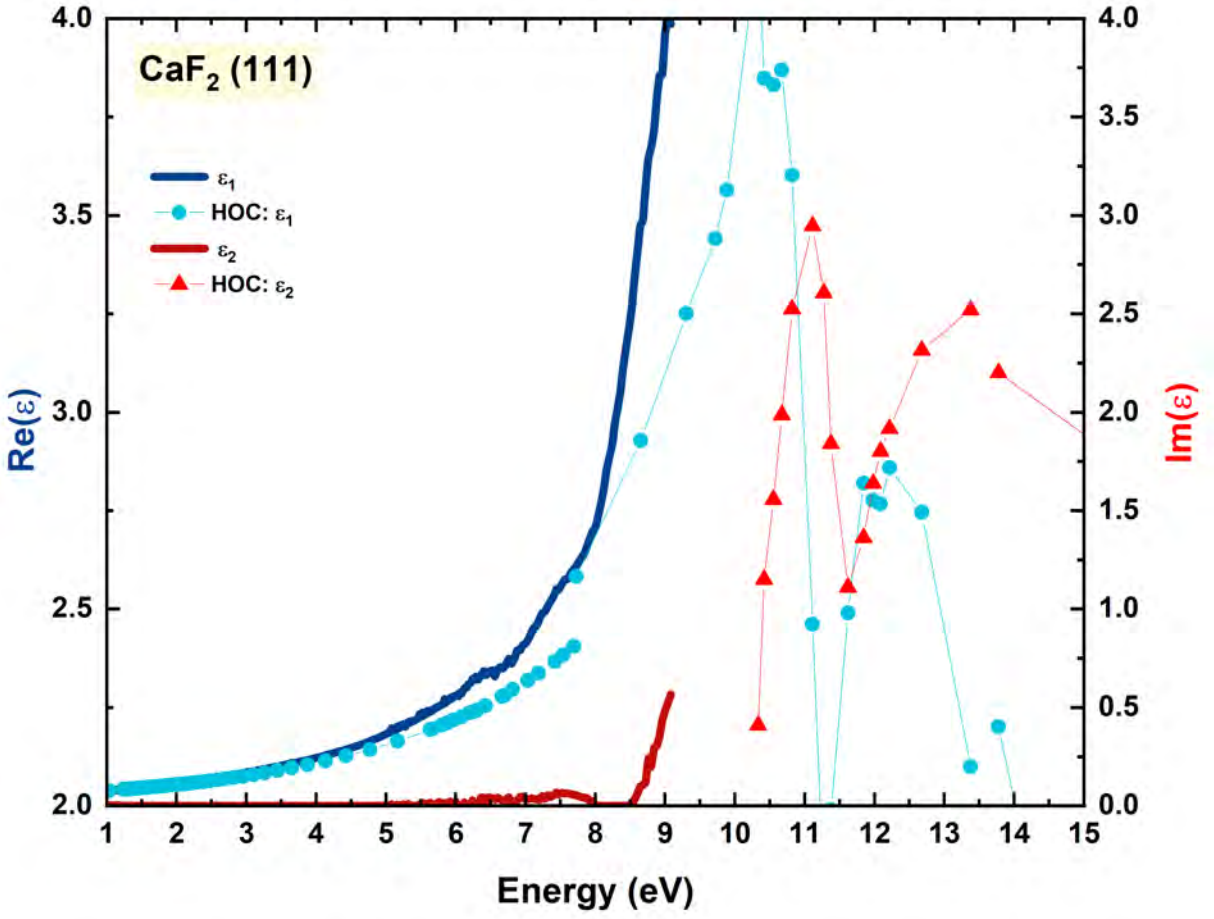

Figure 19: Visible and VUV data for calcium fluoride (111) manufactured by MTI Co. compared to optical constants tabulated in the Handbook of Optical Constants of Solids II.

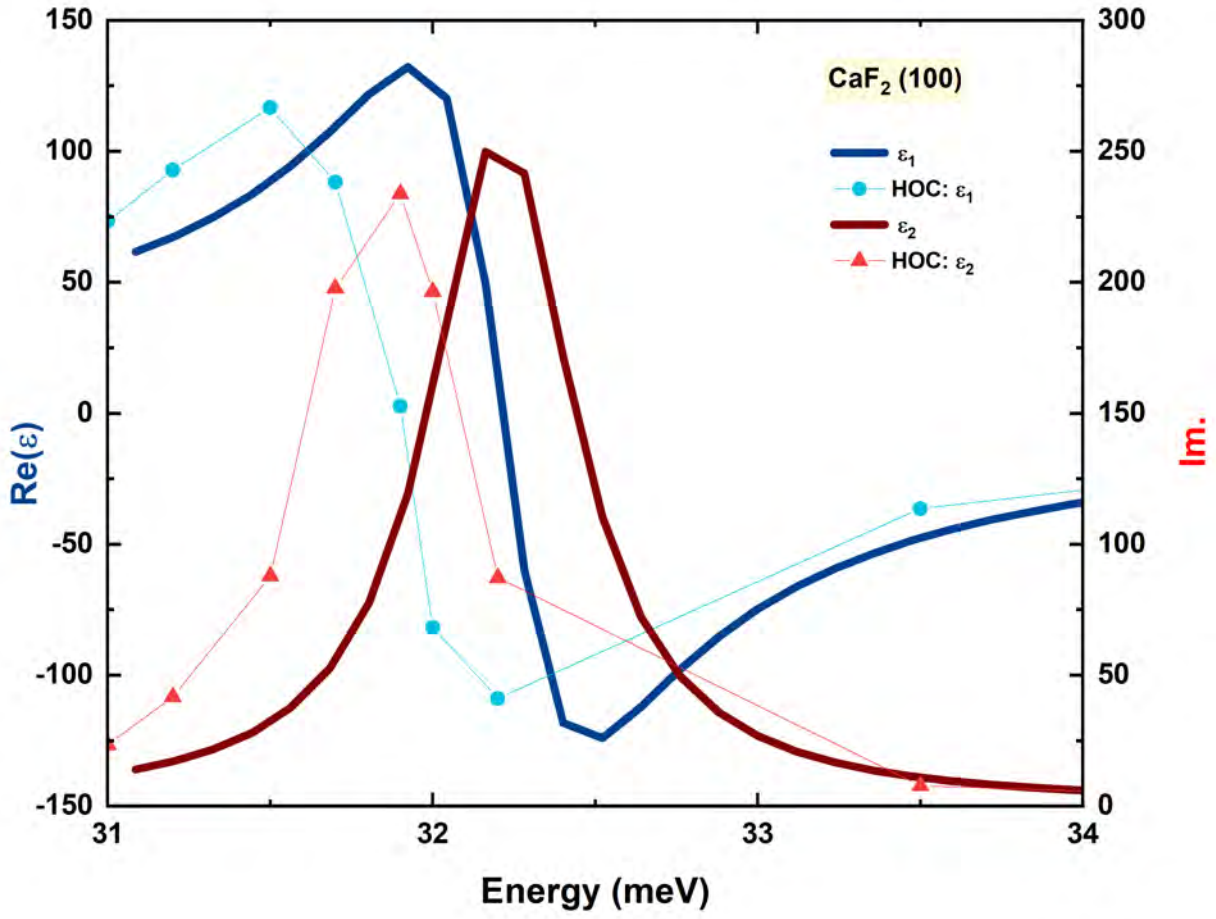

Figure 20: The TO phonon mode for for calcium fluoride (100) manufactured by MTI Co. compared to optical constants tabulated in [1].

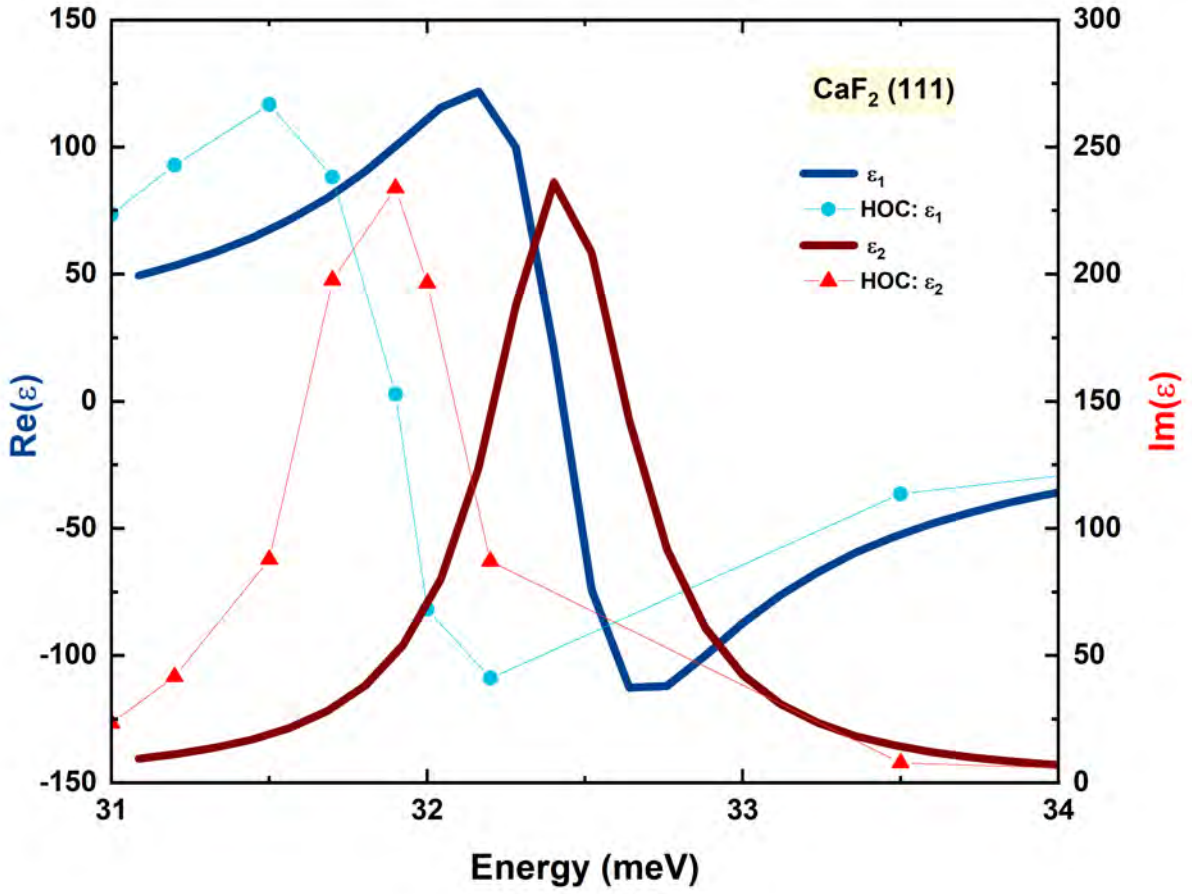

Figure 21: Visible and VUV data for calcium fluoride (111) manufactured by MTI Co. compared to optical constants tabulated in [1].

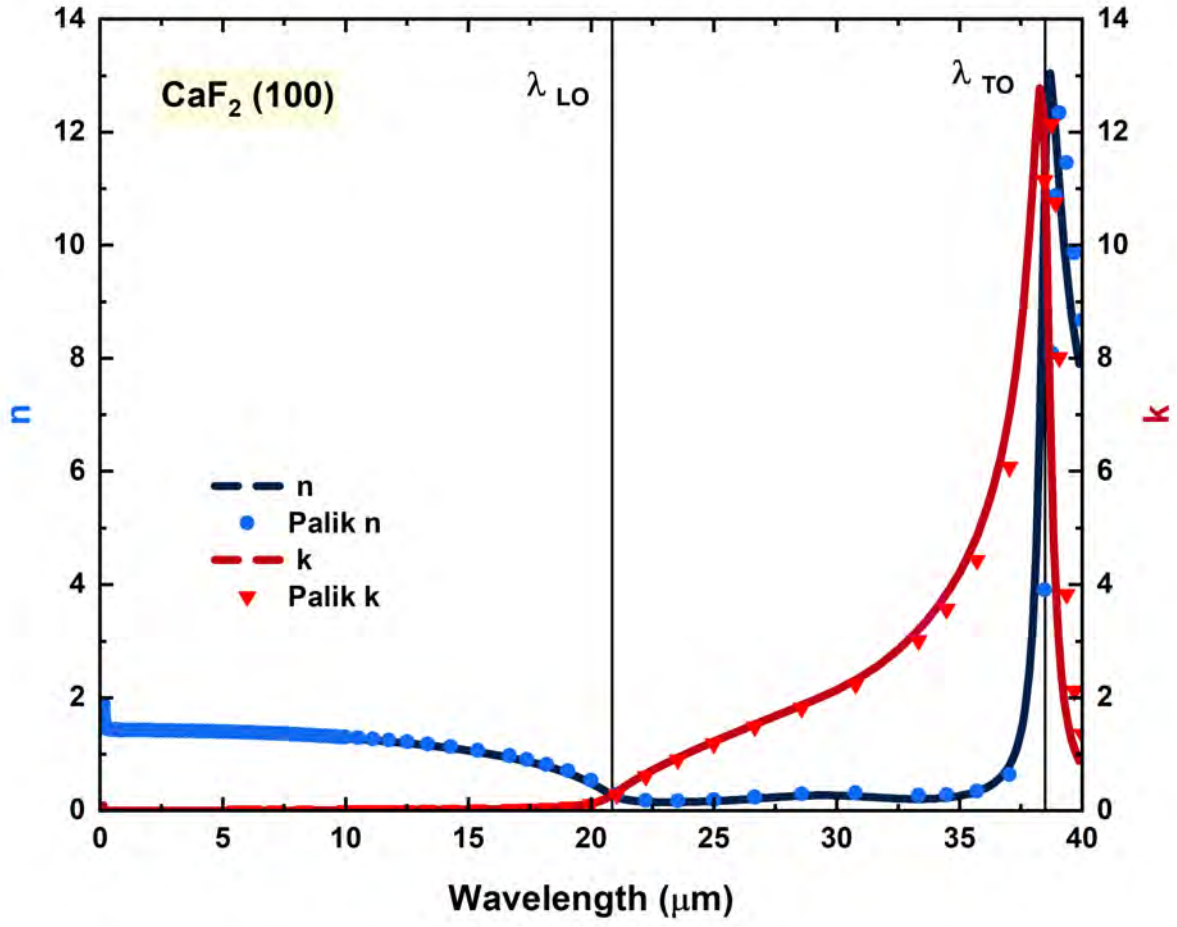

Figure 22: Figure shows the complex refractive index of CaF_2 (100) over the spectral range from 0 - 40 μm.

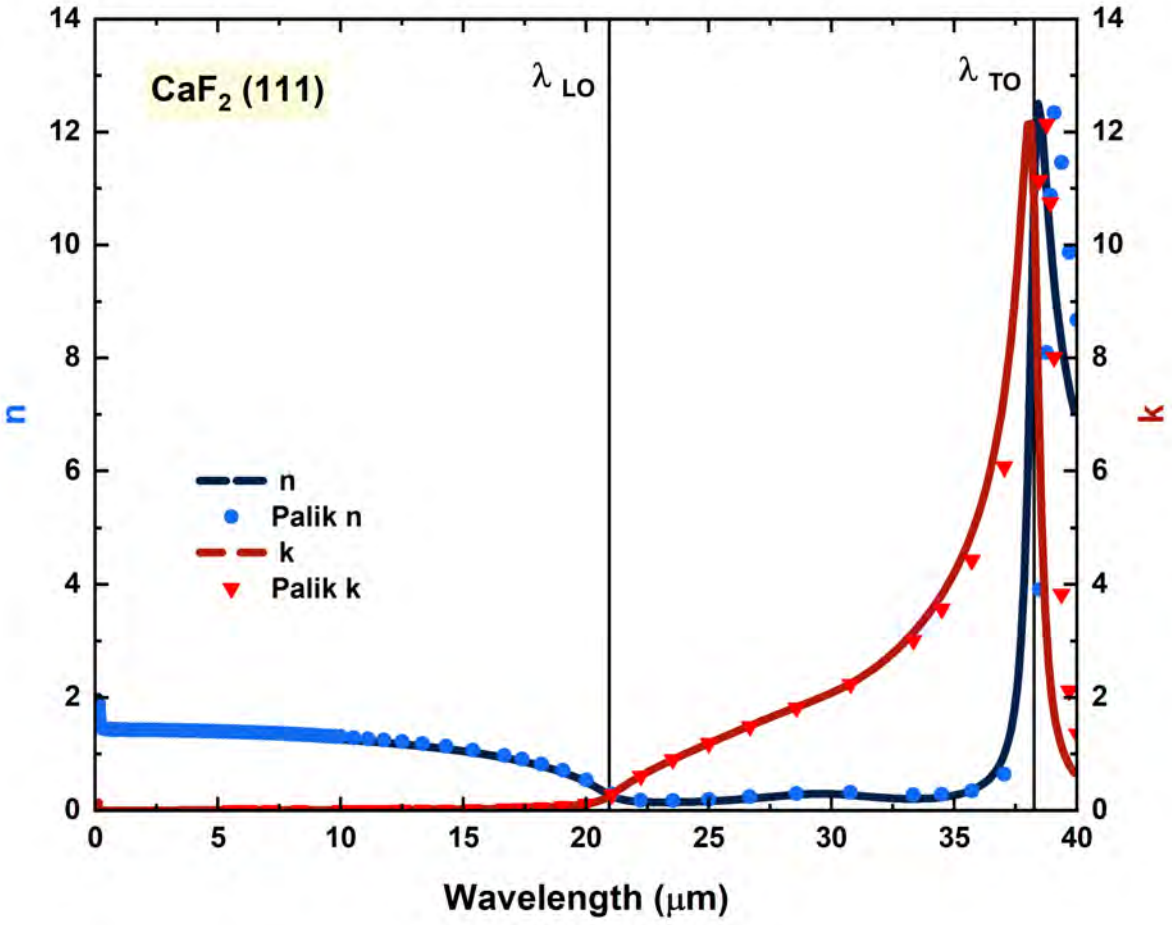

Figure 23: Figure shows the complex refractive index of CaF_2 (111) over the spectral range from 0 - 40 μm.

Because of strong relativistic effects in heavy elements (Darwin shift), the band structure of gray α-Sn is inverted. In comparison to germanium, the Γ_7^- "electron" band is situated between the Γ_8^+ heavy and light hole bands and the Γ_7^+ split-off hole band. It thus becomes a valence band with a negative curvature. In the absence of strain, the Γ_8^+ heavy hole and light "hole" bands are degenerate. This makes α-Sn a gapless semimetal. The heavy hole band is curved like a valence band, while the light "hole" band is a conduction band [20, 18]. Schematics of the band structure can be found in Fig. 1 in [38] or Fig. 1 in [19]. Epitaxial growth of α-Sn on InSb stabilizes the diamond-like crystal structure at room temperature and avoids transformation into the metallic β-Sn phase [42]. The small lattice mismatch of -0.15% between α-Sn and InSb leads to an antisplitting of the Γ_8^+ bands equal to 12 meV [18]. Technically, α-Sn on InSb is a Dirac semimetal [19]. However, this splitting is small compared to the energy scale investigated here. For our purposes, it is sufficient to treat α-Sn on InSb as a topologically trivial zero-gap semimetal. This inverted band structure allows optical interband transitions from the Γ_7^- "electron" band to the Γ_8^+ heavy and light hole bands. A strong infrared $\bar{E}_0$ was recently identified in FTIR ellipsometry measurements of the α-Sn optical constants [19]. A careful analysis of the band structure of α-Sn showed [38] that this infrared peak is mostly due to transitions from Γ_7^- into the Γ_8^+ heavy hole band because of its large effective mass. Transitions into the Γ_8^+ light "hole" band are much weaker due to the smaller effective mass. The purpose of this chapter is to apply the Thomas-Reiche-Kuhn f-sum rule [43, 2, 44] to calculate the heavy hole concentration from the integrated

oscillator strength of the infrared $\bar{E}_0$ peak at 0.41 eV. For a nearly intrinsic (undoped) α-Sn layer, the resulting heavy hole concentrations from 10 to 300 K are in excellent agreement with a degenerate Fermi-Dirac carrier statistics model [38] Depending on the preparation of the InSb substrate before growth, donor or acceptor doping of α-Sn with Sb or In can be achieved. This leads to observable changes in the infrared spectra and the resulting heavy hole concentrations.

The α-Sn films were grown on undoped 1sp InSb (001) substrates (WaferTech Ltd.). The α-Sn layer on sample AE225 was grown on an indium rich c(8x2) reconstruction and the α-Sn layer on sample AE227 was grown on an antimony rich c(4x4) reconstruction. The substrates were gallium-bonded to molybdenum substrate holders. The c(8x2) reconstruction is prepared via atomic hydrogen clean (MBE Komponenten) to remove oxides at 285°C followed by a light anneal at 360°C to smoothen the surface. The cleaning recipe was periodically verified using scanning tunneling microscopy. Temperature measurements are uncalibrated. The c(4x4) reconstruction was prepared by annealing InSb(001)-c(8x2) in a primarily Sb_4 overpressure above 430°C and then rapidly cooling. For growth on both InSb reconstructions, the sample was allowed to cool to room temperature prior to initiation of α-Sn growth. Desired reconstructions were confirmed by RHEED immediately prior to the initiation of α-Sn growth. The α-Sn growth rate was monitored by RHEED oscillations and periodically calibrated by Rutherford Backscattering Spectrometry. Further details on the growth details and chemistry of the alpha-Sn epilayers can be found in [42].

5.1 X-Ray Diffraction of 30 nm Thick Grey Tin on InSb (100)

XRD and HRXRD are used for structural characterization of the grey tin layer in sample AE225. The diffraction pattern of AE225 is compared with the patterns for a β-Sn powder and an InSb (100) bulk substrate. The comparisson confirms that the epilayer is stabilized at room temperature by the InSb substrate becuase there is no strong indication that β-Sn is present in the diffraction pattern. HRXRD is used to confirm the 30 nm layer thickness and determine the out-of-plane lattice constant.

Table 4: Sample descriptions including layer ordering, interface condition and the expected doping type for samples AE225 and AE227 and samples measured previously in [19].

Name	Layers	Type
AE225	30 nm α-Sn / InSb(100) c(8x4)	In rich interface, intrinsic
AE227	30 nm α-Sn / InSb(100) c(4x4)	Sb rich interface, n-type
RAC InSb	70 nm α-Sn / InSb(100) c(8x2)	p-type
RAC CdTe	70 nm α-Sn / CdTe(100) c(2x1)	Intrinsic

A HRXRD (004) symmetric scan was collected for one 30 nm thick α-Sn film on InSb (100) along the z-axis in reciprocal space using a ω-2θ scan. One scan was taken with an open detector (OD) and the other was taken in receiving slit (RS) mode. The OD and RS scans are displayed together in Figure 26. The OD and RS scans were done over the 2θ range from 55° to 58° with 0.88 s time per step and a step size of 0.0006°. The pendellösung fringes are not observable in the OD mode due to a higher detected background and therefore the RS data is used to model the layer thickness. The data was simulated using Epitaxy Smoothfit [24] by entering the layer and substrate material compositions then adjusting parameters for the intensity and layer thickness. The strain is fixed at 100 % because the layer is pseudomorphic.

In Table (5) we compare a few of the predicted diffraction peaks with the experimental

results for sample AE225, 99.95% pure β-Sn powder, and bulk InSb (100). The data shows the expected diffraction peaks for all materials and the relative peak intensity between Bragg planes is consistent with the calculated values provided by VESTA [15]. In addition to the peaks from the samples the BBHD optics produce spectral lines from the W filament and the Cu target. There is a peak near 44° that is seen in the AE225 and InSb (100) spectra attributed to the metal sample holder. The peak does not appear in the β-Sn powder spectra because the β-Sn powder was measured using a different type of sample holder. Due to the close lattice matching of the α-Sn with the InSb substrate the layer peak and the substrate peak are not easily distinguishable. The peak labels for InSb and α-Sn shown in Figure 25 are for calculated 2θ values from (5). The peaks attributed to the sample stage and the incident beam optics are also labeled. In the XRD spectra we observe peaks from the substrate as well as the α-Sn layer. The (200) and (600) peaks are attributed to the substrate due to the selection rules of α-Sn requiring that h+k+l is a multiple of 4 [3]. They are also observed in the bulk InSb (100) sample as further evidence that the peaks are caused by the substrate rather than the layer. The β-Sn powder peaks have been labeled with corresponding Miller Indices. In the AE225 spectra there are two small peaks with intensities less than 100 counts that align with the (112) and (301) orientations of the β-Sn powder. It is possible that small portions of the α-Sn surface have undergone the phase transition. The sample surface has visibly degraded over time and I have noticed patches of discoloration that look like dust on the samples surface since XRD measurements were collected.

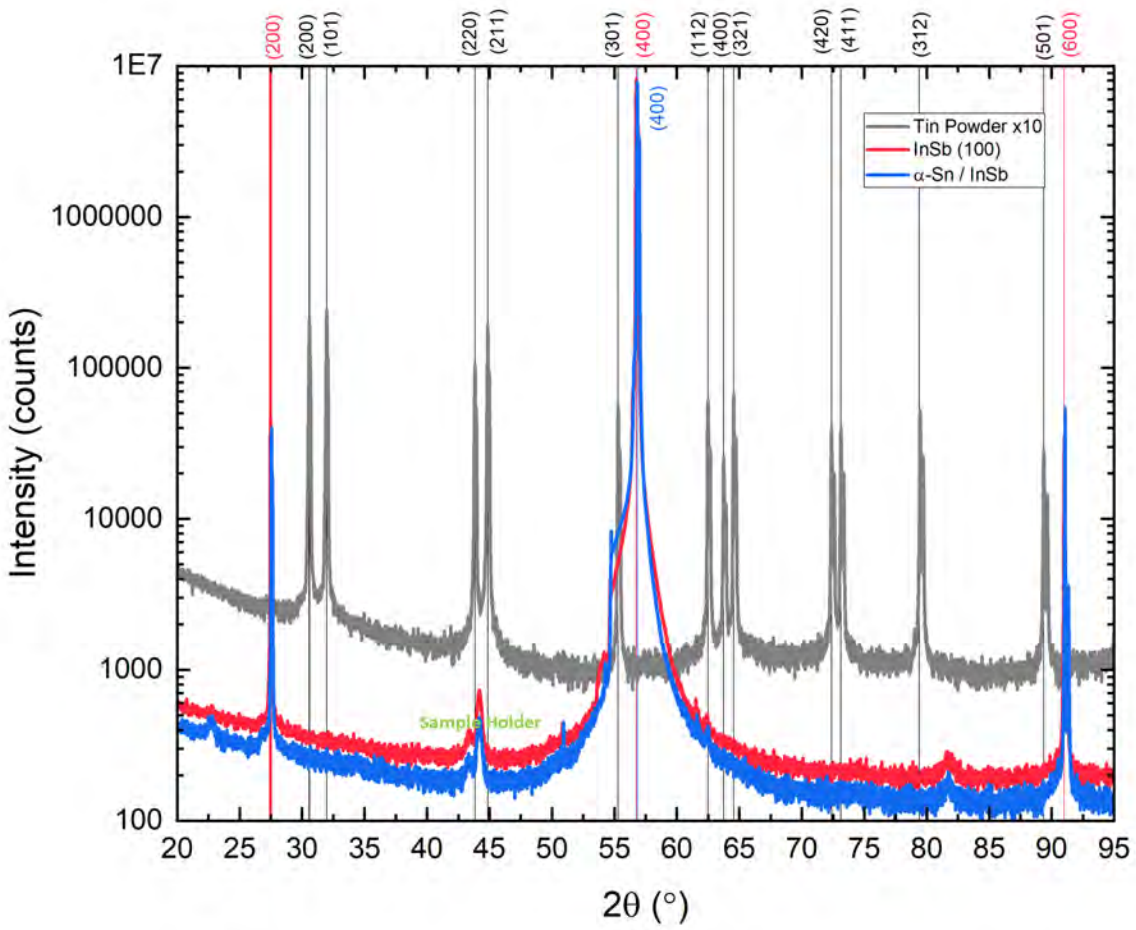

Figure 24: XRD scan of AE225 showing the full 2θ range. We see diffraction peaks from other planes with lower intensity on either side of the (004) peak.

Table 5: XRD results for a selection of diffraction peaks for sample AE225, β-Sn powder, and bulk InSb (100).

Material	Miller Indices	2θ [°] Expt.	2θ [°] VESTA	d [Å] Expt.	a [Å] Expt.
α-Sn	(400)	56.57	56.69	1.626	6.503
InSb	(200)	27.47	27.51	3.244	6.489
	(400)	56.75	56.80	1.621	6.483
	(600)	91.00	91.03	1.080	6.480
β-Sn	(200)	30.68	30.70	2.921	5.841
	(301)	55.30	55.46	1.660	5.249
	(112)	62.66	62.67	1.485	3.638

Table 6: HRXRD experimental results for AE225 including the substrate and layer.

	Miller Indices	2θ [°]	d [Å]	$a_\perp$ [Å]	t [nm]
α-Sn	(400)	56.68	1.622	6.491	29.7 $\pm$ 0.7
InSb	(400)	56.79	1.620	6.479	-

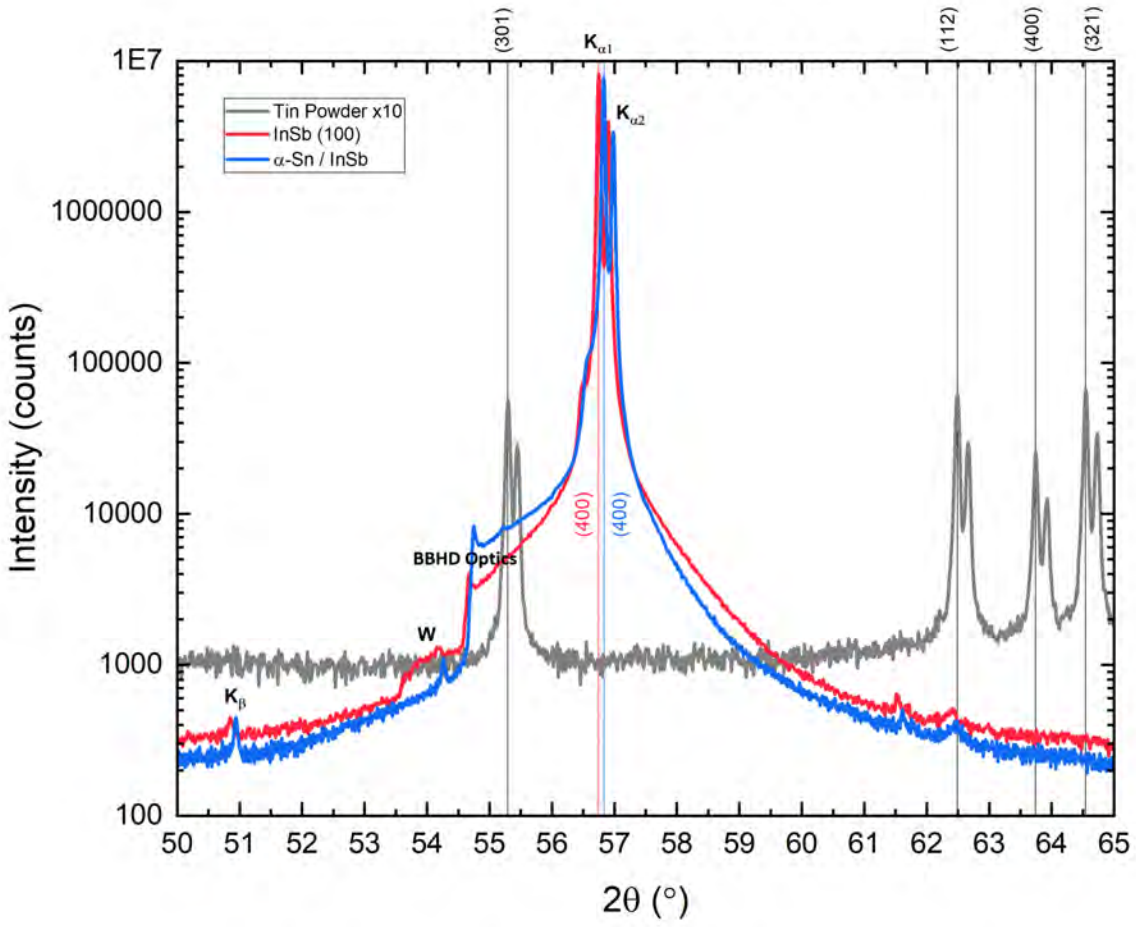

Figure 25: XRD scan of AE225 with a focused range around the (004) InSb substrate peak. Miller indices and spectral lines from the BBHD optics are labeled.

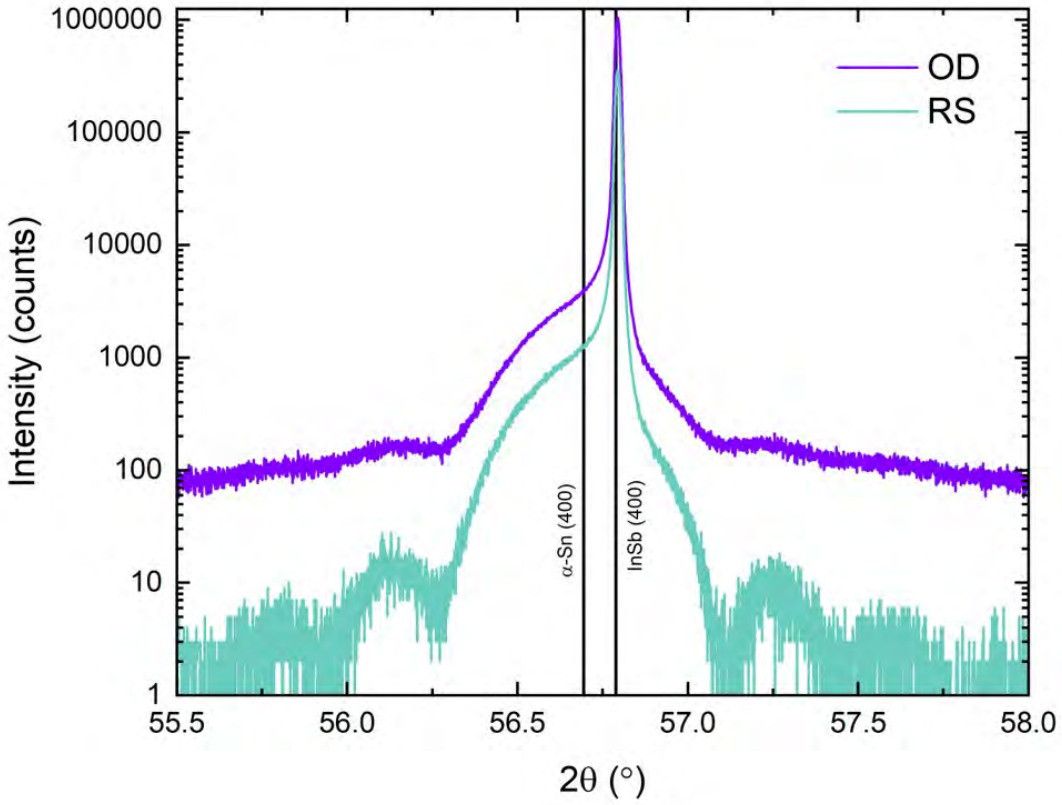

Figure 26: HRXRD spectra of AE225. The plot shows the $\omega - 2\theta$ scan taken using open detector (OD) settings and receiving slit (RS) settings.

5.2 Temperature Dependent Ellipsometry

Low temperature ellipsometry measurements are taken inside a UHV cryostat chamber fitted with with diamond windows that are transparent in the infrared region. The cryostat chamber is mounted on the goniometer and replaces the standard sample mounting stage for the IR-VASE Mark II ellipsometer. The 335 temperature controller displays both the sample temperature (input B) and cryogen space temperature (input A) and is linked to the computer running the data collection software, WVASE-IR. Using the WVASE-IR software an automated series was programmed to run from 300 K down to 10 K in 25 K steps. One ellipsometry scan was taken for each temperature step using 64 cm^{-1} resolution with 2 measurement cycles over the range 0.03 to 0.8 eV. The ellipsometer uses a rotating compensator with 15 positions per cycle and a polarizer at 0° and 90°. To improve the scan quality we took 500 scans per compensator position. To find the best resolution scans were taken at 16 cm^{-1}, 32 cm^{-1}, and 64 cm^{-1} and they are shown together in Figure 28. The 64 cm^{-1} resolution was selected because the $\bar{E}_0$ peak is clearly resolved and there is the highest signal to noise ratio at this resolution. Each scan lasted about 4.5 hours and the series was run over the course of several days.

During the temperature series measurments we have noticed the formation of a layer that increases in thickness over time. This is seen as an increasing slope at low temperatures for energies above 0.2 eV in ϵ_2. Without a surface layer the slope should not change, and because the slope depends on temperature it is likely that the surface layer is caused by deposition of a contamination such as water vapor or hydrogen on the samples surface over

time. This issue can be minimized by baking the sample overnight, evacuating the chamber to sufficiently low pressures, or temperature cycling where the sample is heated and cooled repeatedly. These steps can reduce the gas pressure within the chamber or force the particles to deposit on the chamber walls rather than the sample surface. These steps were not taken because they require heating above room temperature or heating for long periods of time which increases the chances of a phase transition.

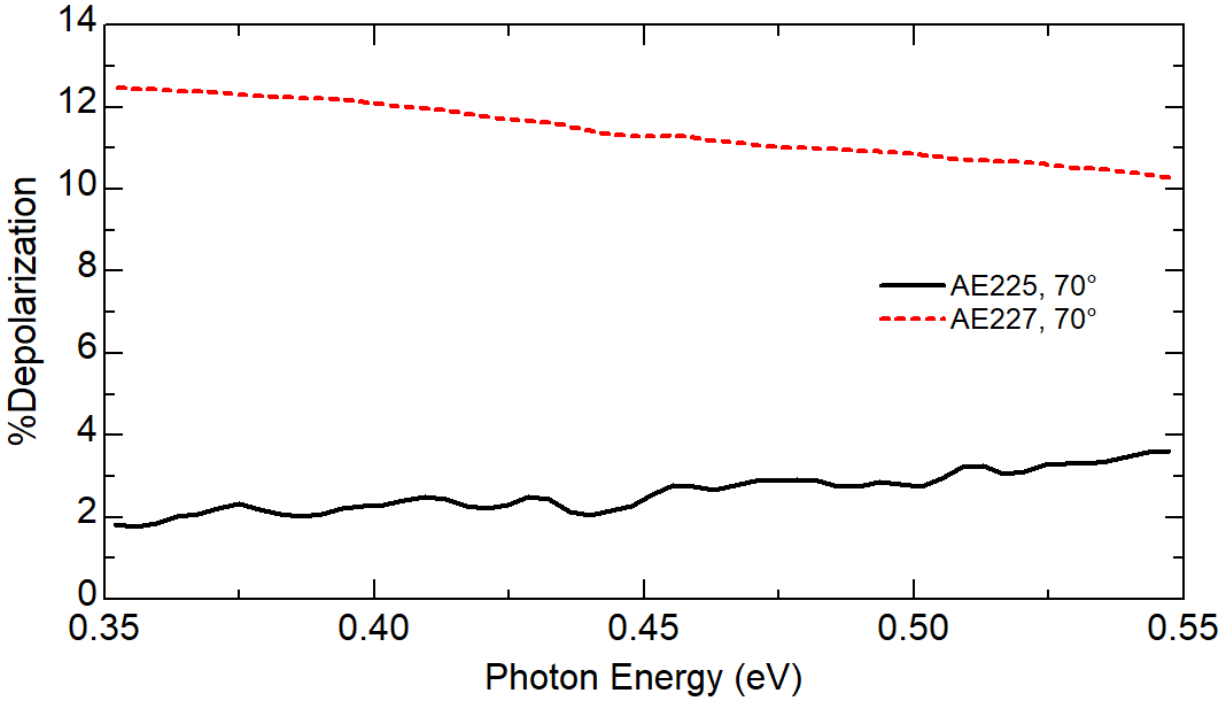

Figure 27: The depolarization spectra for samples AE225 and AE227.

5.3 Analysis: Basis Spline and Optical Sum Rules

Previously [19] collected temperature series data for 70 nm α-Sn films grown on InSb and CdTe substrates from 0.1 to 6.0 eV. The data was described using a parametric semiconductor (PSEMI) model with a fixed layer thickness to fit the critical points of the substrate across the whole spectrum. The model applied by [19] uses a PSEMI substrate layer that includes all critical points of the substrate material. On top of the substrate is the first layer that

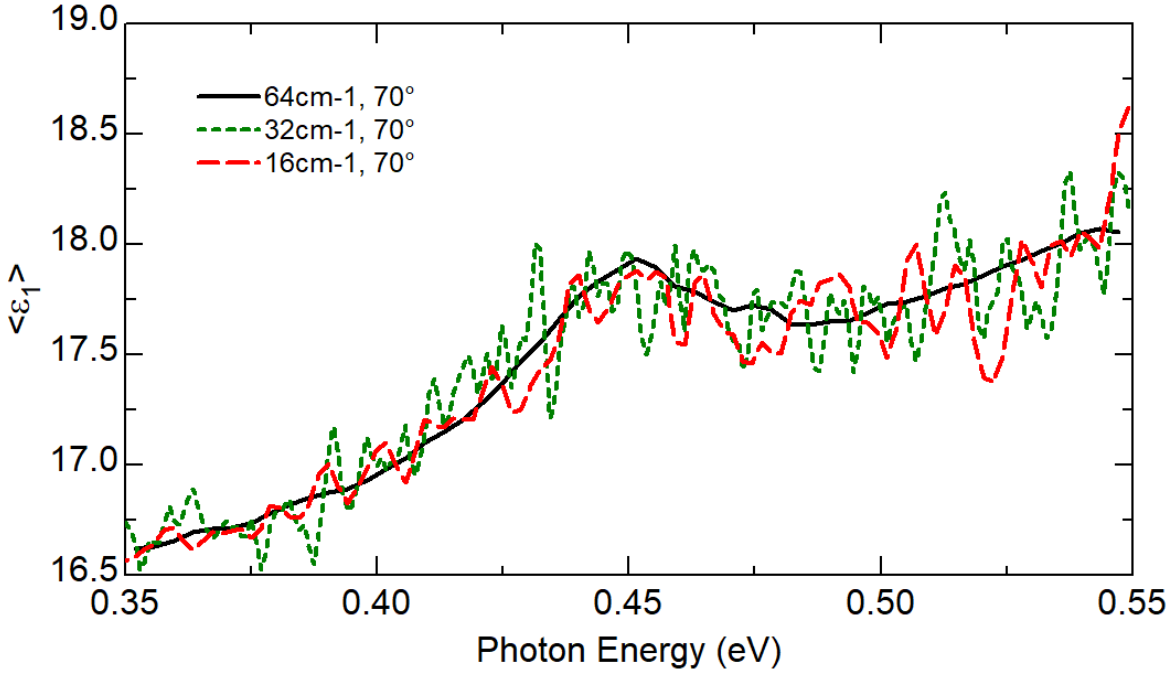

Figure 28: Scans were taken with different resolutions to optimize the signal to noise ratio.

intermixes a PSEMI model containing the tin critical points with a Drude term to describe the free carrier response at low energies. Additionally, the model includes an oxide layer where the oxide layer thickness is a fit parameter. The PSEMI model requires attention to details and tends to be time consuming and tedious especially when there are so many dependent parameters to fit. For grey tin films grown on InSb substrates the optical response is made complicated in part by the effect of free carriers causing a negative slope in ϵ_2 and square-root like increase in ϵ_1 below 0.25 eV. Additionally the $\bar{E}_0$ peak is relatively weak and the influence of critical points outside of the measured region leading to a large increasing slope towards the higher energies. The other complication is caused by interference effects from the substrate that show up as oscillations near the substrate band gap in the dielectric function of the layer.

In order to capture the features of the spectra such as the linear increase in absorption

Figure 29: Example showing the layer model used for our analysis (left) compared to layer model used in [19] (right).

towards higher energy's and the non-symmetric broadening of the absorption peak the layered PSEMI oscillator model becomes complicated. In order simplify the model we choose to parametrize layer 1 using a b-spline polynomial with a 20 meV to fit the grey tin layer optical constants. The two things that are required for using the b-spline are the layer thickness and the substrate optical constants. The layer thickness was confirmed to be 29.7 nm $\pm$ 0.7 nm using HRXRD. The substrate optical constants have been determined previously down to 77 K [35]. The fit describing the bulk InSb (100) optical constants is a PSEMI model that only fits the E_0 critical point shown by the first row marked with a hash in Figure 30. Each row in the window corresponds to material specific critical points. The critical point parameters represent the material optical constants and are known from theory and experiments. This figure is meant to illustrate the complexity of the PSEMI models previously used to describe the tin layers while also describing the source of the substrate optical constants. After achieving a good fit in the PSEMI model the InSb (100) optical constants are saved as a tabulated file and the process is repeated for each temperature.

Modeling with the b-spline is done using CompleteEase, an alternative software provided

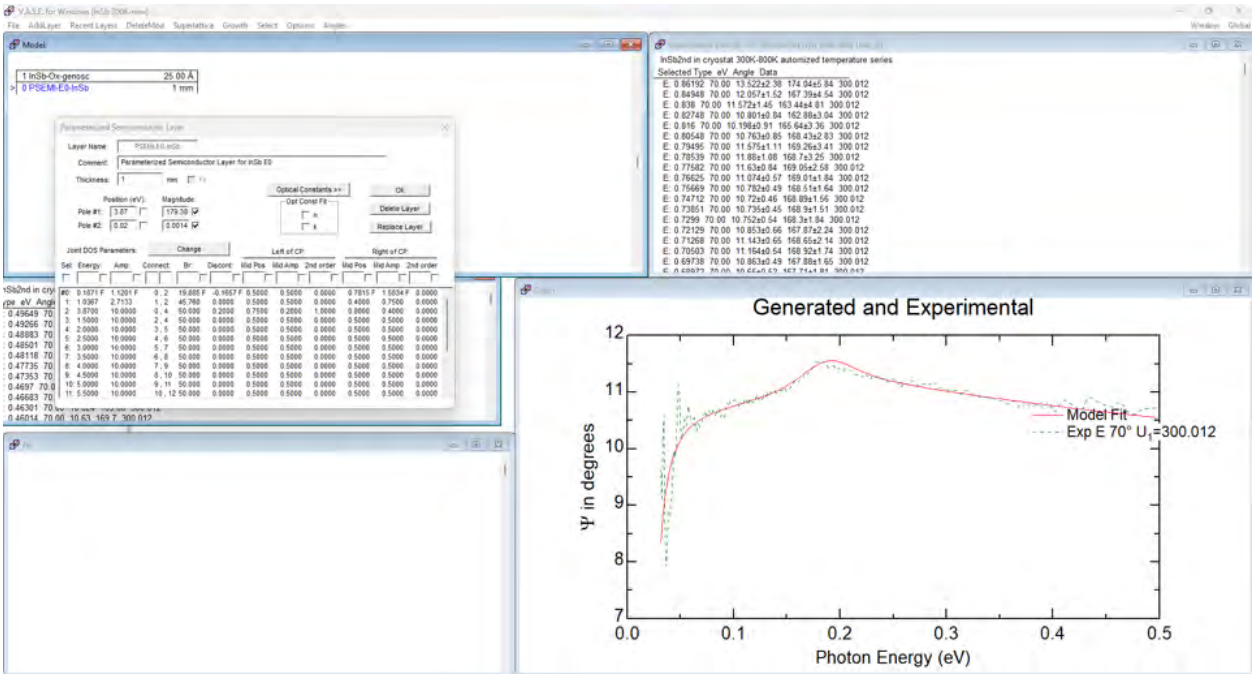

Figure 30: Example of the PSEMI model used to describe the InSb bulk substrate optical constants [35].

by the J. A. Woollam Company that has been adapted to better fit infrared SE data. The substrate optical constants are loaded as fixed values in the substrate layer and the b-spline layer was added on top with a fixed layer thickness of 30 nm. The basis spline model shown in Figure (29) is much simpler than in [19] but omits surface layers and intermixing of layers such as at the interface. The parameters that were allowed to vary were ϵ_∞ and the magnitude of an IR pole. Fixing the value of ϵ_∞ to 1 does not significantly change the quality of the fit. After the MSE has been minimized the complex dielectric function of the layer is extracted. This approach was repeated for each temperature step by exchanging the room temperature InSb optical constants with the InSb low temperature optical constants. For temperatures below 77 K we leave the 77 K InSb optical constants in place for the substrate. After using the basis spline function to extract the dielectric function the program FitYk is used to subtract a linear background from ϵ_2 in the region between 0.35 and 0.55 eV. After the linear

background subtraction we find the integrated peak intensity for the $\bar{E}_0$ absorption peak. The integrated peak intensity corresponds to the oscillator strength density and is related to the plasma frequency (23) through the relationship described by the Thomas-Reiche-Kuhn f-sum rule shown in equation (28) [2]. For this analysis the equation is modified to include the effective mass of the heavy hole band and has been converted into units of energy as shown in (29). It is through this relationship that we are able to calculate the carrier density using the integrated peak intensity of $\bar{E}_0$ in the imaginary part of the dielectric function.

The $\bar{E}_0$ IVB transition occurs from the Γ_7^- band to the Γ_8^+, heavy hole band and is observable in infrared spectroscopic ellipsometry measurements. The heavy hole band has a known effective mass that has been measured from oscillatory magneto-resistance measurements by [20, 45]. The effective mass was determined from the oscillation period seen in a reciprocal resistance versus magnetic field curve and was found to be $0.26m_0$ for the Γ_8^+ heavy hole band [45]. In this study of the effective mass was supported by a previous study of the Hall effect in grey tin which was done by [46] to determine the carrier concentrations for several grey tin samples prepared with different doping concentrations. They were able to overcome the challenges of measuring such a brittle material by using non-magnetic spring contacts set with a 1:4 indium to gallium solder and thin copper electrodes to prevent stress from differences in thermal expansion. The measurements were taken while the sample was submerged in a liquid bath of nitrogen, then propane, then butane. The results from [46] report that the Hall coefficient for p-type grey tin (In doped, p = 1.2 E 18 cm^{-3}) changes from positive to negative with increasing temperature indicating that the electron mobility is higher than the hole mobility. The result is opposite for n-type grey tin (As doped, 1.2 E 18 cm^{-3}) but they acknowledge that As is not as effective of a dopant as Sb.

Determining the carrier density as a function of temperature for intrinsic, p-type, and n-type grey tin samples is the focus of this analysis. The results from experimental data are compared with a theoretical calculation of the carrier density for intrinsic α-Sn. The theoretical carrier density calculation [38] is based on degenerate Fermi-Dirac carrier statistics and uses effective masses that have been determined by magneto-reflectance measurements [20]. The density of states for each band changes with the temperature. The Γ_7^- VB is always fully occupied and the 0 energy point is set at the Γ_8^+ degeneracy point. For intrinsic α-Sn at 0 K the Γ_8^+ band is fully occupied and the $\bar{E}_0$ transition is not allowed [38]. At higher temperatures there are unoccupied states especially for electron deficient p-type samples that increase the strength of the $\bar{E}_0$ transition from Γ_7^- to Γ_8^+ [38, 19]. The Fermi-Dirac distribution (30) gives the occupation factor and is a function of the band transition energy E, chemical potential μ, Boltzmann constant k_B, and temperature T.

An intrinsic semiconductor is electrically neutral and has an equal number of electrons and holes. Studies by [46, 45] describe the effect of doping in oscillatory magneto-resistance measurements where they found a strong correlation between doping and the Hall coefficient. From these measurements they were able to determine carrier mobility and carrier density but the experiments had to be carefully designed as not to damage the brittle grey tin samples. Here we have used ellipsometry as a non-destructive method to measure absorption from the $\bar{E}_0$ transition as a function of temperature for epitaxial grey tin layers prepared with different interface conditions and have confirmed that the $\bar{E}_0$ transition is sample dependent. The strength of the $\bar{E}_0$ absorption depends on the number of heavy holes in the Γ_8^+ band. If the α-Sn layer is grown on a surface that is In rich the In ions will diffuse into the epitaxial layer increasing the number of holes and causing p-type doping. If the α-Sn layer is grown

on an Sb rich interface then the diffusion would be by Sb increasing the number of electrons and causing n-type doping. Depending on the substrate material and substrate surface preparation the α-Sn layer can be intrinsic, p-type doped, or n-type doped. The carrier densities that we have calculated using the oscillator strength density are in agreement with the theoretical calculation based on Fermi-Dirac carrier statistics [38].

5.4 Results

Sample AE225 is a 30 nm α-Sn film grown on InSb (100) with a c(8x2) surface reconstruction and an In rich interface. Because of the interface preparation there is likely to be diffusion of In ions into the layer which will introduce more holes to the lattice leading to more $\bar{E}_0$ transitions especially at higher temperatures. Starting with the ellipsometric angle Ψ we see the InSb band gap as a peak at 0.17 eV as well as the $\bar{E}_0$ peak maximum at 0.45 eV. The peak intensity is largest at high temperatures and decreases towards low temperatures. In the pseudo dielectric function we see the same substrate and the layer critical points appearing at 0.17 eV and 0.45 eV, respectively. The $\bar{E}_0$ peak appears in $\langle\epsilon_1\rangle$ and when we extract the dielectric function the absorption peak appears in ϵ_2. In the dielectric function of the layer there are interference effects around 0.17 eV from the substrate E_0 critical point. This is expected because we are measuring thin films but it does not influence our analysis of the $\bar{E}_0$ peak since we are focusing on finding the integrated peak intensity. The real part of the dielectric function ϵ_1 increases towards the InSb critical point before becoming generally constant. The imaginary part of the dielectric function ϵ_2 has a negative slope below the InSb critical point and then increases towards higher energies.

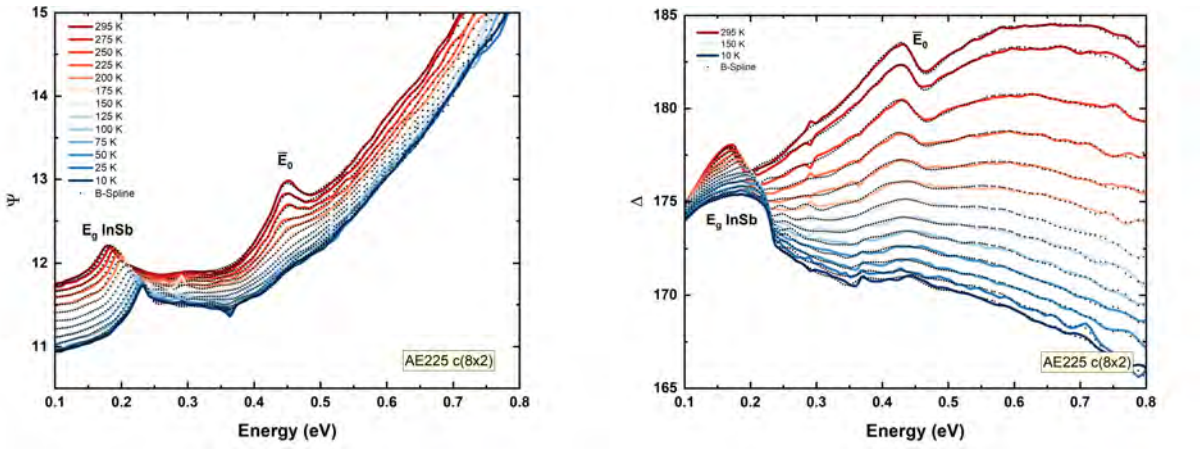

Figure 31: Ellipsometric angles Ψ and Δ from 295 K to 10 K for sample AE225.

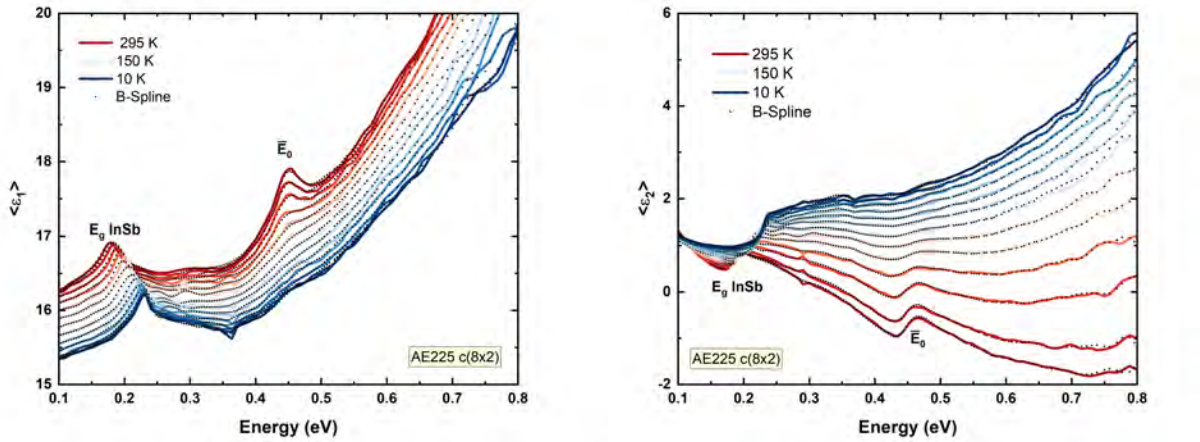

Figure 32: The pseudo dielectric function at temperatures from 300 K to 10 K for sample AE225.

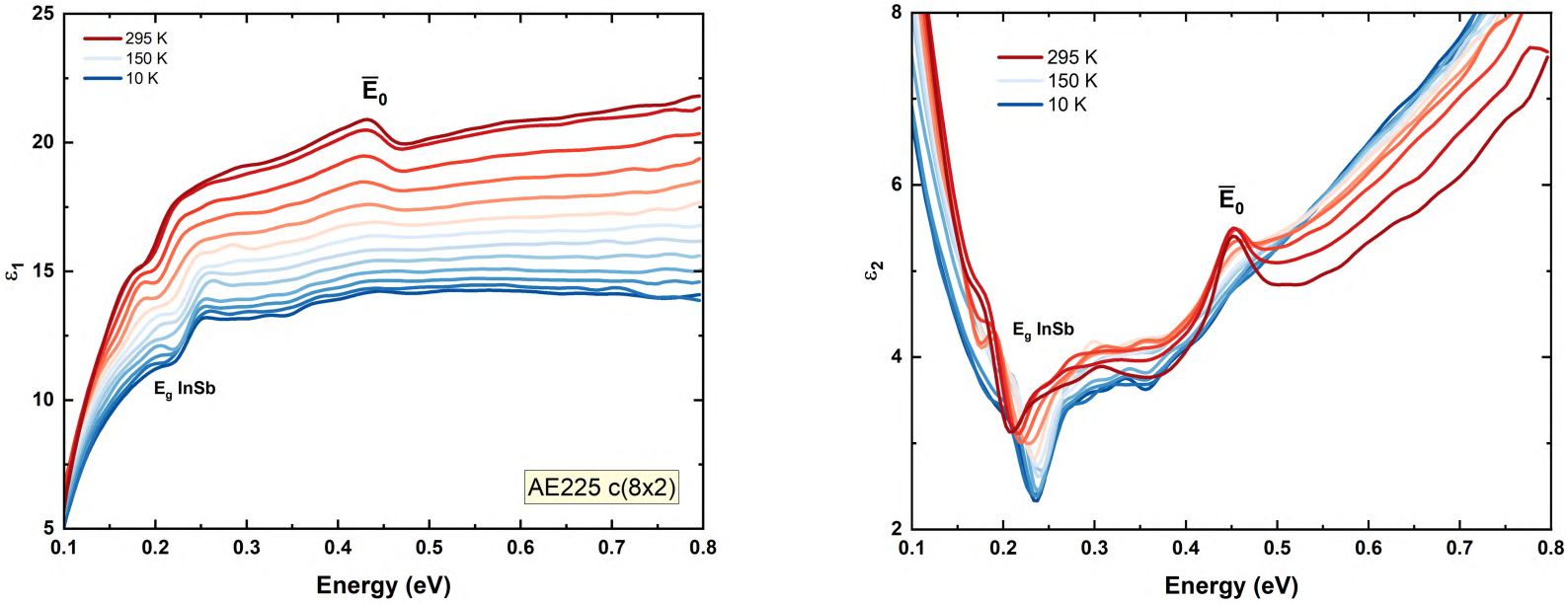

Figure 33: The complex dielectric function at temperatures from 295 K to 10 K for a 30 nm α-Sn layer grown on InSb (100) with an In rich interface, sample AE225.

Sample AE227 is a 30 nm α-Sn film grown on InSb (100) with a c(4x2) surface reconstruction and an Sb capped interface. The study by [46] found that Sb ions are more effective as donors than As ions and because the interface for AE227 was capped with Sb we expect that the epitaxial layer will will show the behavior of an n-type material due to the diffusion of Sb ions. The $\bar{E}_0$ peak intensity is much smaller than in AE225 since n-type doping increases the number of electrons and reduces the probability for transitions to occur into the heavy hole band. This is because n-type doping raises the occupation number of the heavy hole band therefore reducing the number of possible transitions at high and low temperatures [38]. The room temperature ellipsometric angle Ψ shown in Figure 34 shows the InSb band gap at 0.17 eV and the $\bar{E}_0$ maximum at 0.45 eV. The pseudo dielectric function in Figure 35 shows the InSb E_0 transition and α-Sn $\bar{E}_0$ transition. The dielectric function for AE227 is shown in Figure 36. The interference effects of the InSb critical point appear as oscillations near 0.17 eV in the dielectric function of the layer. The slope of ϵ_1 is negative approaching the InSb critical point and then flattens out towards higher energies. ϵ_2 shows the same behavior as in AE225.

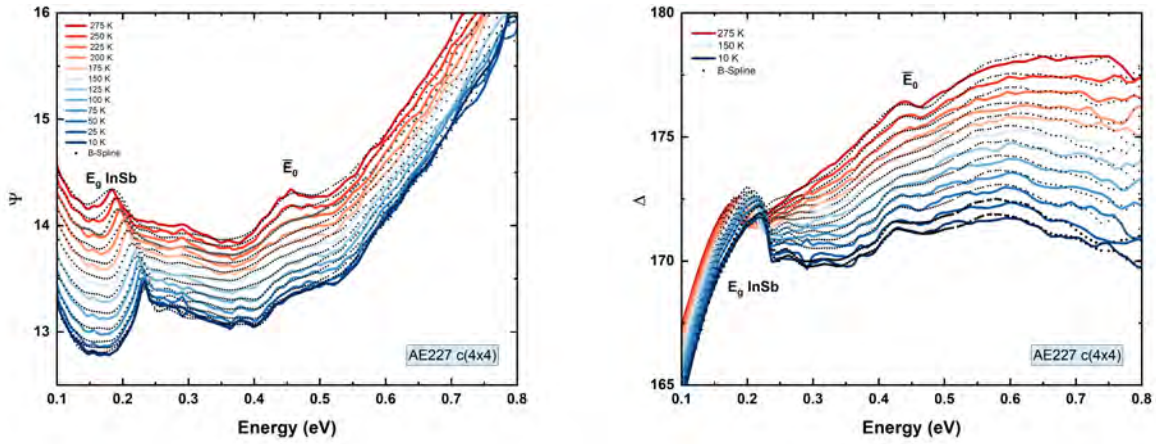

Figure 34: Ellipsometric angles Ψ and Δ for sample AE227.

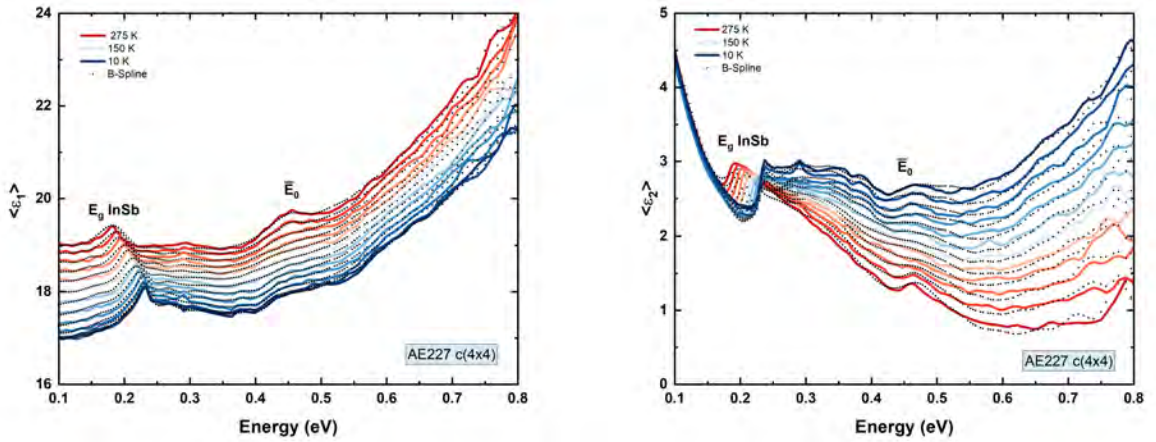

Figure 35: The pseudo dielectric function from 275 K to 10 K for sample AE227.

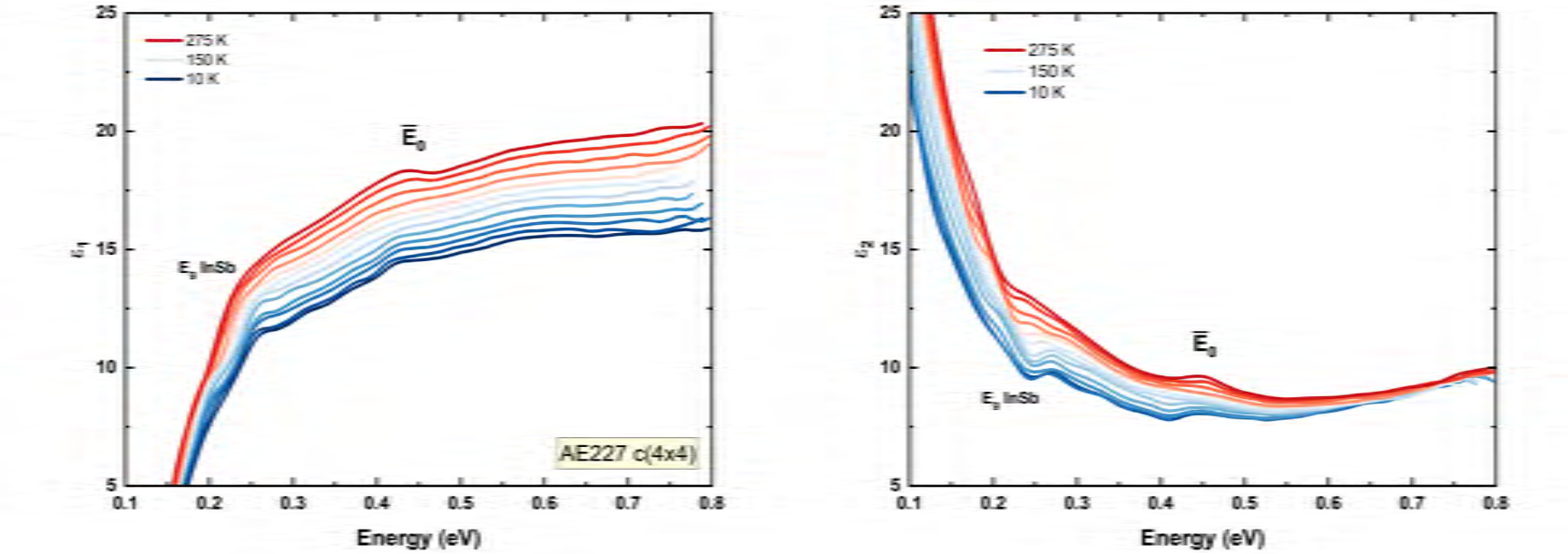

Figure 36: The infrared complex dielectric function at temperatures from 275 K to 10 K for a 30 nm α-Sn layer grown on InSb (100) with an Sb rich interface, sample AE227.

The samples we compare to AE225 and AE227 are 70 nm α-Sn films grown on InSb and CdTe substrates by a different group using MBE [19]. The $\bar{E}_0$ peak for RAC InSb has the largest peak intensity that does not decrease at low temperatures. The data for ϵ_2 shows a rising slope above the InSb critical point at high and low temperatures. The interference effects due to the substrate are not as prominent likely since layer thickness is twice as large. The CdTe substrate is considered intrinsic [19] and the $\bar{E}_0$ peak is significantly weaker than in the heavily hole doped α-Sn on InSb. The peak intensity decreases at low temperatures and the slope of ϵ_2 changes from negative to positive with decreasing temperature.

A linear background is subtracted from ϵ_2 and the area under the $\bar{E}_0$ peak was found by adding Gaussian functions together. Figures 37 and 38 shows the $\bar{E}_0$ peak for AE225 and AE227 with the linear background subtraction. The linear background subtraction and area calculation was repeated three times at each temperature to obtain an average integrated peak intensity since the peak limits are not well defined in the b-spline model by a parameter such as the broadening that is used in the standard oscillator models. The agreement in area between trials is within a fraction of a percent although it should be noted that this is likely the largest source of error in the calculation for the carrier density. The data obtained previously [19] was modeled using many PSEMI layers and to make this comparison I remodeled the data using the b-spline analysis procedure outlined in a previous section. The layer thickness was fixed at 70 nm and no surface layers or roughness was added. The carrier densities calculated from the f-sum rule for all samples are compared in Figure 40.

In Figure 39 we plot ϵ_2 at 300 K (solid) and 100 K (dots) with a linear background subtraction for samples AE225 (orange), AE227 (green), RAC InSb (purple), and RAC CdTe

(black). The intrinsic samples both show similar magnitudes at high and low temperatures. The heavily p-type doped sample has the largest oscillator strength and the oscillator strength increases at low temperatures. The n-type sample shows the smallest oscillator strength at high and low temperatures, for this sample the amplitude nearly the same. For the intrinsic sample shown in Figure 37 the $\bar{E}_0$ amplitude at room temperature is four times larger than at low temperatures and decreases gradually. Below 150 K the amplitude does not change significantly. The peak broadening decreases slightly with temperature. For the n-type sample shown in Figure 38 the $\bar{E}_0$ amplitude at room temperature is twice as large as at low temperatures. The peak broadening seems independent of temperature.

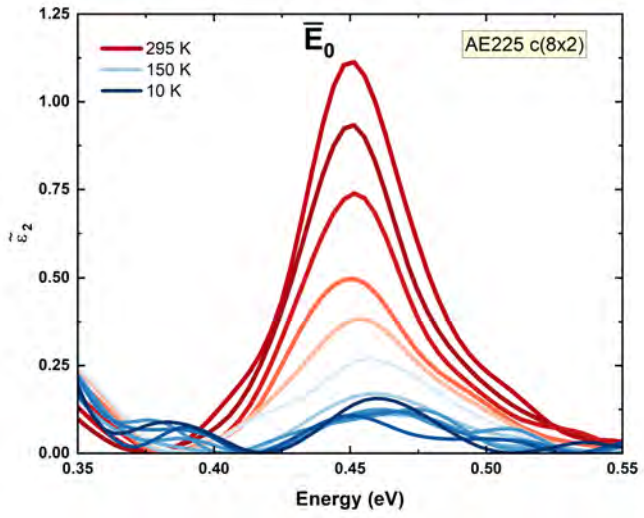

Figure 37: The $\bar{E}_0$ oscillator strength for sample AE225 shown at all temperature steps from 300 K to 10 K after the linear background subtraction.

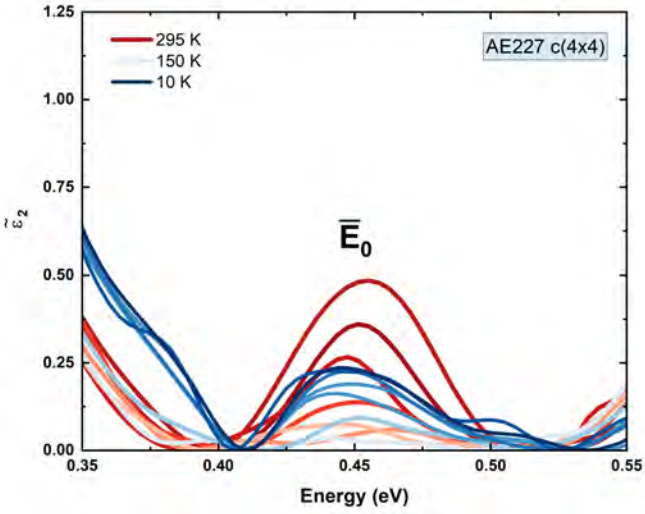

Figure 38: The $\bar{E}_0$ oscillator strength for sample AE227 shown at all temperatures from 300 K to 10 K after the linear background subtraction.

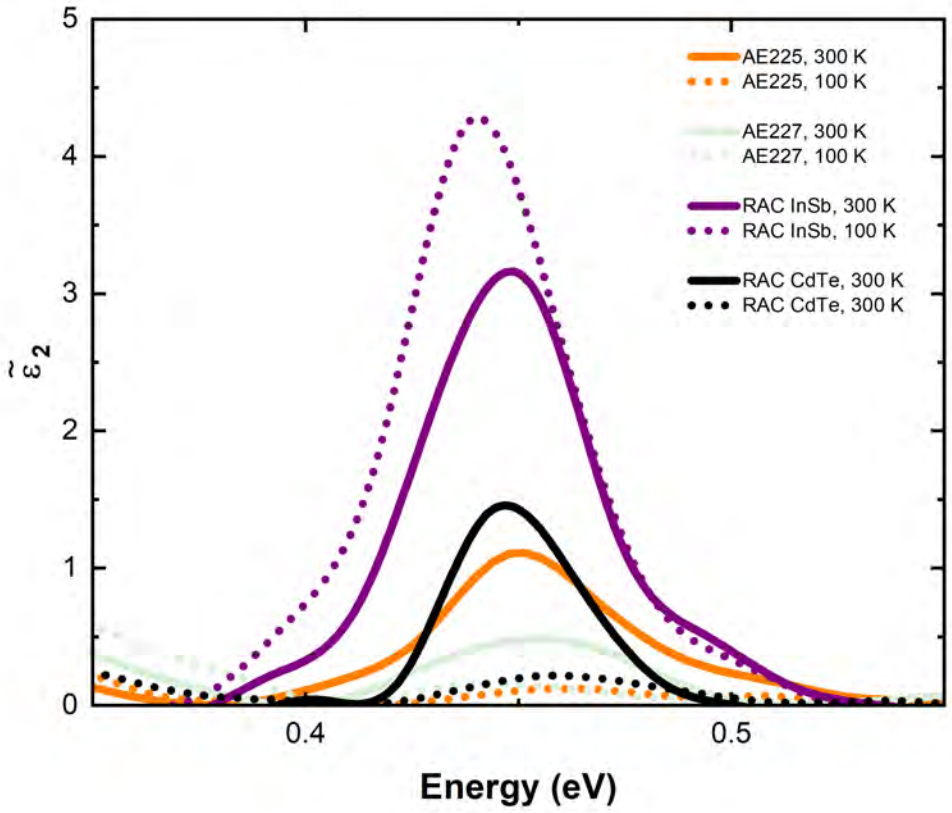

Figure 39: After the linear background subtraction we compare the oscillator strengths in $\tilde{\epsilon}_2$ at 300 K (solid) and 100 K (dots) for intrinsic, p-type, n-type doped α-Sn layers.

The hole density is proportional to the integrated peak intensity. The integrated peak intensity is smaller for samples with fewer carriers contributing to the $\bar{E}_0$ oscillator strength. In Figure 40 the red line shows the theoretical values for intrinsic α-Sn where n = p [38]. AE225 (purple) and RAC CdTE (grey) are the intrinsic reference samples and the experimental data agrees well with the theoretical values especially for sample AE225. Sample AE227 is n-type doped and shows the lowest values for hole density. RAC InSb is p-type doped because the hole density is significantly larger than the other samples at all temperatures.

Table 7: Carrier density at 300 K and 100 K for 30 nm and 70 nm grey tin layers grown on a variety of substrates. Experimental values are compared to literature values from [38].

Sample	Type	$\bar{E}_0$ (eV)	$\bar{E}_0$ (eV)	p $\cdot 10^{18}$ (cm^{-3})	p $\cdot 10^{18}$ cm^{-3})
		300 K	100 K	300 K	100 K
SZ	intrinsic	-	-	3.67	0.61
AE225	intrinsic	0.452	0.459	3.558	0.376
AE227	n-type	0.455	0.447	1.504	0.746
RAC InSb	p-type	0.448	0.440	9.637	11.00
RAC CdTe	intrinsic	0.447	0.458	3.031	0.636

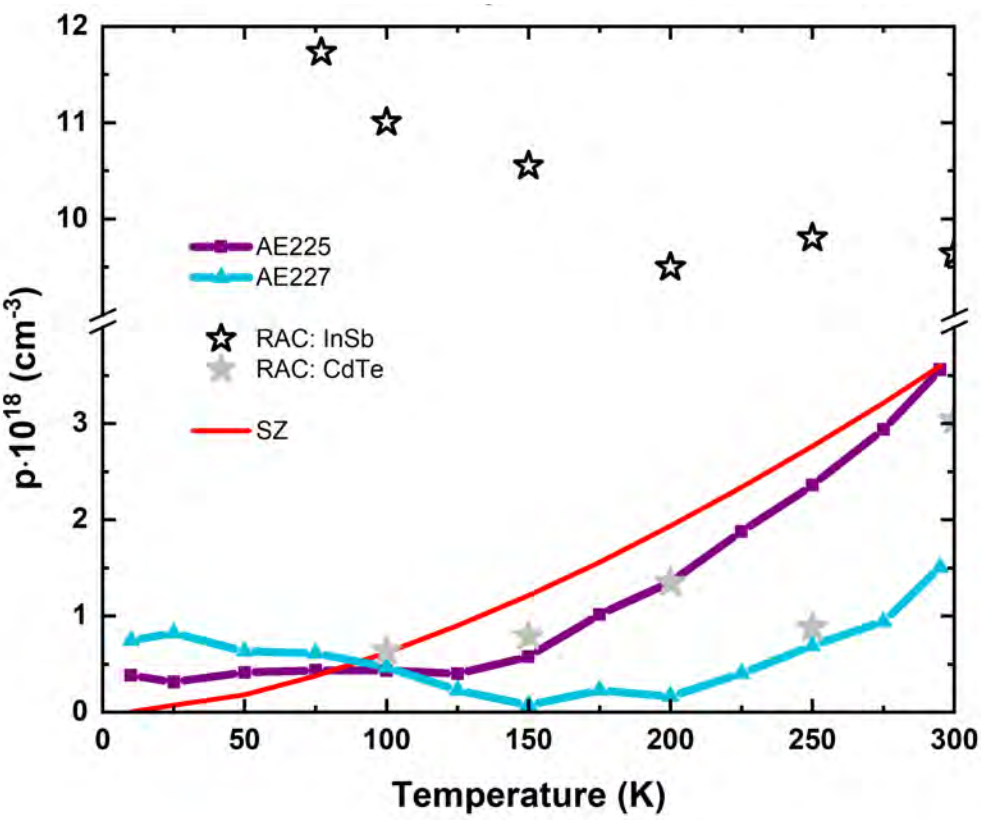

Figure 40: The hole density as a function of temperature for 30 nm and 70 nm α-Sn layers grown on different substrates.

6 CONCLUSIONS

6.1 Calcium Fluoride

Calcium fluoride substrates with different surface orientations, (100) and (111), were measured from 0.14 to 40 μm using two ellipsometers and the experimental data was modeled using the methods described in a previous chapter. The structural characterization of the (100) and (111) substrates was done using XRD and confirms the surface orientation of each bulk crystal by comparison with a CaF_2 powder spectrum. The lattice constants for CaF_2 (100) and (111) were calculated by applying (5) and was found to be 5.4639(8) Å and 5.4778(2) Å, respectively.

The infrared data shows a band of high reflectivity called the restrahlen band which was used to determine the mode frequencies of the infrared active TO and LO phonons. We find that for CaF_2 (100) $\lambda_{LO} = 20.82$ μm and $\lambda_{TO} = 38.48$ μm. For CaF_2 (111) $\lambda_{LO} = 20.95$ μm and $\lambda_{TO} = 38.23$ μm. Calcium fluoride crystallizes in an isotropic structure meaning that the results for the (100) and (111) substrates should be equal. The results show that the values for the TO and LO phonon modes are the same within the experimental uncertainty of 1%. In addition to finding the phonon mode frequencies we also identify a region of two phonon absorption that is visible as a dip in the restrahlen band near 33 μm. Additionally we find the high frequency dielectric constant, ϵ_∞, to be 1.991 and 1.971 for the (100) and (111) substrates, respectively. The values determined experimentally by this study are smaller than the value of 2.045 used in calculations to determine the refractive index and extinction coefficients compiled in table IV of The Handbook of Optical Constants of Solids II [8, 1,

9]. We find the static dielectric constant, ϵ_s, to be 6.409 and 6.134 for the (100) and (111) substrates, respectively.

The optical constants in the visible and vacuum ultra-violet for the (100) and (111) substrates both show normal dispersion and no absorption as expected in the transparent region of the material. There is a small negative pseudo-absorption observed in the imaginary part of the pseudo dielectric function for both substrates. The negative pseudo-absorption is non-physical and we attribute the feature to the presence of a surface layer with a larger refractive index than the bulk substrate. A surface layer was added to the model and the thickness was found to be 21 Å and 64 Å for the (100) and (111) substrates, respectively. The refractive index for the layer and substrate are compared in Figures 16 and 17 and it is clear that the refractive index of the layer is larger than the substrate at almost all wavelengths. In order to better charachterize the small absorption feature analysis of VUV transmission measurments would be required, but this data is not avaliable as of now.

Additionally, we point to previous studies [4, 29, 41] describing the influence of oxygen ions filling in fluorine vacancies on the absorption band onset. The studies conclude that increasing the impurities lowers the onset energy of the absorption band [29]. Specifically, if the impurity is oxygen then the absorption band onset is reduced to a value closer to 7 eV rather than the expected 11 eV as found by [10]. Based on the comparison made with the tabulated optical constants by [1] it is clear that the onset of absorption for the MTI Co. calcium fluoride substrates is lower than the literature values. When the literature values for the TO phonon mode are compared with our experimental results we see that the TO mode is shifted about 0.5 meV above the literature values. The literature values from [1, 8] are calculated at room temperature. The experimental data was also collected at room

temperature and we can eliminate thermal effects that may shift the phonon mode. Based on the observations mentioned above and the fact that the TO phonon mode is shifted for both samples it is reasonable to attribute these slight deviations to the presence of defects in the lattice. This is further supported by the fact that the deviations are larger for CaF_2 (111) which happens to have a thicker overlayer than CaF_2 (100).

6.2 Grey tin

XRD was used to measure the diffraction patterns for sample AE225, a 30 nm α-Sn layer grown via MBE on an InSb (100) substrate, β-Sn powder 99.95%, and bulk InSb (100). This data was used to determine the quality of the α-Sn layer by identifying peaks that would correspond to the β-Sn powder. It appears that the α-Sn phase was preserved by strain from the substrate and there are no significant peaks indicating an overall phase transformation of the layer that may have been caused by thermal stress during the temperatrure series. There are however small peaks with intensities less than 100 counts that do align with the (112) and (301) orientations of the β-Sn powder suggesting that there may be small regions where a phase transition has occurred or that the surface was contaminated by β-Sn grains during measurements. The peaks due to the substrate and layer were identified by comparing spectra for AE225 and bulk InSb (100) and using the structure factors to attribute the (200) and (600) peaks to the InSb substrate only. The spectra were used to calculate the Bragg plane spacing and lattice constants for selected peaks for each material and a comparison is made in table 5 with expected values from VESTA [15]. The peaks selected for the β-Sn powder correspond to the suspected β-Sn peaks observed in AE225. High resolution XRD was used to measure a symmetric (004) ω-2θ scan of the AE225 sample in order to determine the in

plane and out of plane lattice mismatch. The epitaxial layer is pseudomorphic on the InSb (100) substrate and therefore the parallel lattice mismatch, $\delta_{L||}$ is 0%. The perpendicular lattice mismatch $\delta_{L\perp}$ is 0.19%.

Temperature dependent spectroscopic ellipsometry was used to collect data from 300 K to 10 K for samples AE225 and AE227. The experimental data was modeled using fixed substrate optical constants and the layer was parametrized using a basis spline function with a small node spacing. The dielectric function of the layer was extracted at each temperature to observe the change in the $\bar{E}_0$ absorption peak for both samples. Qualitatively the oscillator strength at room temperature is larger for the α-Sn that was prepared on the In rich interface. The oscillator strength decreases with decreasing temperature for both samples. To quantitatively analyze the oscillator strength we apply a linear background subtraction to ϵ_2 and then find the integrated peak intensity for the $\bar{E}_0$ peak as a function of temperature. We apply the Thomas-Reiche-Kuhn [2] f-sum rule (28) to determine the carrier density as a function of temperature.

We applied the same analysis procedure to temperature series data collected by [19] for 70 nm α-Sn layers on InSb and CdTe substrates. The results for the hole density as a function of temperature are compiled in Figure 40. The experimental values are plotted alongside the theoretical calculation of the carrier density that is based on degenerate Fermi-Dirac Carrier statistics for an intrinsic α-Sn sample [38]. Deviations from the theoretical model are attributed to the amount and type of doping present in each of these four samples. Intrinsic samples AE225 and RAC CdTe show the closest agreement with the theoretical values. Sample AE227 is n-type doped due to diffusion by Sb ions into the epitaxial layer and shows the lowest hole density which is nearly constant with temperature. Sample RAC

InSb has the largest carrier density and is heavily p-type doped. Interface preparation with only an atomic hydrogen clean leads to α-Sn layers with p-type doping due to diffusion by In. Interface preparation using Sb to cap the substrate leads to reduced hole densities due to n-type doping of the α-Sn layer. We confirm that the optical response and electronic properties of pure α-Sn can be tuned by changing the interface preparation or the substrate material. We have demonstrated a non-destructive method for determining the carrier density that gives good agreement with theory.

References

[1] D. F. Bezuidenhout. *Handbook of Optical Constants of Solids II*. Academic Press, San Diego, 1997, p. 815.

[2] M. Altarelli et al. "Superconvergence and Sum Rules for the Optical Constants". In: *Phys. Rev. B* **6** (1972), p. 4502.

[3] G. S. Rohrer. *Structure and Bonding in Crystaline Materials*. Cambridge University Press, 2001.

[4] N. I. Medvedeva et al. *Effects of Defects in the Vacuum-Ultraviolet Parameters of CaF_2*. Plenum Publishing Corporation, 1985, p. 649.

[5] Fairfield Crystal Technology. *Material Properties and Specifications: Calcium Fluoride (CaF_2)*.

[6] H. Landolt and R. Bornstein. *Zahlenwerte und Funktionen aus Physik, Chemie, Astronomie, Geophysik und Technik*. Vol. **6**. Springer-Verlag, Berlin Heidelberg, (1982), p. 911.

[7] R. Tousey. "Optical Constants of Fluorite in the Extreme Ultraviolet". In: *Phys. Rev.* **50** (1936), p. 1057.

[8] I. H. Malitson. "A Redetermination of Some Optical Properties of Calcium Fluoride". In: *Appl. Opt.* **2** (1963), p. 1103.

[9] W. Kaiser et al. "Infrared Properties of CaF_2, SrF_2, and BaF_2". In: *Phys. Rev.* **127** (1962), p. 6.

[10] T. Tomiki and T. Miyata. "Optical Studies of Alkali Fluorides and Alkaline Earth Fluorides in VUV Region". In: *J. Phys. Soc. Jpn.* **27** (1969), p. 658.

[11] H. Landolt and R. Bornstein. *Semiconductors: Physics of Group IV Elements and III-V Compounds*. Vol. **17**. Springer-Verlag, Berlin Heidelberg, 1982.

[12] H. Song et al. "Thermal Stability Enhancement in Epitaxial Alpha Tin Films by Strain Engineering". In: *Adv. Eng. Mater.* **21** (2019), p. 1900410.

[13] F. Legrain and S. Manzhos. "Understanding the difference in cohesive energies between alpha and beta tin in DFT calculations". In: *AIP Adv.* **6** (2016), p. 045116.

[14] R. F. C. Farrow et al. "The Growth of Metastable, Heteroepitaxial Films of α-Sn by Metal Beam Epitaxy". In: *J. Cryst. Growth* **54** (1981), p. 507.

[15] K. Momma and F. Izumi. "VESTA 3 for three-dimensional visualization of crystal, volumetric and morphology data". In: *J. Appl. Crystallogr.* **44** (2011), p. 1272.

[16] M. R. Bauer et al. "Tunable band structure in diamond–cubic tin–germanium alloys grown on silicon substrates". In: *Solid State Commun.* **127** (2003), p. 355.

[17] T. D. Eales et al. "$Ge_{1-x}Sn_x$ alloys: Consequences of Band Mixing Effects for the Evolution of the Band gap Γ-character with Sn Concentration". In: *Sci. Rep.* **9** (2019), p. 14077.

[18] R. A. Carrasco et al. "Dielectric Funciton and Band Structure of $Sn_{1-x}Ge_x$ (x⟨ 0.06) Alloys on InSb". In: *Appl. Phys. Lett.* **114** (2018), p. 06102.

[19] R. A. Carrasco et al. "The Direct Bandgap of Gray α-tin Investigated by Infrared Ellipsometry". In: *Appl. Phys. Lett.* **113** (2018), p. 232104.

[20] S. H. Groves et al. "Interband Magnetoreflection of α-Sn". In: *J. Phys. Chem. Solids* **31** (1970), p. 2031.

[21] U. Pietsch, V. Holy, and T. Baumbach. *High-Resolution X-Ray Scattering: From Thin Films to Lateral Nanostructures Second Edition*. Springer-Verlag, New York, 2004.

[22] B. D. Cullity and S. R. Stock. *Elements of X-Ray Diffraction 3rd Edition*. Pearson, New Jersey, 2001.

[23] P. F. Fewster. "X-ray analysis of thin films and multilayers". In: *Rep. Prog. Phys* **59** (1996), p. 1339.

[24] PANalytical B.V. *Epitaxy and SmoothFit Quick Start Guide*. PANalytical, The Netherlands, 2012.

[25] D. J. Griffiths. *Introduction to Electrodynamics, Fourth Edition*. Cambridge Univeristy Press, Cambridge, 2017.

[26] H. G. Tompkins and J. N. Hilfiker. *Spectroscopic Ellipsometry Practical Applications to Thin Film Charachterization*. Momentum Press, New York, 2016.

[27] J.A. Woollam Co. Inc. *Guide to Using WVASE32 Spectroscopic and Ellipsometry Data Analysis Software*. J.A. Woollam Co., Inc., 2017.

[28] H. Fujiwara. *Spectroscopic Ellipsometry Principles and Applications*. Maruzen Co. Ltd., Tokyo, 2009.

[29] M. M. Elcombe and A. W. Pryor. "The lattice dynamics of calcium fluoride". In: *J. Phys. C: Solid State Phys.* **3** (1970), p. 492.

[30] M. Schubert. *Infrared Ellipsometry on Semiconductor Layer Structures Phonons, Plasmons, and Polaritons*. Springer-Verlag, Berlin Heidelberg, 2004.

[31] A. F. Turner, L. Chang, and T. P. Martin. "Enhanced Reflectance of Reststrahlen Reflection Filters". In: *Appl. Opt.* **4** (1965), p. 927.

[32] N. S. Samarasingha and S. Zollner. "Temperature dependence of the optical phonon reflection band in GaP". In: *J. Vac. Sci. Technol. B* **39** (2021), p. 052201.

[33] B. Johs and J. S. Hale. "Dielectric function representation by B-splines". In: *p hys. stat. sol. (a).* **205** (2008), p. 715.

[34] J. Mohrmann et al. "Application of a B-spline Model Dielectric Function to Infrared Spectroscopic Ellipsometry Data Analysis". In: *J. Vac. Sci. Technol. B* **38** (2020), p. 014001.

[35] M. R. Arias et al. "Temperature Dependence of the Infrared Dielectric Function and the Direct Bandgap of InSb from 80 to 725 K". In: *J. Vac. Sci. Technol. B* **41** (2023), p. 022203.

[36] J. J. Hopfield. "Sum Rule Relating Optical Properties to the Charge Distribution". In: *Phys. Rev. B* **2** (1970), p. 973.

[37] F. Bassani. "Optical Sum Rules and Kramers–Kronig Relations". In: *J. Vac. Sci. Technol. B.* **38** (2020), p. 200.

[38] S. Zollner. "Excitonic Effects in the Optical Absorption of Gapless Semiconductor α-tin Near the Direct Bandgap." In: *J. Vac. Sci. Technol. B* **42** (2024), p. 022203.

[39] Scientific Instruments. *Si-540 Silicon Diode Cryogen Temperature Sensor.*

[40] HORIBA Jobin Yvon. *What is the Mueller matrix and why is it useful?*

[41] P. Feltham and I. Andrews. "Colour Centers in Alkaline Earth Fluorides". In: *Phys. Stat. Sol.* **10** (1965), p. 203.

[42] A. N. Engel et al. "Growth and Characterization of α-Sn Thin Films on In- and Sb-rich Reconstructions of InSb(001)". In: *Phys. Rev. Mater.* **8** (2024), p. 044202.

[43] F. Stern. *Solid-State Physics.* Vol. **15**. Academic, New York, 1963, p. 300.

[44] D. Y. Smith. *Handbook of Optical Constants of Solids.* Academic Press, San Diego, 1998, p. 35.

[45] E. D. Hinkley and A. W. Ewald. "Oscillatory Magnetoresistance in Gray Tin". In: *Phys. Rev.* **134** (1964), A1261.

[46] E. E. Kohnke and A. W. Ewald. "Hall Effect in Gray Tin Filaments". In: *Phys. Rev.* **102** (1956), p. 1481.